eXPRESS Polymer Letters Vol.1, No.10 (2007) 640
Available online at www.expresspolymlett.com
DOI: 10.3144/expresspolymlett.2007.87

Editorial corner – a personal view

Nanoindentation: an emerging technique for polymer surface mechanical characterization

P. M. Frontini[*]

Instituto de Ciencia y Tecnología de Materiales (INTEMA), CONICET Universidad Nacional de Mar del Plata, Juan B. Justo 4302, B7608FDQ Mar del Plata, Argentina

Polymer surfaces are the phase boundaries that reside between the bulk polymer and the outer environments. For many applications they have to be modified using physical or chemical processes to achieve the desired functional properties. Examples are biomedical, automobile, microelectronic or packaging applications. While the driving force of surface modification is generally the functional properties, good surface and global mechanical properties are necessary in most applications. Surface analytical methodologies have already been well established, but mechanical characterization of polymeric surfaces is still a subject of debate.

The so-called depth sensing indentation or nanoindentation is a well established instrumental technique to assess Young's Modulus and hardness, of hard inorganic engineering materials, but its usage is rather questionable for thin and low compliant materials like soft polymers and polymeric films. The analysis of nanoindentation data is often based on the Oliver and Pharr approach which displays limitations in describing viscoelastic and viscoplastic behavior of polymers, and uneven yielding behavior under multiaxial stress systems. Experiments also depends on a number of parameters like the shape of the indenter tip, the strain history of the sample or adhesion phenomena between tip and surface, surface preparation and pre-conditioning of the sample. Besides, properties of polymeric materials also depend on many intrinsic factors which range from monomeric level to macroscopic level, such as monomer sequence, tacticity, short-chain branching, long-chain branching, molecular weight, molecular weight distribution, degree of chain orientation, degree of crystallization, and the states of the crystal-amorphous interfaces which may promote, for instance, strain hardening. Despite the mentioned limitations, comparative studies of polymers have been recently reported which encourage the use of this technique to assess surface modified polymers.

Further research on the nanoscale mechanical response of polymers should be focused on the development of new analysis procedures assisted by mathematical modeling and numerical simulation capable of determining absolute quantitative constitutive equations representative of the actual mechanical behavior of polymers. When this goal has been met, nanoindentation will become a powerful tool to optimize the surface polymer tailoring.

Prof. Dr. Patricia Maria Frontini
Member of International Advisory Board

---

[*]Corresponding author, e-mail: pmfronti@fi.mdp.edu.ar

eXPRESS Polymer Letters Vol.1, No.10 (2007) 641–653
Available online at www.expresspolymlett.com
DOI: 10.3144/expresspolymlett.2007.88

Dynamic mechanical analysis of binary and ternary polymer blends based on nylon copolymer/EPDM rubber and EPM grafted maleic anhydride compatibilizer

C. Komalan[1], K. E. George[2], P. A. S. Kumar[3], K. T. Varughese[4], S. Thomas[5]*

[1]S.N.M College, Maliankara, Kerala-683516, India
[2]Department of PS&RT, Cochin University of Science and Technology, Cochin-22, Kerala, India
[3]NIT Calicut P.O, Calicut, Kerala, India
[4]Central Power Research Institute, Bangalore-560080, Karnataka, India
[5]School of Chemical Science, M.G University, Kottayam-686560, Kerala, India

Received 30 March 2007; accepted in revised form 17 June 2007

Abstract. The dynamic mechanical properties such as storage modulus, loss modulus and damping properties of blends of nylon copolymer (PA6,66) with ethylene propylene diene (EPDM) rubber was investigated with special reference to the effect of blend ratio and compatibilisation over a temperature range –100°C to 150°C at different frequencies. The effect of change in the composition of the polymer blends on tanδ was studied to understand the extent of polymer miscibility and damping characteristics. The loss tangent curve of the blends exhibited two transition peaks, corresponding to the glass transition temperature (T_g) of individual components indicating incompatibility of the blend systems. The morphology of the blends has been examined by using scanning electron microscopy. The Arrhenius relationship was used to calculate the activation energy for the glass transition of the blends. Finally, attempts have been made to compare the experimental data with theoretical models.

***Keywords:** polymer blends and alloys, dynamic mechanical analysis, compatibilisation*

1. Introduction

Thermoplastic elastomers (TPEs) are being used in a variety of applications because of their desirable mechanical properties and recyclability [1, 2]. Dynamic mechanical thermal analysis (DMTA) has proved to be an effective tool in the characterisation studies of viscoelastic materials.

Several researchers [3–9] have investigated effects of blend ratio and compatibilisation on the dynamic mechanical properties. Al-Malaika and Kong [10] studied the compatibilisation of functionalised EPR with GMA. Examination of the DMA of the reactive and physically compatibilized blends shows a smaller separation between the glass transition temperatures. Rajan *et al.* [11] have studied the dynamic mechanical properties of PP in the thermoplastic elastomeric state. α-relaxation peaks of PEEK and PES and their blends were studied by Nandan *et al.* [12]. Kumar *et al.* [13] have studied the dynamic mechanical properties of EPDM-g-VOS/LLDPE blends with special reference to the effect of blend ratio. They found that increasing the proportion of LLDPE decreases the T_g value of blend and there were increase in E' and E'' due to increase in crystallinity. Karger-Kocsis and Kiss [14] have investigated morphology and dynamic mechanical properties of EPDM/PP blends and PP block polymers. In these blends as the concentra-

---

*Corresponding author, e-mail: sabut@sancharnet.in

tion of EPDM increases, E' of the blends decreases. The dynamic mechanical spectrum showed two separate damping peaks and therefore has a two-phase morphology indicating that the blend is incompatible. Guo *et al.* [15] studied the dynamic mechanical properties of PA6/PS blend systems. Gopakumar *et al.* [16] found that the compatibilisation does not affect the transition temperature of the respective components while several other researchers [17, 18] have reported that the incorporation of the compatibilizer leads to obvious shifting of T_g's. These authors are of the opinion that the effect of compatibilizers on the position of T_g is a reflection of the extent of compatibilisation. Moly *et al.* [19] have studied the effect of compatibilisation on the dynamic mechanical properties of LLDPE/EVA blends and found that compatibilisation increased the storage modulus of the system which is due to the fine dispersion of EVA domains in the LLDPE matrix providing an increased interfacial interaction.

In this communication, effects of blend ratio and compatibilisation on the dynamic mechanical properties of nylon copolymer/EPDM blends were investigated. Viscoelastic properties like storage modulus, loss modulus and tanδ were investigated as a function of temperature.The dynamic mechanical properties of the new generation of nylon copolymer/EPDM blends are extremely important, as these data are still limited in the literature. The dynamic mechanical properties have been correlated with the morphology of the blends. Attempts have also been made to correlate the experimental viscoelastic data with various theoretical models.

2. Experimental

2.1. Materials

The raw materials used for this work are as follows. Nylon copolymer (PA6,66) (Tufnyl120) of melting point 148°C and density of 1.12 g/mol, with $\overline{M}_n$ 38 000 was supplied by SRF Ltd (Madras, India). EPDM (KELTAN 720) with E/P ratio 58/35.5 wt% and DCPD content 6.5 wt% with $\overline{M}_n$ 120 000 was obtained from DSM (Netherlands).

The EPM-g-MA with 1 wt% of MA grafting with E/P ratio 55/45 having density 0.88 g/mol (Royaltuf 465) was supplied by Uniroyal Chemical Company, Germany.

2.2. Blend preparation

Nylon copolymer (PA6,66) pellets were dried in vacuum oven at 80°C for 24 h before blending .The blends were prepared in a Brabender at a temperature of 180°C and a rotor speed of 60 rpm. Nylon was first melted for 2 minutes and then EPDM was added and the mixing was continued for 6 more minutes. In the case of compatibilized blends, the compatibilizer EPM-g-MA was mixed with EPDM in a two roll mill at room temperature so as to get EPM-g-MA coated EPDM. Nylon is fed into the preheated Brabender at 180°C and melted for 2 minutes. Then EPM-g-MA coated EPDM is added and melting is continued for 6 more minutes (Total mixing time fixed was 8 minutes). Test samples were prepared by compression molding in a hydraulic press at 180°C. The volumetric proportion of 70/30 nylon/EPDM blends were prepared with compatibilizer concentrations of 0, 1, 2.5, 5, 10 wt% based on the minor phase. Test specimens are compression moulded into 2 mm thick sheets at 180°C for 3 minutes in an electrically heated hydraulic press at a pressure of 10 MPa.

2.3. Designation of the blends

The blends were designated as follows. N_0 means EPDM and N_{100} means nylon copolymer. N_{70} means a blend of 70 parts of nylon and 30 parts of EPDM. The binary blends were designated as N_0, N_{30}, N_{50}, N_{70} and N_{100} where the subscripts denote the weight percentage of nylon in the blend. The EPM-g-MA compatibilized N_{70} blends were designated as N_{70x}, where x denotes the weight percentage of compatibilizer in the blend. Various blends studied with their compositions are summarized in Table 1.

Table 1. Compositions and codes of the samples used

System	PA6,66		EPDM		EPM-g-MA	
	[wt%]	[vol%]	[wt%]	[vol%]	[wt%]	[vol%]
N_0	–	–	100	100	–	–
N_{30}	30	27.6	70	72.4	–	–
N_{50}	50	50	50	50	–	–
N_{70}	70	71.4	30	30.6	–	–
N_{100}	100	100	–	–	–	–
N_{701}	70	71.4	29	29.6	1	0.3
$N_{702.5}$	70	71.4	27.5	28.1	2.5	0.7
N_{705}	70	71.4	25	25.5	5	1.3
N_{7010}	70	71.4	20	20.4	10	2.0

N – nylon copolymer, N_0 – ethylene propylene diene rubber

2.4. Measurement of dynamic mechanical properties

The dynamic mechanical properties of nylon/EPDM blends were determined using Dynamic Mechanical Thermal Analyzer (DMTA; Model-2980, supplied by TA Instrument (USA). The shape of test sample is a rectangular strip of 40×12×2 mm^3. The dual cantilever mode of deformation was used under the test temperature range from –100 to 150°C with a heating rate of 2°C/min under liquid nitrogen flow. Storage modulus (E') loss modulus (E'') and loss tangent (tanδ) of each sample were recorded in multi-frequency mode at 0.1, 1, 10 Hz.

2.5. Morphology

The morphology of the freeze-fractured cross-sections was examined using a scanning electron microscope JEOL JSM-820. Observations were made from etched samples. From N_{70} and N_{50} blends EPDM phase was extracted using xylene vapours. From N_{30} blend, nylon phase is extracted using formic acid. The samples were dried in an air oven at 120°C for 24 h and preserved in a desiccator. The solvent extracted samples were sputter coated with gold (Au) and SEM observations were made.

3. Results and discussions

3.1. Effect of blend ratio (uncompatibilized blends)

Dynamic mechanical analysis helps to study polymer/polymer miscibility in polymer blends and also measure the glass transition temperatures (T_g) of polymers. Moreover, we can obtain an idea about the storage (dynamic) modulus, loss modulus and damping behaviour (internal friction). The results of dynamic mechanical analysis add information about the behaviour of the blends and phase morphology. The effects of temperature and blend ratio on the storage modulus (E') of the samples at a frequency of 10 Hz are given in the Figure 1. The value of storage modulus, E' signifies the stiffness of the material. All the curves show three distinct regions: a glassy high modulus region where the segmental mobility is restricted, a transition zone where a substantial decrease in the E' values with increase of temperature and a rubbery region (the flow region) where a drastic decay in the modulus with temperature. The storage modulus curve of EPDM (N_0) shows a typical behaviour of an unvulcanized elastomer. EPDM shows a high modulus below its T_g followed by a drastic drop in its magnitude around –52°C. This drastic decrease in modulus with temperature around –52°C indicates distinct transition from glassy to rubbery state. At any fixed rate of deformation, the temperature at which E' starts to decrease rapidly corresponds to the glass transition temperature. But in the case of nylon, changes in the storage modulus are less severe around the glass transition zone because of its semi-crystalline nature. In the semi-crystalline materials like nylon, the crystalline chains are arranged in a regular order, and it will remain intact until the temperature reaches the melting point (T_m). Only the amorphous part undergoes segmental motion. So, in the case of nylon, the storage modulus decreases to a smaller extent than EPDM does in the transition.

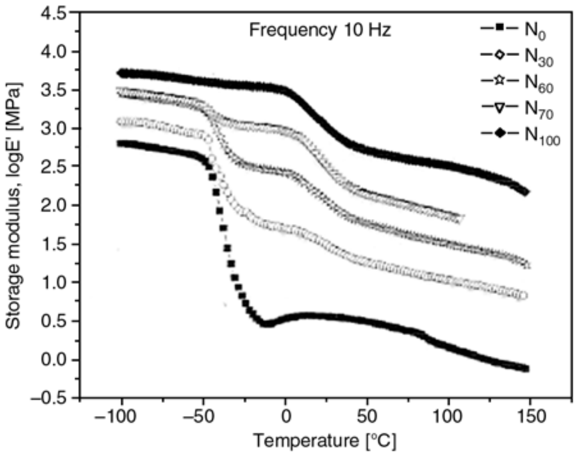

Figure 1. Storage mudulus (E') curves as function of temperature for nylon, EPDM and physical blend of nylon/EPDM

It may be noted that nylon has the maximum and EPDM has the minimum E' values. The E' values of the blends are found to be intermediate between those of pure components depending on the proportion of EPDM. At very low temperature, modulus of the blends is high. The blends show transition and plateau region corresponding to EPDM and nylon. The storage modulus decreased with increase in temperature and finally levels off at high temperature. It is seen from figure1 that the value of storage modulus decreases with increase in the concentration of EPDM content, which is more pronounced at high temperatures. On adding more

EPDM, the crystallinity is reduced. Therefore the modulus of EPDM rich blends decreases much faster at high temperatures. EPDM is having very low modulus in the rubbery plateau. The two-step curves in the figure for the blends are due to two-phase morphology indicating immiscibility. The above results are very much in agreement with those of systems based on blends of PP\EPDM studied by Papke and Karger-Kocsis [20]. The change from dispersed phase morphology in N_{30} to co-continuous morphology in N_{50} leads to an increase in modulus. In co-continuous structures the storage modulus-temperature dependence reflects a greater contribution of both components, whereas in dispersed structures, the blend modulus is dominated by the matrix component [21]. The relationship between storage modulus at a given temperature can also determine the region of phase inversion and the existence of co-continuous structures, as shown by Dedecker and Groeninckx [22] for reactively compatibilized PA6/PMMA blends.

Variation of loss modulus (E'') with temperature of nylon, EPDM and nylon/EPDM blends are given in Figure 2. The loss modulus peak corresponds to the maximum heat dissipation per unit deformation. The glass transition temperature, T_g was selected as the peak position of E'' when plotted as a function of temperature. From the figure, it is clear that N_{100} shows a peak around 13.5°C corresponding to the T_g of nylon whereas EPDM (N_0) shows a peak around –44°C. Another important observation that can be made from the figures is that nylon exhibits a strong β-relaxation around –57°C. However two distinct peaks each exactly corresponding to the glass transition temperatures of nylon and EPDM can be observed in all the blends indicating the incompatibility and immiscibility between the phases. The loss modulus increases with increase in EPDM content. Various researchers [20, 22, 23] used dynamical mechanical investigation to predict the miscibility of polymeric systems. Generally for incompatible system, the tanδ versus temperature curve shows two damping peaks corresponding to the glass transition temperatures of individual polymers [20]. When blend components are compatible, a single peak is found for the combined processes [23]. Broadening of the transition occurs in the case of partially compatible systems. Shift in the T_g to higher or lower temperatures as a function of composition also indicates the partial miscibility. Figure 3 shows the variation of loss tangent (tanδ) with temperature for the pure components and nylon/EPDM blends. The main relaxation processes in the amorphous region for the nylon and EPDM phases in the blends can be detected from the damping curves presented in Figure 3. As the temperature increases, damping goes through a maximum near T_g in the transition region, and then a minimum in the rubbery region. At T_g, micro-Brownian motion of molecular segments begins where short range diffusion can take place. The damping is low below T_g because thermal energy is insufficient to cause rotational and transnational motions of the segments [24]. As a result of this, the chain segments are frozen in. So, below T_g, the molecular slip resulting in viscous flow is low. Above T_g also the damping is low because molecular segments are very free to move about and there is little resistance for their flow. Hence, when the segments are either frozen in or are free to move, damping is low. In the

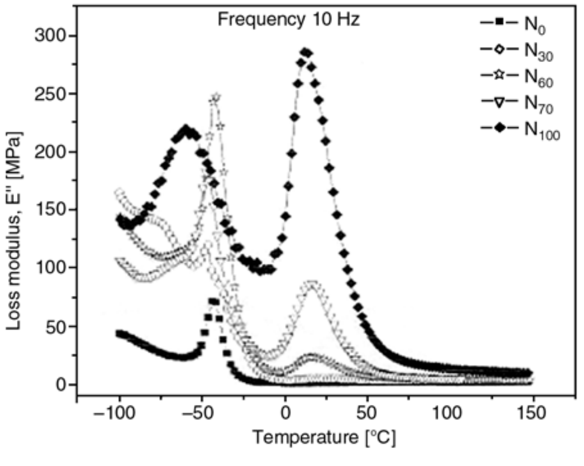

Figure 2. Loss modulus (E'') curves as function of temperature for nylon, EPDM and nylon/EPDM blend

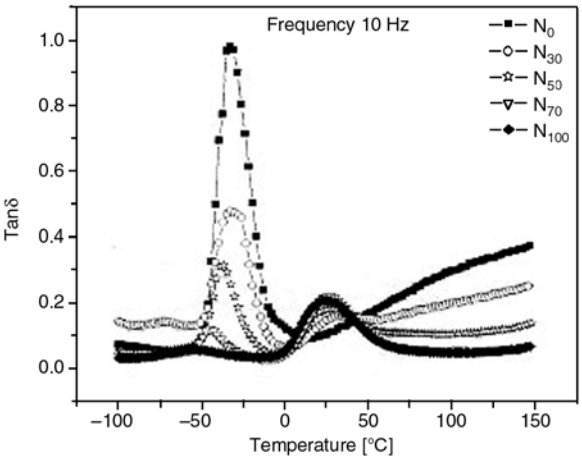

Figure 3. Tanδ curves as function of temperature for nylon, EPDM and l blends nylon/EPDM

transition region a part of the segments are free to move about and the remainder are not so free. A frozen segment stores energy through deformation and it ultimately releases it as viscous energy when it becomes free to move. The tanδ curve of EPDM shows a peak at –32°C due to the α-transition arising from the segmental motion. This α-transition corresponds to the glass transition temperature (T_g) of EPDM. Nylon shows the glass transition temperature at 26°C. Another important observation that can be made from the Figures 2, 3 is that nylon exhibits a strong β-relaxation [25] around –55°C. It is believed that the β damping peak is due to the carbonyl group of nylon forming hydrogen bonds [26]. The temperature of this peak is influenced by nylon moisture content. Some researchers related this secondary transition to movements involving carbonyl groups, which have formed hydrogen bonds with absorbed water [27]. The absence of the β-relaxation peaks in the blends indicates that addition of EPDM into nylon decreased the water uptake property of nylon as discussed else where. EPDM has higher damping than nylon because of its rubbery nature and the flexible rubber chains respond rapidly towards a cyclic loading. Since the rubber is uncrosslinked, the uncoiling and recoiling process on the application and removal of the stress makes more permanent deformation and thereby registering the highest loss tangent (tanδ_{max}) values. As can be seen from the figures, all the blend compositions show two distinct and clearly separate tanδ peaks corresponding to the T_g's of nylon and EPDM indicating that the blends are incompatible. The T_g values obtained from the loss modulus curve and tanδ curves are given in Table 2. As usual, the T_g values obtained from E'' curves are lower than those from tanδ curves. The T_g values taken from the tanδ peaks of virgin polymers and blends at different frequencies are given in Table 3. In all cases the T_g values increase with the frequency. As the mechanical frequency is increased the position of the glass-rubber transition moves to a higher temperature because the polymer chains need more energy to respond to the shorter time scale stresses imposed at higher frequencies. The shift in the T_g values upon the addition of the EPDM especially at higher concentrations of EPDM may be due to enhanced chain mobility of nylon due to the plasticizing action of the flexible EPDM phase. The EPDM has the highest damping. It is accepted that higher the tanδ_{max} the greater the mechanical losses. These losses are related to high energy input required for the motion of the molecular chains of the polymer as the transition is being approached [28]. The results also suggested that increasing the rubber content caused an increase of elastic behaviour. A small hump in the tanδ peak at lower temperature (–73°C) of N_{30} may be due to motion of the side chain and imperfection.

The damping behaviour of the blends increases with an increase in the concentration of EPDM rubber. The variation of tanδ_{max} of blend as a function

Table 2. T_g values of various nylon/EPDM blens (10 Hz)

Sample	T_g [°C] with respect to			
	EPDM		Nylon	
	From tanδ_{max}	From E''	From tanδ_{max}	From E''
N_{0}	–32	–42	–	–
N_{30}	–31	–46	31	17
N_{50}	–37	–41	27	17
N_{70}	–44	–46	26	16.7
N_{100}	–	–	26	13.5

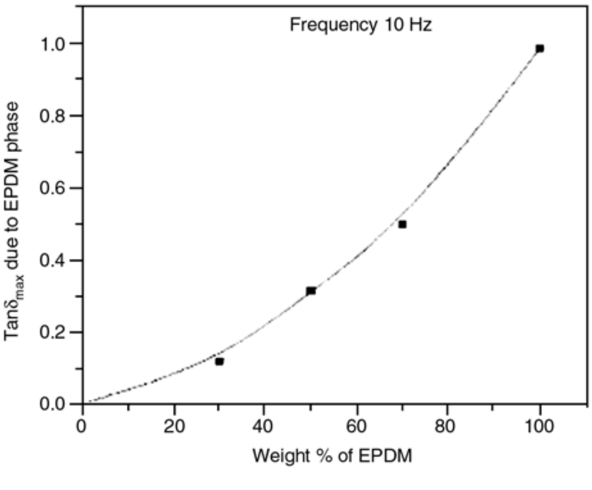

Figure 4. Variation of tanδ of nylon, EPDM and nylon/EPDM blends with temperature

Table 3. T_g [°C] values of various nylon/EPDM blends at various frequencies obtained

Frequency [Hz]	N_0	N_{30}		N_{50}		N_{70}		N_{100}
		Due to EPDM	Due to nylon	Due to EPDM	Due to nylon	Due to EPDM	Due to nylon	
0.1	–41	–45	17	–47	20	–51	17	13
1	–38	–39	20	–42	22	–47	21	19
10	–32	–31	31	–37	27	–40	26	26

of EPDM content measured at 10 Hz is shown in Figure 4. EPDM shows maximum value of tanδ indicating its excellent damping behaviour. In the blends with nylon, the crystalline plastic phase acting as physical crosslinks imposes some restriction towards cyclic loading and the tanδ_{max} decreases with increases in nylon content. The increase in the damping and tanδ_{max} with increase in EPDM content is due to the reduction in the crystalline volume of the system on increasing the concentration of EPDM whose damping is always higher than nylon.The increase in tanδ_{max} of N_{30} (70% of EPDM) in Figure 4 can be explained by morphological changes. Examination of the morphology of the blends by scanning electron microscope (Figure 5) reveals that for blends containing 70% EPDM, the nylon phase is dispersed as spherical particles (observed as semi-spherical holes after etching by hot xylene to remove the EPDM phase) in the continuous EPDM matrix. In N_{30}, the rubber phase has become continuous and its response towards a cyclic loading is more effective and there by exhibiting highest tanδ_{max}. In N_{70}, nylon is found to form the continuous phase in the blends due to its increased concentration. In this contribution of rubber towards tanδ_{max} is restricted by the crystalline plastic phase. N_{50} blend shows a co-continuous morphology and the rubber particles exist as large domains and their contribution towards tanδ_{max} is increased. SEM micrographs of the blends show a clear two phase morphology with the rubber particles being coarsely dispersed in the continuous nylon phase and having clear and sharp interfacial boundaries which may be attributed to high interfacial tension indicating poor adhesion at phase boundaries, and this is a manifestation of the incompatibility of the polymer components in these blends. It is well known that blends based on immiscible polymer pairs are characterized by great interfacial tension, which makes the dispersion during the blending operation difficult, and contributes to unstable morphology and poor adhesion [29].

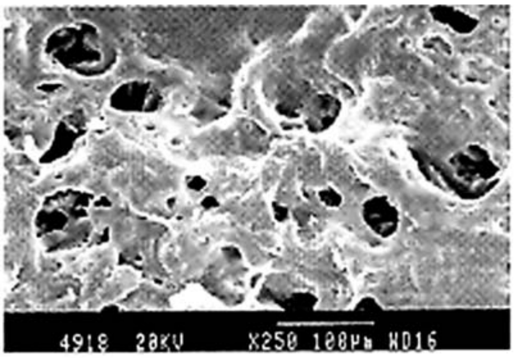

30 nylon/70 EPDM (N_{30})

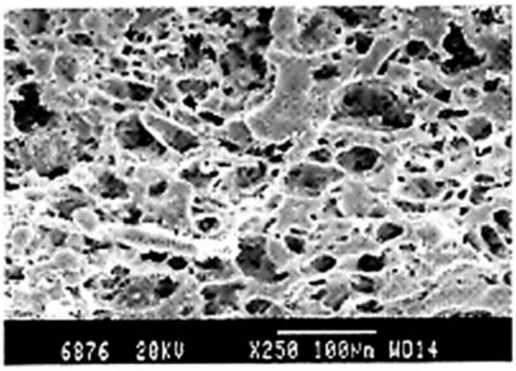

50 nylon/50 EPDM (N_{50})

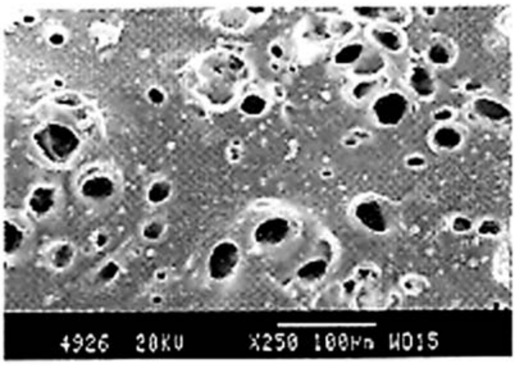

70 nylon/30 EPDM (N_{70})

Figure 5. Scanning electron micrograph of nylon copolymer/EPDM blends at a magnification of 250 times

The activation energy, E for the glass transition of the blends can be calculated from the Arrhenius equation (1):

$$\log f = \log A - 2.030\frac{E}{RT} \tag{1}$$

where f is the experimental frequency of transition, A, is a constant, E is the activation energy, R is the universal gas constant, T is the temperature corresponding to the maximum of the tanδ curve in Kelvin scale [K]. The plots of $\log f$ versus $1/T$ were constructed and the values of the activation energies were calculated from the slope of the plots. This slope corresponds to the activation energy of the viscous flow that accompanies the glass transition. The Arrhenius plot corresponding to EPDM transition in 70/30 nylon/EPDM blend is given in the Figure 6. Activation energy values are given in the Table 4. The blends show higher activation energy than the EPDM. Due to the amorphous nature of the EPDM, it is less sensitive to tempera-

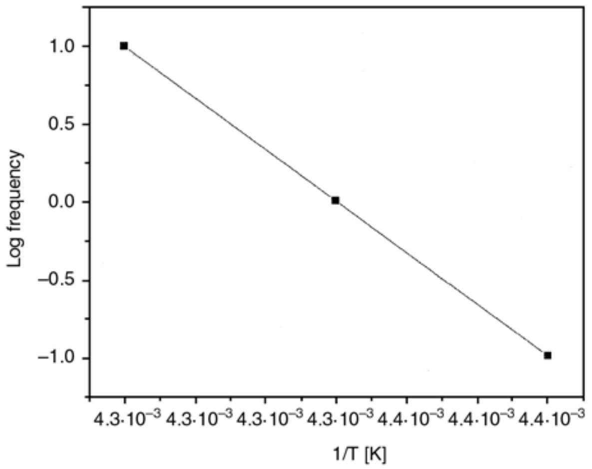

Figure 6. Arrhenious plot corresponding to EPDM transition in 70/30 nylon/EPDM blends

Table 4. Activation energy for the transition of EPDM phase in nylon/EPDM blends

Sample	Activation energy (ΔE) [kJ/mol^{-1}] for EPDM phase transition
N_{70}	423
N_{50}	261
N_{30}	189
N_0	51

ture hence the activation energy decreases with increase in EPDM content. The chain flexibility increases with increase in the rubber content. As the flexibility increases, the crystallinity decreases. As a result of this the activation energy decreases.

3.1.1. Theoretical analysis of storage modulus

Model studies were carried out to assess the behaviour of the two-phase blend from the component property data. The various composite models such as parallel, series, Coran's and Takayanagi's have been used to predict the viscoelasic behaviour of the binary blends. The upper bound of the storage modulus is given by the rule of mixtures (Equation (2)):

$$E_u = E_1\phi_1 + E_2\phi_2 \tag{2}$$

where E_u is the property of the blend and E_1 and E_2 are the corresponding properties of the components ϕ_1 and ϕ_2 respectively. and represent the volume fraction of components 1 and 2 respectively. This equation is applicable to the materials in which the components are arranged parallel to the applied stress. The applied stress elongates each component by the same amount. In the lowest lower bound series model, the blend components are arranged in series (Reuss prediction) perpendicular to the direction of the applied force. The equation for the series combination of the components is given by Equation (3):

$$\frac{1}{E_L} = \frac{\phi_1}{E_1} + \frac{\phi_2}{E_2} \tag{3}$$

where E_L is the moduli of the blend in the series model. For both these models, there is no relation between the morphology and the property.

According to Halpin-Tsai model [30, 31], the Equation (4) that relates the morphology of the polymer blend to the properties is:

$$\frac{E_1}{E} = \frac{1 + A_i B_i \phi_2}{1 - B_i \phi_2} \tag{4}$$

where

$$B_i = \frac{\frac{E_1}{E_2} - 1}{\frac{E_1}{E_2} + A_i} \tag{5}$$

In the Equation (5) the subscript 1 and 2 refer to the continuous and dispersed phases respectively. The constant A_i is determined by the morphology of the system. For elastomer domains, dispersed in a continuous hard matrix, $A_i = 0.66$ and when the hard material forms the dispersed phase, A_i is 1.5. This model was also useful in determining the properties of polymer blends that contained both continuous and discontinuous phases. This model has also been successfully applied by several researchers to systems [32, 33] of polymer composites.

In Coran's model [34], the mechanical properties are generally in between the upper bound parallel model (E_U) and the lower bound series model (E_L) (Equation (6)):

$$E = f(E_U – E_L) + E_L \tag{6}$$

where 'f' can very between zero and unity. The value of 'f' is given by Equation (7):

$$f = V_H^n (nV_S + 1) \tag{7}$$

where n contains the aspects of phase morphology. V_H and V_S are the volume fractions of hard phase and soft phase respectively. It can be seen from Figure 7 that the experimental data are very close to the Coran's modal with an n value of 2.2.

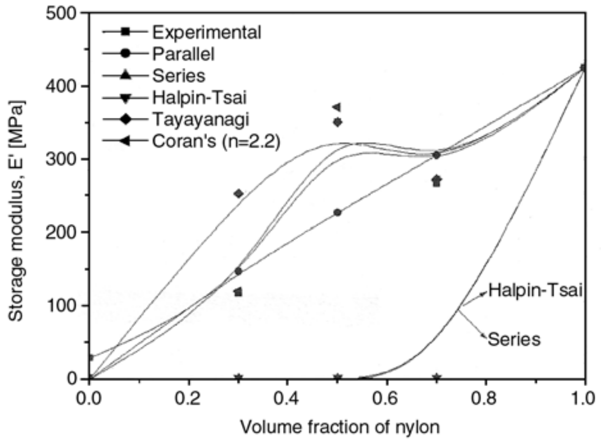

Figure 7. Experimental and theoretical curves of storage modulus of nylon/EPDM blends as a function of volume fraction of nylon at room temperature (28°C)

The viscoelastic behaviour of the heterogeneous polymer blend can be predicted using Takayanagi model [35] in which the concept of percolation is introduced. According to this model (Equation (8)):

$$E = (1-\lambda)E_1 + \frac{\lambda}{\frac{1-\phi_2}{E_1} + \frac{\phi_2}{E_2}} \tag{8}$$

where E_1 is the modulus of the matrix phase, E_2 is the modulus of the dispersed phase and the values of λ and ϕ_2 are related to the degree of series-parallel coupling.

The degree of parallel coupling of the model can be expressed by Equation (9):

$$[\%]\text{parallel} = \left[\frac{\phi_2(1-\lambda)}{1-\phi_2\lambda}\right]\cdot 100 \tag{9}$$

The curves resulting from the different theoretical models and that of the experimental data for the variation of storage modulus at 25°C with volume fraction of nylon are given in Figure 7. Coran's model ($n = 2$) fits well with the experimental curve and the Takayanagi model with 45% parallel coupling agrees to some extent with the experimental curve. The series model is the lowest bound over the entire composition range.

3.2. Effect of compatibilization

As discussed in the above section, the nylon copolymer/EPDM blend systems are incompatible. The incorporation of a compatibilizer into an immiscible blend reduces the interfacial energy of the phases, stabilizes the morphology against coalescence and improves the interfacial adhesion. As a result, systems with improved and reproducible properties are obtained.

Dynamic mechanical analysis (DMA) is sensitive to molecular motions and transitions [36] has been chosen as a tool for characterizing blend compatibilisation. The objective of the current work is to use DMA to study the glass transition behaviour of immiscible polymer blends in an effort to characterize blend compatibilisation on the molecular level and to make a correlation between phase morphology and dynamic mechanical properties.

The variation of storage modulus as a function of temperature for 70/30 nylon/EPDM blends compatibilized with different concentrations of EPM-g-MA is shown in Figure 8. The E' values of compatibilized N_{70} blends are higher than that of uncompatibilized blend at the same temperature. The addition of EPM-g-MA makes the blend technologically compatible to some extent even though molecular level miscibility cannot be achieved. Even by the addition of 1% compatibilizer, the storage modulus of the blends shifted towards the lower temperatures, i. e, below the glass transition temperature of nylon. The increase in the modulus upon the addition of the compatibilizer is due to the increase in the interfacial adhesion caused by the emulsifying effect of the copolymer formed by the reaction between EPM-g-MA and nylon. The presence of compatibilizer improves the interfacial adhesion by enhancing the interfacial thickness and thereby facilitating the stress transfer between the components. Thus EPM-g-MA, improved the inter-

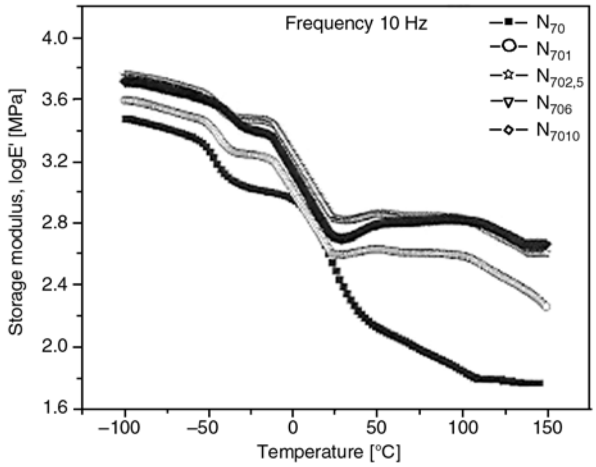

Figure 8. Effect of compatibilisation on the variation of storage modulus as a function of temperature in N_{70} blends

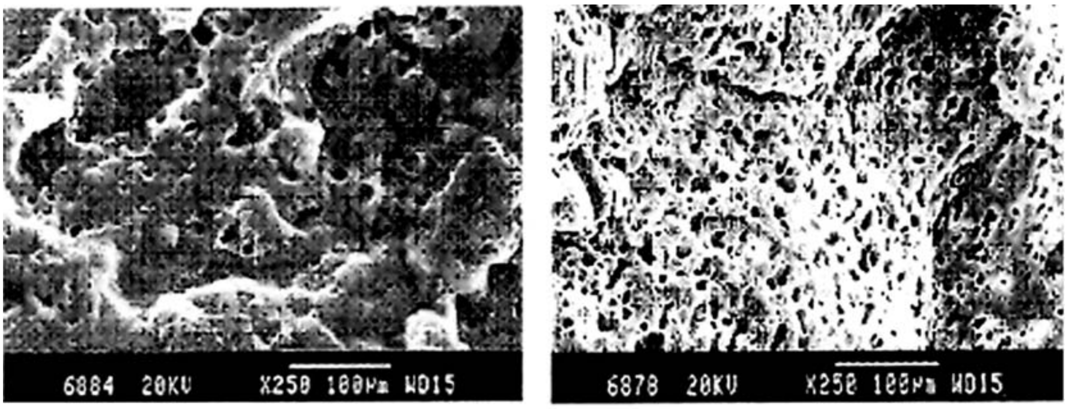

1% compatibilizer

2.5% compatibilizer

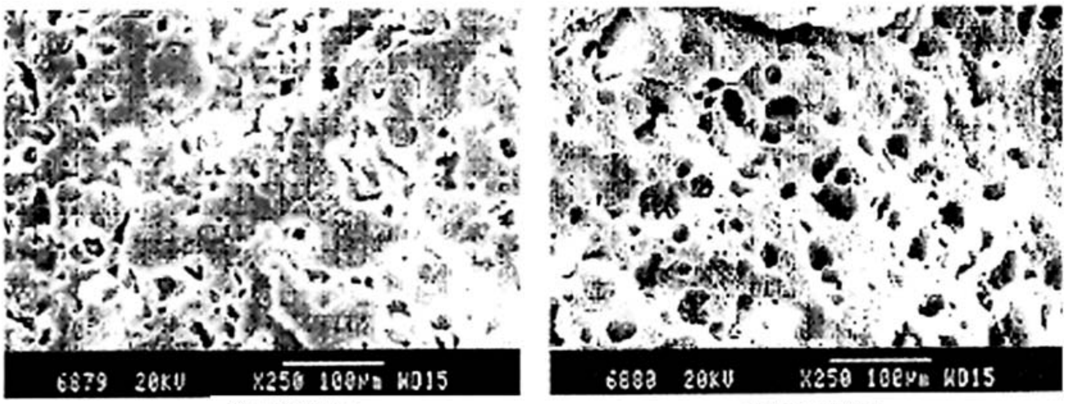

5% compatibilizer

10% compatibilizer

Figure 9. Scanning electron micrographs of N_{70} blend containing different levels of EPM-g-MA

facial adhesion, consequently, the storage modulus of the blends enhanced. The increased interfacial interaction is evident from the small and uniform dispersion of EPDM particles upon the addition of EPM-g-MA (Figure 9). A decrease in E' by the addition of 10 wt% EPM-g-MA indicates the formation of micelles in the nylon matrix. At higher loading of the compatibilizer, modulus value decreases due to the formation of agglomerates of the compatibilizer molecule.

Now let us consider the effect of compatibilisation on the T_g's of the blends. Figure 10 depicts the change of loss modulus (E'') as function of temperature for nylon/EPDM blends compatibilized by EPM-g-MA. The E'' values of the compatibilized systems are higher than those of N_{70} uncompatibilized blend. The shift in the T_g values of the nylon phase of the compatibilized blends compared to the uncompatibilized blends indicate the strong interaction between the nylon and EPDM as a result of reactive compatibilisation. Thus a shifting of T_g values of the components is taken as an indication of miscibility enhancement and therefore can be considered as an evidence for compatibilisation. Due to the reaction the mobility of the nylon phase decreases.

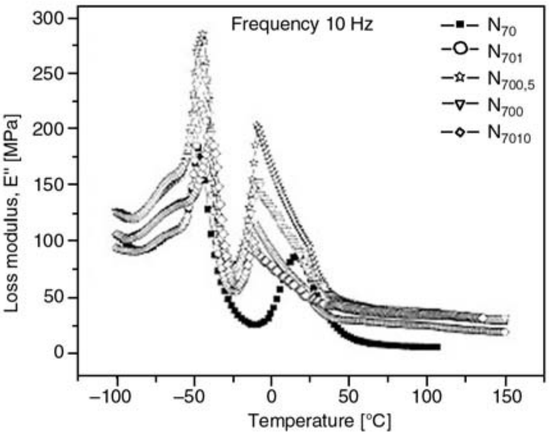

Figure 10. Effect of compatibilisation on the variation of loss modulus as a function of temperature in N_{70} blends

There is no change in the T_g values of EPDM phase of the compatibilized blends in the loss modulus curve. This is because, at the lower T_g in the compatibilized blends, there are two types of constraints imposed on the motions of molecular segments in the vicinity of the interface. One is due to the presence of another phase and other is due to the presence of chemical bonds between the two phases. As the blend goes through the lower T_g, one phase retains its glassiness. The constraints imposed by the glassy phase apparently dominates the presence of chemical bonds between phases. Therefore, no difference is observed when one compares the lower T_g behaviour of the compatibilized and uncompatibilized blends. And below T_g, the molecular mobility is reduced. So the rate of free volume changes with temperature is very small. Therefore, when both blend components are below their respective T_g, free volume effects are small and E'' is relatively constant with temperature. Since the compatibilisation reduces interfacial energy and creates a finer dispersion by increasing the interfacial area [37], one can expect an overall volume of the interaction zone to increase when copolymer is added. When the blend goes through the high T_g, all the molecules are relaxed. In the compatibilized blends the linked segments do not have the degree of mobility as the unlinked segments have, so that the effective number of segments free to completely relaxed has decreased. So there is a shift towards lower T_g. The T_g values obtained (Table 5) from E'' *vs.* temperature is always less than that obtained from tanδ maximum.

DMA has become a classical method for the determination of miscibility because the height and position of the mechanical damping peaks are affected remarkably by miscibility, intermolecular interaction, interface feature and morphology. The variation of tanδ as a function of temperature of the compatibilized blends is given in Figure 11. The compatibilized blends also show the presence of two peaks corresponding to the T_g's of nylon and EPDM similar to those of the uncompatibilized blends. This indicated that compatibilisation did not alter the degree of miscibility. The broadening of the peaks is an indication of the compatibilisation. The general broadening of the tanδ peaks is associated with increased molecular mixing [38], which is expected. As the compatibility increases, the interpenetration of the components increases [39]. There is no appreciable shift in the T_g towards the average value. This emphasizes that significant miscibility increase does not occur for the compatibilized blends. However, domain boundary mixing [40] or interface mixing [41] have been shown to cause an increased temperature dependence of storage modulus and increased level of loss modulus between T_g for compatibilized relative to uncompatibilized blends. From the Figure 11 it is clear that 2.5% compatibilizer loaded blend shows the highest tanδ than other blends in various temperatures. This may be due to the maximum interfacial interaction provided by the compatibilizer. This is evident from the SEM analysis also. Maximum particle size reduction is obtained for 2.5% of compatibilizer (Figure 9).

We can conclude that both electron microscopy and dynamical mechanical analysis clearly show that the system is still phase separated even in the presence of the compatibilizer and tanδ curve also indicates that compatibilizer addition could not make the system completely miscible. This is in agreement with the conclusions made by Paul [42] that if two polymers are far from being miscible, then no copolymer is likely to make a single phase system. In a completely immiscible system, the main role of the copolymer is to act as an interfacial agent.

Table 5. Effect of compatibilisation on the T_g values of EPDM and nylon in N_{70} blends at 10 Hz

Blends	Glass transition temperature [°C]			
	From E" vs. T curve		From tanδ vs. T curve	
	EPDM phase	Nylon phase	EPDM phase	Nylon phase
N_{70}	–46	16.7	–40	26
1% Compatibiliser	–44	–11	–41	23
2.5% Compatibiliser	–44	–9.3	–42	24
5% Compatibiliser	–44	–9.3	–42	24
10% Compatibiliser	–38	–12	–36	22

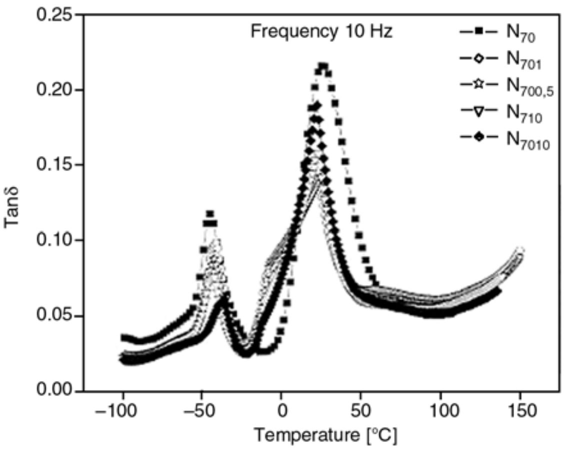

Figure 11. Effect of compatibilisation on the variation of tanδ as a function of temperature in N_{70} blends

3.3. Degree of entanglement density

Degree of entanglement of the polymer blends can be obtained from swelling measurements, stress-strain curve and also from dynamic mechanical analysis. We can use the storage modulus data for determining the entanglement density using the Equation (10):

$$N = \frac{E'}{6RT} \tag{10}$$

where E' is the storage modulus obtained from the plateau region of E' versus temperature curve, R is the universal gas constant and T, is the absolute temperature. A higher degree of entanglement is exhibited by the compatibilized blends when compared to the uncompatibilized blends. This is because by the addition of compatibilizer the entanglement between the homopolymers increases and a better adhesion is achieved as a result of decrease in the interfacial tension. The value for degree entanglement between nylon and EPDM are given in the Table 6. From the morphology studies it is clear that immiscible polymers exhibit a coarse dispersion. By the addition of the compatibilizer the particle size decreased leading to a better adhesion. Oommen *et al.* [43] reported that the entanglement density increases as a result of compatibilisation. It is interesting to note that, the entanglement density increases up to 2.5 wt% of compatibilizer concentration followed by a decrease at higher loading. This indicates clearly that the compatibilizer leaves the interface after critical micelle concentration (CMC). Our earlier studies revealed that the minimum amount of compatibilizer (CMC) required to modify the interface is 2.5% of EPM-g-MA.

Table 6. Entanglement Density of 70/30 nylon/EPDM blends at 10 Hz

Temperature [°C]	Compatibiliser [wt%]	Entanglement density [moles/m^3]
239	0	123
	1	152
	2.5	273
	5	251
	10	234

4. Conclusions

1. In uncompatibilized blends, nylon shows the maximum and EPDM shows the minimum storage modulus. The storage modulus of blends was found to be intermediate between the pure components.
2. For the uncompatibilized blends, loss modulus and tanδ values did not able to give any information about the favourable interactions between nylon and EPDM, as their transition peaks (T_g of nylon ~26°C, T_g of EPDM ~–32°C and β-relaxation of nylon ~–57°C) experienced no shift as a function of blend ratio.
3. As the concentration of the EPDM rubber increases the storage modulus decreases and the damping and loss modulus increases.
4. The experimental data of uncompatibilized blends were theoretically modeled and observed that Coran's model (n = 2.2) was best suited for the present system and the Takayanagi model with 45% parallel coupling agrees to some extent.
5. The addition of EPM-g-MA as compatibilizer improved the viscoelastic properties indicating improved interaction between the two components in the compatibilized system.
6. A higher degree of entanglement is exhibited by the compatibilized blends when compared to the uncompatibilized blends.
7. Morphologies of the blends have got a profound influence on the dynamic mechanical properties.

References

[1] Craver C. D., Carraher C.: Applied polymer science-21st century. Elsevier, New York (2000).

[2] Holden G., Legge N. R., Quirk R. Q., Schroeder H. E.: Thermoplastic elastomers. Hanser-Gardner Publications, Cincinnati (1996).

[3] Yang H., Lai M., Liu W., Sun C., Liu J.: Morphology and thermal and mechanical Properties of PBT/HIPS and PBT/HIPS-g-GMA blends. Journal of Applied Polymer Science, **85**, 2600–2608 (2002).

[4] John B., Varughese K. T., Oommen Z., Pötschke P., Thomas S.: Dynamic mechanical behavior of high-density polyethylene/ethylene vinyl acetate copolymer blends: The effects of the blend ratio, reactive compatibilization, and dynamic vulcanization. Journal of Applied Polymer Science, **87**, 2083–2099 (2003).

[5] George J.: Compatibilisation of high density polyethylene/nitrile rubber blends. PhD thesis, Mahatma Gandhi University (2003).

[6] Ramirez-Vargas E. R., Sandoval-Arellano Z., Hernandez-Valdez J. S., Martinez-Colunga J. G., Sanchez-Valdes S.: Compatibility of HDPE/postconsumer HDPE blends using compatibilizing agents. Journal of Applied Polymer Science, **100**, 3696–3706 (2006).

[7] Diaz M. F., Barbosa S. E., Capiati N. J.: Addition compatibilization of PP/PS blends by tailor-made copolymers. Polymer Engineering and Science, **46**, 329–336 (2006).

[8] Mirzazadeh H., Katbab A. A.: PP/EPDM-based thermoplastic dynamic vulcanizates with organoclay: morphology, mechanical and viscoelastic properties. Polymers for Advanced Technologyes, **17**, 975–980 (2006).

[9] Yang Y-L., Lin Y., Sell C., Hiver J-M., Bai S-L.: Dynamic mechanical properties and morphology of high-density polyethylene/$CaCO_3$ blends with and without an impact modifier. Journal of Applied Polymer Science, **103**, 3907–3914 (2007).

[10] Al-Malaika S., Kong W.: Reactive processing of polymers: effect of in situ compatibilization on characteristics of blends of polyethylene terephthalate andethylene-propylene rubber. Polymer, **46**, 209–228 (2005).

[11] Rajan G. S., Vu Y. T., Mark J. E., Myers C. L.: Thermal and mechanical properties of polypropylene in the thermoplastic elastomeric state. European Polymer Journal, **40**, 63–71 (2004).

[12] Nandan B., Kandpal L. D., Mathur G. N.: Glass transition behaviour of poly(ether ether ketone)/poly(aryl ether sulphone) blends: dynamic mechanical and dielectric relaxation studies. Polymer, **44**, 1267–1279 (2003).

[13] Kumar M. S. C., Alagar M., Prabu A. A.: Studies on dynamic mechanical and mechanical properties of vinyloxyaminosilane grafted ethylene propylene diene terpolymer/linear low density polyethylene (EPDM-g-VOS/LLDPE) blends. European Polymer Journal, **39**, 805–816 (2003).

[14] Karger-Kocsis J., Kiss L.: Dynamic mechanical properties and morphology of polypropylene block copolymers and polypropylene/elastomer blends. Polymer Engineering and Science, **27**, 254–262 (1987).

[15] Guo T-Y., Song M-D., Hao G-J., Zang B-H.: Compatibility and mechanical properties of polyamide-6/polystyrene/diblock poly(styrene-b-ethylene oxide) copolymer blends. European Polymer Journal, **37**, 241–246 (2001).

[16] Gopakumar T. G., Ponrathnum S., Lele A., Rajan C. R., Fradet A.: In situ compatibilization of poly (phenylene sulphide)/wholly aromatic thermotropic liquid crystalline polymer blends by reactive extrusion: morphology, thermal and mechanical properties. Polymer, **40**, 357–364 (1999).

[17] Seo Y.: TLCP ternary blends for in situ composites: In situ compatibilizer. Journal of Applied Polymer Science, **70**, 1589–1595 (1998).

[18] Tjong S. C., Li R. K. Y., Xie X. L.: Compatibilizing effect of styrene-maleic anhydride copolymer on the properties of polyamide-6/liquid crystalline copolyester composites. Journal of Applied Polymer Science, **77**, 1964–1974 (2000).

[19] Moly K. A., Bhagawan S. S., Groeninckx G., Thomas S.: Correlation between the morphology and dynamic mechanical properties of ethylene vinyl acetate/linear low-density polyethylene blends: Effects of the blend ratio and compatibilisation. Journal of Applied Polymer Science, **100**, 4526–4538 (2006).

[20] Papke N., Karger-Kocsis J.: Thermoplastic elastomers based on compatibilized poly(ethylene terephthalate) blends: effect of rubber type and dynamic curing. Polymer, **42**, 1109–1120 (2001).

[21] Quintens D., Groeninckx G., Guest M., Aerts L.: Mechanical behavior related to the phase morphology of PC/SAN polymer blends. Polymer Engineering and Science, **30**, 1474–1483 (1990).

[22] Dedecker K., Groeninckx G.: Reactive compatibilisation of A/(B/C) polymer blends. Part 2. Analysis of the phase inversion region and the co-continuous phase morphology. Polymer, **39**, 4993–5000 (1998).

[23] Varughese K. T., Nando G. B., De P. P., De S. K.: Miscible blends from rigid poly (vinyl chloride) and epoxidised NR. Journal of Material Science, **23**, 3894–3900 (1988).

[24] Ferry J. D.: Viscoelastic properties of polymers. John Wiley, New York (1980).

[25] Dickie R. A.: Heterogeneous polymer-polymer composites. I. Theory of viscoelastic properties and equivalent mechanical models. Journal of Applied Polymer Science, **17**, 45–63 (1973).

[26] Bell J. P., Murayama T.: Relation between dynamic mechanical properties and dye diffusion behavior in acrylic fibers. Journal of Applied Polymer Science, **12**, 1795–1799 (1968).

[27] Gadekar R., Kulkarni A., Jog J. P.: Blends of nylon with polyethylene: Effect of compatibilization on mechanical and dynamic mechanical properties. Journal of Applied Polymer Science, **69**, 161–168 (1998).

[28] Sombatsompop N.: Dynamic mechanical properties of SBR and EPDM Vulcanisates filled with cryogenically pulverized flexible polyurethane foam particles. Journal of Applied Polymer Science, **74**, 1129–1139 (1999).

[29] Hu G-H., Sun Y-J., Lambla M.: Effects of processing parameters on the in situ compatibilization of polypropylene and poly(butylene terephthalate) blends by one-step reactive extrusion. Journal of Applied Polymer Science, **61**, 1039–1047 (1996).

[30] Nielsen L. E.: Morphology and the elastic modulus of block polymers and poly blends. Rheologica Acta, **13**, 82–92 (1974).

[31] Halpin J. C.: Structure-property relations and reliability concepts. Journal of Composite Materials, **6**, 208–2031 (1972).

[32] Kalaprasad G., Joseph K., Thomas S., Pavithran C.: Theoritical modelling of tensile properties of short sisal fibre reinforced low density polyethylene composites. Journal of Material Science, **32**, 4261–4267 (1997).

[33] Nair K. C. M., Divan S. M., Thomas S.: Tensile properties of short sisal fiber reinforced polystyrene composites. Journal of Applied Polymer Science, **60**, 1483–1497 (1996).

[34] Stephens H. L., Bhowmick A. K.: Handbook of elastomers: New developments and technology Marcel Dekker, New York (1988).

[35] Dickie R. A.: Heterogeneous polymer-polymer composites. I. Theory of viscoelastic properties and equivalent mechanical models. Journal of Applied Polymer Science, **17**, 45–763 (1973).

[36] Murayama T.: Dynamic Mechanical analysis of polymer material. Elsevier, New York (1978).

[37] Paul D. R.: Interfacial agents (compactibilizers) for polymer blends. in 'Polymer Blends' (eds.: Paul D. R., Newman S.) Academic Press INC, New York, Vol 2, 35–62 (1978).

[38] Thomas D. A., Sperling C. H.: Interpenetrating polymer networks. in 'Polymer Blends' (eds.: Paul D. R., Newman S.) Academic Press INC, New York, Vol 2, 1–33 (1978).

[39] Wu S.: Interfacial energy, structure and adhesion between polymers. in 'Polymer Blends' (eds.: Paul D. R., Newman S.) Academic Press INC, New York, Vol 1, 243–293 (1978).

[40] Hashimoto T., Tsukahara Y., Tachi K., Kawai H.: Structure and properties of tapered block polymers. 4. 'Domain-boundary mixing' and 'mixing-in-domain' effects on microdomain morphology and linear dynamic mechanical response. Macromolecules, **16**, 648–657 (1983).

[41] Feng D., Wilkens G. L., Crivello J. V.: Structure-property behaviour of free radical synthesized polydimethylsiloxane-polystyrene multiblock polymers: 1. Effect of the siloxane block length. Polymer, **30**, 1800–1813 (1989).

[42] Newman S.: Rubber modifications of plastics. in 'Polymer Blends' (eds.: Paul D. R., Newman S.) Academic Press INC, New York, Vol 2, 63–89 (1978).

[43] Oommen Z., Groninckx G., Thomas S.: Dynamic mechanical and thermal properties of physically compatibilized natural rubber/poly (methyl methacrylate) blends by the addition of natural rubber-graft-poly (methyl methacrylate). Journal of Polymer Science Part B: Polymer Physics, **38**, 525–536 (2000).

eXPRESS Polymer Letters Vol.1, No.10 (2007) 654–659
Available online at www.expresspolymlett.com
DOI: 10.3144/expresspolymlett.2007.89

Adhesion properties of styrene-butadiene rubber (SBR)/ Standard Malaysian Rubber (SMR L)-based adhesives in the presence of phenol formaldehyde resin

B. T. Poh, L. N. Ong*

School of Industrial Technology Universiti Sains Malaysia, 11800 Penang, Malaysia

Received 8 June 2007; accepted in revised form 7 August 2007

Abstract. The adhesion properties, i. e. viscosity, tack and peel strength of styrene-butadiene rubber (SBR)/Standard Malaysian Rubber (SMR L)-based pressure-sensitive adhesive was studied using phenol formaldehyde resin as the tackifying resin. Toluene was used as the solvent throughout the experiment. SBR composition in SBR/SMR L blend used was 0, 20, 40, 60, 80, 100%. Three different resin loadings, i. e. 40, 80 and 120 parts per hundred parts of rubber (phr) were used in the adhesive formulation. The viscosity of adhesive was determined by a HAAKE Rotary Viscometer whereas loop tack and peel strength of paper/polyethylene terephthalate (PET) film were measured using a Lloyd Adhesion Tester operating at 30 cm/min. Results indicate that the viscosity of adhesive decreases with increasing % SBR whereas loop tack passes through a maximum value at 20% SBR for all resin loadings. Except for the control sample (without resin), the peel strength shows a maximum value at 60% SBR for the three modes of peel tests. For a fixed % SBR, adhesive sample containing 40 phr phenol formaldehyde resin always exhibits the highest loop tack and peel strength, an observation which is associated to the optimum wettability of adhesive on the substrate.

***Keywords:** rubber, adhesion, coating, tackifier*

1. Introduction

Recently, we have carried out several investigations on the viscosity, tack, peel and shear strength of natural rubber (NR) and epoxidized natural rubber (ENR) [1–5]. It has been shown that the viscosity and tack of natural rubber-based adhesive increases with resin content due to the concentration effect of tackifier resin. The peel strength generally increases with resin content, an observation which is attributed to the wettability of substrates. On the other hand, shear strength of the adhesive decreases gradually with increasing resin content as a result of decreasing cohesive strength of adhesive as resin loading is increased. For a fixed resin content, shear strength increases with increasing coating thickness suggesting that shear strength is thickness-dependent. With regard to ENR-based pressure-sensitive adhesives, results show that peel strength passes through a maximum at 40 phr of tackifying resin. However, the shear strength indicates a gradual decrease with increasing resin loading due to the decrease in cohesive strength of adhesive. ENR 25 consistently exhibits higher peel strength and shear strength than ENR 50. The viscosity and loop tack of ENR-based adhesive increases with increasing zinc oxide concentration. For the peel strength, it increases with zinc oxide concentration up to 30–40 phr of filler and drops after the maximum value. However, with respect to the effect of rubber blending on the adhesion property of pressure-sensitive adhesives, there is no study reported so far. We have thus carried out a

---

*Corresponding author, e-mail: btpoh@usm.my

systematic investigation to evaluate the effect of % SBR on the viscosity, tack and peel strength of SBR/SMR L-based pressure sensitive-adhesive.

2. Experiment

2.1. Materials

SMR L grade was used as the natural rubber. The technical specification [6–7] of the rubber is given in Table 1.

Table 1. Technical specifications of SMR L

Dirt content (max. %wt)	0.03
Ash content (max. %wt)	0.50
Nitrogen (max. %wt)	0.60
Volatile matter (max. %wt)	0.80
Plasticity retention index (min. %)	30
Mooney viscosity, $M_{L,1+4}$ (100°C)	78

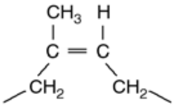

Figure 1. Structure of SMR L

The molecular structure of SMR L is given in Figure 1. It is a repeating unit of isoprene monomer to form *cis*-1,4 polyisoprene.

Buna Hüls 1502 grade SBR was supplied by Bayer. It has a 33.5% by weight of target bound styrene. The density, ash content, Mooney viscosity and volatile matter of the rubber are 0.9 g/cc, 0.5%, 50 and 0.2% respectively.

Commercial grade phenol-formaldehyde resin was chosen as the tackifier. Its specific gravity, refractive index and specific heat are 1.2, 1.6 and 0.5 respectively. Toluene was used as the solvent throughout the study to prepare the rubber-based pressure-sensitive adhesives.

2.2. Adhesive preparation

The rubbers were masticated on a 2-roll mill for 10 minutes. Different blend ratios of SBR/SMR L corresponding to 0, 20, 40, 60, 80 and 100% SBR were prepared. For each adhesive formulation, 5 g of the rubber blend was used. The rubber blend was then dissolved in 30 ml of toluene. The rubber solution was kept in a conditioned room for 24 hours before the addition of phenol-formaldehyde resin. In order to study the effect of phenol-formaldehyde concentration on the adhesion properties, three different weights i.e. 2, 4 and 6 g corresponding to 40, 80 and 120 parts per hundred parts of rubber [phr] of resin were added to the rubber solution to prepare the adhesives. After the addition of resin, constant stirring with glass rod was carried out to ensure a homogeneous adhesive was formed. The adhesive was left for at least 3 hours prior to testing.

2.3. Testing

2.3.1. Viscosity

The viscosity of adhesive was measured by a HAAKE Rotary Viscometer (Model PK 100). Both the platform and the spindle head were cleaned with isopropyl alcohol to prevent contamination of the adhesive to be tested. Then, a little adhesive was dribbled onto the testing surface as well as the spindle head. The platform was raised up to touch the spindle head. Any excess adhesive was wiped off with a clean tissue and testing was carried out for one minute or ten rounds of spinning. At least five readings were taken and the average viscosity was computed.

2.3.2. Tack

Loop tack test is essentially a peel test involving low contact pressure and short application time [8]. A PET film with dimension of 4 cm × 25 cm was coated at the centre of the film (4 cm × 4 cm) with a coating thickness of 60 µm using a SHEEN Hand Coater. The coated surface area was covered by a release paper and conditioned at room temperature for 30 minutes prior to testing. Then, a loop configuration with the adhesive exposed was formed after the removal of release paper. The top of the loop was taped and clamped in a Lloyd Adhesion Tester (Model LRXPlus with NEXYGEN software). The clamp was lowered at a constant speed of 10 cm/min until the adhesive area touched the glass panel. The contact area was made without any force other than the pushing force of the loop. The loop was then pulled at 30 cm/min until debonding from the glass panel occurred. The three highest peaks from the load-propagation graph were taken to calculate the average debonding force. The loop tack value is expressed as the debonding force per area of contact [N/m^2].

2.3.3. Peel strength

The substrates used for the peel tests were PET film and release paper which formed the base stock and face stock respectively. Three testing modes, i. e. T-Peel, 90° and 180° Peel Tests were used to determine the peel strength of adhesives. The dimensions of the substrates for the T- and 90° Peel Tests were 20 cm × 4 cm. In the case of 180° Peel Test, the dimensions of PET film and paper substrates were 25 cm × 4 cm and 12 cm × 6 cm respectively. A SHEEN Hand Coater was used to coat the PET film at 60 μm thickness from the end of the film with a coating area of 10 cm × 4 cm. The coated PET film was covered by the paper substrate. The testing sample was then conditioned at room temperature for 24 hours before testing on a Lloyd Adhesion Tester operating at 30 cm/min. As in the case of tack determination, the three highest peaks from the load-propagation graph were recorded to compute the average peeling force. Peel strength is defined as the average load per width of the bondline required to separate progressively a flexible member from a rigid member or another flexible member (ASTM D 907).

3. Results and discussion

The effects of blend ratio and phenol formaldehyde resin loading on the viscosity, tack and peel strength of the pressure-sensitive adhesives prepared from SBR/SMR L blends are discussed below.

3.1. Viscosity of adhesive

Figure 2 shows the dependence of viscosity of adhesive on the % SBR for various phenol formaldehyde resin loadings. It is obvious that all resin loadings (including the control sample), the viscosity of adhesive decreases gradually with SBR composition. This observation is explained by lower molecular weight of SBR (Mooney viscosity = 50) compared to that of SMR L (Mooney viscosity = 78). Figure 2 also indicates that viscosity of adhesive increases with increase in resin loading. This observation is consistent with our previous study on SMR 10 and SMR 20-based pressure-sensitive adhesives [1–2]. The concentration effect of the tackifying resin accounts for this increase in viscosity. It is also observed that there is a significant increase in viscosity from 0–40 phr of resin loading, especially below 60% SBR composition. This sudden increment may be attributed to the onset of chain entanglement [9] between SMR L and phenol formaldehyde resin. Further addition of resin is accompanied by the steady increase in viscosity as shown by the 80 and 120 phr resin loading. This is especially so when SBR composition is increased beyond 60%. In this case, chain entanglement does not govern the increase in viscosity as resin loading is increased. In other words, SBR chain does not entangle with the resin molecule and increment in viscosity is essentially a concentration effect phenomenon.

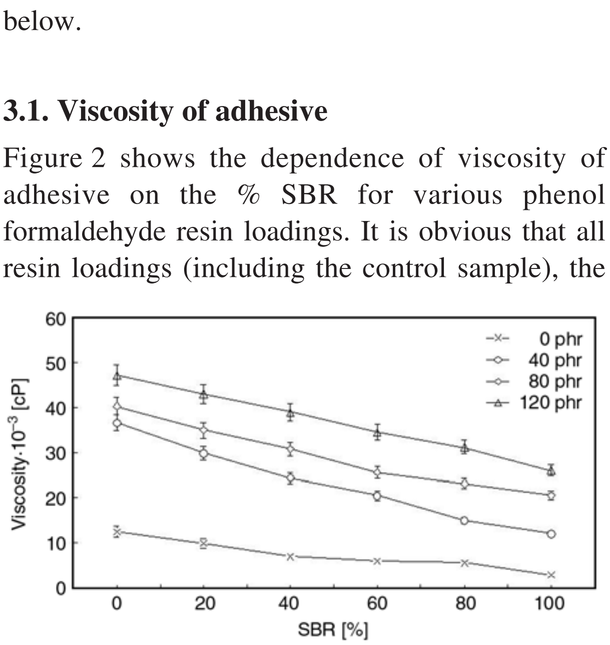

Figure 2. Dependence of viscosity with % SBR for various resin loadings

3.2. Loop tack

The dependence of loop tack on % SBR for various resin loadings is shown in Figure 3.

For all resin loadings, loop tack increases with % SBR to a maximum value at 20% SBR composition, after which it decreases with increasing % SBR. The maximum tack value observed at 20% SBR is attributed to the maximum wettability of adhesive on the substrate. At this condition, the adhesive is able to wet and conforms to the irregularities of the substrate, i.e. low surface energy condition is observed [10]. The surface energy of the

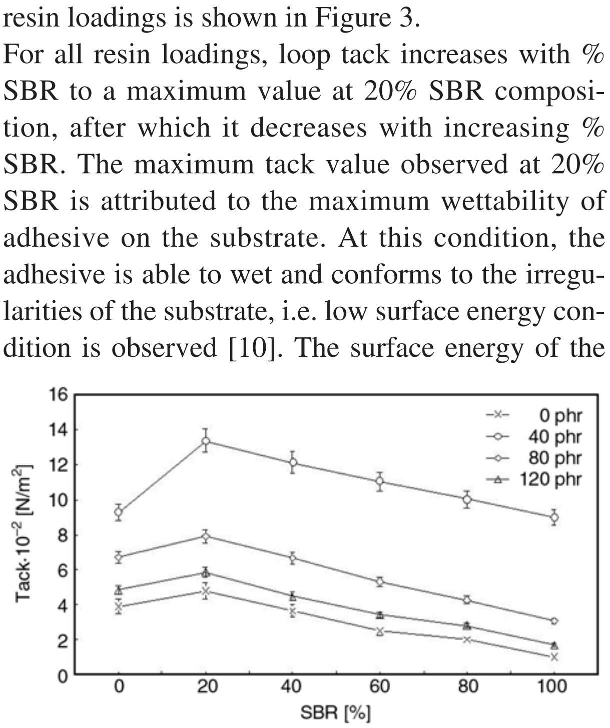

Figure 3. Dependence of loop tack with % SBR for various resin loadings

adhesive depends on the composition as shown by the variation of tack with % SBR and phenol-formaldehyde resin content. As % SBR is further increased, tack value decreases correspondingly. This observation is associated with the lower flexibility property of SBR due to its lower T_g (–53°C) [11] compared to that of SMR L (T_g = –72°C). Figure 3 also indicates that for a fixed % SBR, maximum tack is consistently exhibited by the 40 phr resin loading. At this resin loading, the optimum composition of adhesive is achieved which results in optimum wettability of adhesive. However, if resin loading is increased beyond 40 phr, a decrease in the tack value is obtained. This is due to the decreasing wettability of adhesive as resin component becomes a dominant component in the adhesive system, i. e. phase inversion occurs. The lowest tack value is shown by the control sample where no resin is added. This means that poor adhesion property is observed in the absence of tackifying resin such as phenol formaldehyde suggesting low wettability of adhesive.

3.3. Peel strength

The peel strength between paper/PET film using a T-Peel test mode is shown in Figure 4.

No plateau level is reached during crack propagation because the surface of substrate is not perfectly smooth. The irregularities on the surface of substrate (PET and release paper) explain why peaks occur during peel test. Debonding is observed between adhesive and release paper. The position of peaks changes with adhesive composition. Except for the control sample, maximum peel strength is observed at 60% SBR for the resin-loaded adhesives. Owing to the difference in the substrate systems, maximum peak position for loop tack study (Figure 3) and that of peel strength (Figure 4) occurs at different positions. This observation is attributed to the difference in compatibility between the adhesive and substrates. However, for the control sample in the absence of phenol formaldehyde resin, maximum wettability occurs at lower % SBR, i. e. at 40% SBR. In all cases, peel strength drops after the maximum value which is due to the decrease in wettability with increase in % SBR. For a fixed % SBR, it indicates that after 40 phr of phenol-formaldehyde resin content, a decrease in peel strength is obtained. This observation suggests that phase inversion occurs between 40–80 phr of the resin. The drop in peel strength with further addition of resin is attributed to the dilution effect, resulting in a decrease in modulus, i. e. resistance to rupturing of the bond is decreased. The peel strength for the 90° and 180° Peel Tests are shown in Figures 5 and 6 respectively. Except for the control sample, the figures also indicate that maximum peel strength occurs at 60% SBR for all the resin loadings studied. All these observations may be explained by the varying degree of compatibility of adhesive with substrate following changes in the adhesive formulation. Figure 7 shows the comparison of peel strength obtained from the three modes of peel tests at 60% SBR.

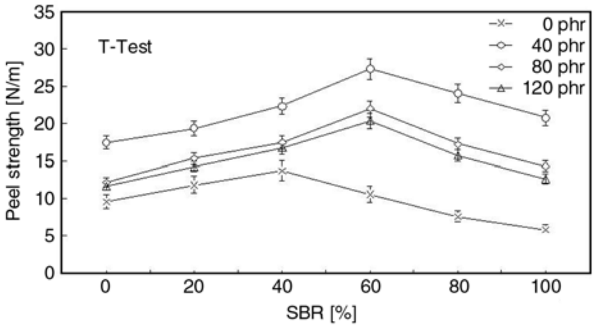

Figure 4. Dependence of peel strength (T-test) with % SBR for various resin loadings

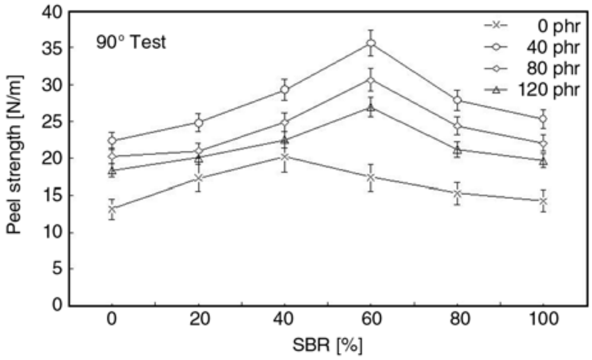

Figure 5. Dependence of peel strength (90° test) with % SBR for various resin loadings

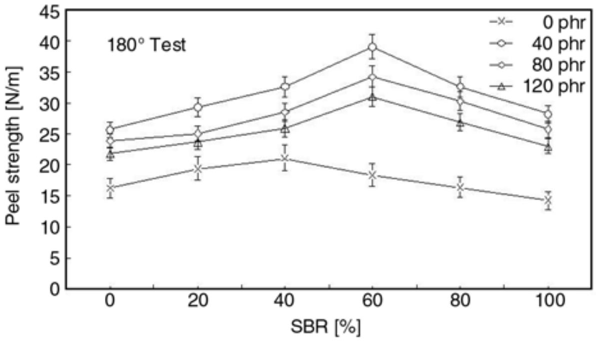

Figure 6. Dependence of peel strength (180° test) with % SBR for various resin loadings

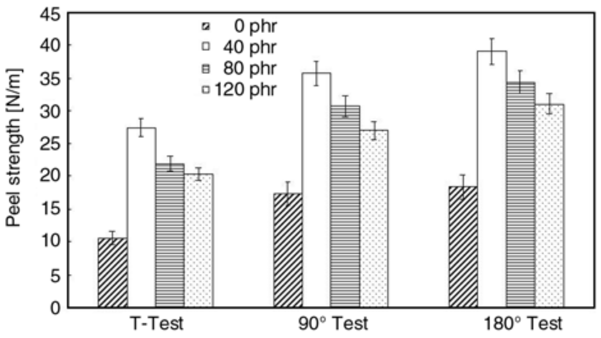

Figure 7. Comparison of peel strength between resin loadings for various peel tests at 60% SBR

The results also reveal that 180° Peel Test consistently exhibits the highest peel strength for all phenol formaldehyde loadings, including the control sample. The difference in results is attributed to the difference in the angle of testing where a higher peel force is needed in the case of 180° Peel Test. The rubber chains undergo more strain-induced crystallization [12–13] in the 180° Peel Test compared to T- and 90° Peel Tests. In other words, the adhesive hardens at high strain levels to become a tough solid and the adhesive layer itself cannot easily be ruptured [6]. Therefore, higher peel strength is needed in the case of 180° Peel Test. Figure 7 also shows that the highest peel strength is exhibited by 40 phr resin loading for the three modes of peel tests carried out in this study. Adhesive deformation in the bonding stage should be viscous to conform to the irregularities of the substrate. A high modulus during bond rupture will increase the tack and peel strength of adhesive. From this study, it is observed that the optimum viscosity occurs at 2.2×10^4 cP where maximum peel strength is observed at 60% SBR and 40 phr phenol-formaldehyde resin content. At this particular composition, maximum wettability and compatibility occur resulting in mechanical interlocking and anchorage of the adhesive in pores and irregularities in the substrate [8, 14], hence the highest peel strength is observed.

4. Conclusions

From this study, the following conclusions can be drawn.

1. The viscosity of adhesive decreases gradually with increase in SBR composition, an observation which is attributed by lower molecular weight of SBR compared to that of SMR L. Below 60% SBR composition, significant increase in viscosity from 0–40 phr of phenol formaldehyde resin loading occurs, an observation which is associated to the onset of chain entanglement between SMR L and phenol formaldehyde resin.
2. Loop tack increases with % SBR up to a maximum value at 20% SBR composition, after which it decreases with increasing % SBR. The maximum tack value observed at 20% SBR is ascribed to the maximum wettability of adhesive on the substrate. For a fixed % SBR, maximum tack is observed at 40 phr resin loading after which tack value drops with further resin loading due to phase inversion.
3. Except for the control sample, maximum peel strength is observed at 60% SBR and 40 phr of phenol formaldehyde resin loading for all the three modes of peel tests carried out in this study indicating that maximum wettability and compatibility occur at this composition. The highest peel strength is shown by the 180° Peel Test for all phenol formaldehyde loadings, including the control sample. This observation is attributed to the higher strain-induced crystallization of rubber chain during 180° peel test, hence causing the adhesive to harden and become a tough solid which cannot be ruptured easily.

Acknowledgements

The authors acknowledge the short-term research grant provided by Universiti Sains Malaysia that has resulted in this article.

References

[1] Poh B. T., Chang Y. Y.: Viscosity and peel strength of SMR 10-based pressure-sensitive adhesives. Polymer-Plastics Technology and Engineering, **45**, 1251–1256 (2006).

[2] Poh B. T., Chee C. L.: Effect of coumarone-indene resin on adhesion property of SMR 20-based pressure-sensitive adhesives. International Journal of Polymeric Materials, **56**, 247–255 (2007).

[3] Poh B. T., Kwo H. K.: Peel and shear strength of pressure-sensitive adhesives prepared from epoxidized natural rubber. Journal of Applied Polymer Science, **105**, 680–684 (2007).

[4] Poh B. T., Chow S. K.: Effect of zinc oxide on the viscosity, tack and peel strength of ENR 25-based pressure-sensitive adhesives. Journal of Applied Polymer Science, **106**, 333–337 (2007).

[5] Poh B. T., Kwo H. K.: Shear strength of SMR-based pressure-sensitive adhesives. Polymer-Plastics Technology and Engineering, in press (2007).

[6] Skeist I. E.: Handbook of Adhesives. Van Nostrand Reinhold, New York (1990).

[7] Sadequl A. M., Poh B. T., Ishiaku U. S.: Effect of filler loading on the mechanical properties of epoxidized natural rubber (ENR 25) compared with natural rubber (SMR L). International Journal of Polymeric Materials, **43**, 261–278 (1999).

[8] Gierenz G., Karmann W.: Adhesives and Adhesive Tapes. Wiley-VCH, New York (2001).

[9] Poh B. T., Ong B. T.: Dependence of viscosity of polystyrene solutions on molecular weight and concentration. European Polymer Journal, **20**, 975–978 (1984).

[10] Satas D.: Handbook of pressure-sensitive adhesive technology. Van Nostrand Reinhold, New York (1982).

[11] Barlow F. W.: Rubber Compounding: Principles, materials, and techniques. Marcel Dekker, New York (1988).

[12] Poh B. T., Ismail H., Quah E. H.: Fatigue, resilience and hardness properties of unfilled SMR L/ENR 25 and SMR L/SBR blends. Polymer Testing, **20**, 389–394 (2001).

[13] Poh B. T., Ismail H., Quah E. H., Chin P. L.: Cure and mechanical properties of filled SMR L/ENR 25 and SMR L/SBR blends. Journal of Applied Polymer Science, **81**, 47–52 (2001).

[14] Lee L. H.: Adhesive bonding. Plenum Press, New York (1991).

eXPRESS Polymer Letters Vol.1, No.10 (2007) 660–666
Available online at www.expresspolymlett.com
DOI: 10.3144/expresspolymlett.2007.90

Detachment of human endothelial cell sheets from thermo-responsive poly(NiPAAm-co-DEGMA) carriers

M. Nitschke[1*], T. Götze[1], S. Gramm[1,3], C. Werner[1,2]

[1]Leibniz Institute of Polymer Research Dresden, Max Bergmann Center of Biomaterials, Hohe Str. 6, 01069 Dresden, Germany
[2]Institute of Biomaterials and Biomedical Engineering, University of Toronto, 5 King's College Road, Toronto, M5S 3G8 Canada
[3]present address: Oxyphen GmbH, Bautzner Landstrasse 45, 01454 Großerkmannsdorf, Germany

Received 31 May 2007; accepted in revised form 8 August 2007

Abstract. The technique of gently harvesting cells and cell sheets using stimuli-responsive cell culture carriers was applied to human umbilical vein cord endothelial cells (HUVEC). To meet the particular requirements of this demanding cell type, a copolymer consisting of *N*-isopropylacrylamide and diethyleneglycol methacrylate (poly(NiPAAm-co-DEGMA)) was combined with a fine-tuned protein pre-coating. Using this approach the detachment of HUVEC sheets was studied. Furthermore, the behavior of the extracellular matrix upon cell detachment was followed by protein staining. The results demonstrate the feasibility of harvesting HUVEC sheets from stimuli-responsive polymer layers and provide valuable options for the advanced engineering of vascular structures.

Keywords: *smart polymers, polymer gels, poly(N-isopropylacrylamide), tissue engineering*

---

1. Introduction

Polymers with a thermally stimulated volume phase transition like poly(*N*-isopropylacrylamide) (PNiPAAm) [1] and NiPAAm containing copolymers can be prepared on solid surfaces by various techniques [2–6]. The resulting coatings respond with swelling and collapsing to small changes in the environmental temperature and can be used as cell culture carriers for harvesting cells and cell sheets without enzymatic or mechanical treatments [7–10].

Vascular endothelial cells receive a lot of attention in tissue engineering strategies as they mediate the interaction of flowing blood with other tissues [11]. Control of endothelial cell adhesion and growth is therefore considered crucial for safety and performance of implants in the cardiovascular system such as vascular grafts or stents. However, endothelialization *in vivo* often fails and pre-seeding of implants *in vitro* is applied according to various schemes [12, 13]. However, even the time-consuming procedure of growing endothelial cell linings directly on the implant is limited because of the lack of the characteristic functional structure of natural vasculature combining layers of smooth muscle cells and endothelial cells [14–17]. To this end, the preparation and subsequent alignment of cell sheets may provide interesting options: Pre-fabricated endothelial cell layers may be deposited on top of smooth muscle cell linings on – degradable or nondegadable – biomaterials and, by that, form a functional structure closely resembling vascular tissue. A defined procedure for the harvesting of endothelial cell sheets is an essential requirement for the implementation of this strategy.

---

*Corresponding author, e-mail: nitschke@ipfdd.de

In the literature there are several reports on cultivation and detachment of endothelial cells from thermo-responsive carriers [18–21]. Copolymerization of NiPAAm with a hydrophobic comonomer (*n*-butyl methacrylate) [19] was shown to be an effective approach for adjusting the substrate properties. The main objective of the work presented here is another route to adapt the technique of thermo-responsive cell culture carriers to the particular requirements of human endothelial cells. Towards this goal, the physico-chemical properties were adjusted by combining a hydrophilic ethylene glycol containing comonomer with a fine-tuned pre-coating of fibronectin.

Cell culture carriers based on a statistical copolymer consisting of *N*-isopropylacrylamide and diethyleneglycol methacrylate (poly(NiPAAm-co-DEGMA)) [22] were prepared by plasma immobilization [23–26]. This technique allows to immobilize polymer films with a thickness of a few nanometers onto polymeric substrates like Teflon AF [27] by low pressure plasma treatment. At appropriate parameters covalent fixation is achieved while important properties like the thermoresponsive swelling and collapsing of polymer chains are preserved.

Ethylene glycol containing comonomers increase the phase transition temperature compared to the NiPAAm homopolymer [28]. Though this effect is rather small for poly(NiPAAm-co-DEGMA), the hydrophilic character of the diethylene glycol group improves cell detachment [10] and allows a more gentle handling of cell sheets upon harvest.

2. Experimental

2.1. Materials

Teflon AF1600™ solution (6% wt/wt) [27] was purchased from DuPont. Teflon AF is an amorphous copolymer based on 2,2 bistrifluoromethyl-4,5-difluoro-1,3-dioxole and tetrafluoroethylene. FC75, a fluorocarbon solvent for Teflon AF, was obtained from 3M.

Poly(NiPAAm-co-DEGMA) (M_n 40 000 g·mol^{-1}, M_w 130 000 g·mol^{-1}, polydispersity ~3 by GPC), was synthesized by free radical polymerization. The ratio of the comonomers in the copolymer is 99.2:0.8 (NiPAAm:DEGMA) [22] (Figure 1).

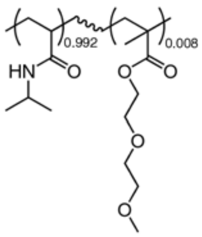

Figure 1. Structure of poly(NiPAAm-co-DEGMA)

For fibronectin (FN) immunostaining primary antibody anti FN rabbit (US Biological, Swampscott, Massachusetts) and secondary antibodies anti FN rabbit (Jackson Immuno Research Laboratories, West Grove, PA) were used.

2.2. Teflon AF substrate preparation and hydrogel coating

Thin films of Teflon AF were prepared by spin coating on microscopy cover slips (24×24 mm^2) and on silicon wafers (15×20 mm^2, oxide thickness 30 nm, for ellipsometry). For that purpose, the Teflon AF solution as received was further diluted using FC75 to obtain a 1% wt/wt solution. After spin coating (maximum speed 3000 rpm, acceleration 3000 rpm·s^{-1}, 30 s), the Teflon AF films with a thickness of about 50 nm were annealed for 10 minutes at 110°C. Subsequently, poly(NiPAAm-co-DEGMA) was prepared on Teflon AF substrates by spin coating (maximum speed 5000 rpm, acceleration 5000 rpm·s^{-1}, 30 s) from a 0.25% wt/wt solution in chloroform (99.8%, Fluka). Teflon AF surfaces were pre-treated in argon plasma as described below for 120 s to obtain an appropriate wetting behavior.

2.3. Plasma immobilization

Poly(NiPAAm-co-DEGMA) thin films were immobilized using low pressure argon plasma. The plasma treatment was carried out in a computer controlled MicroSys apparatus by Roth & Rau (Wüstenbrand, Germany). The cylindrical vacuum chamber, made of stainless steel, has a diameter of 350 mm and a height of 350 mm. The base pressure obtained with a turbomolecular pump was <10^{-7} mbar. On the top of the chamber a 2.46 GHz electron cyclotron resonance (ECR) plasma source RR160 by Roth & Rau with a diameter of 160 mm and a maximum power of 800 W was mounted. Argon (99.999%, Messer Griesheim) was introduced into the active volume of the plasma source via a gas flow control system. When the plasma source was on, the pressure was measured by a capacitive vacuum gauge. The samples were introduced by a load-lock-system and placed on a grounded aluminum holder near the center of the chamber. The distance between the sample and the excitation volume of the plasma source was about 200 mm. For the experiments of this work the following parameters were used: effective power 120 W, argon gas flow 38 sccm, pressure $8\cdot10^{-3}$ mbar, treatment time 10 s. After plasma treatment, the samples were rinsed in chloroform (99.8%, Fluka) for 1 h at room temperature and dried under vacuum.

To fabricate thermo-responsive cell culture carriers with lateral microstructures, the masking technique described in detail in [29] was used. Briefly, argon plasma treatment of a spin-coated poly(NiPAAm-co-DEGMA) film was performed as described above with the sample covered by a transmission electron microscopy grid. The grid protected the copolymer layer underneath from plasma exposure which left this part soluble while the exposed part of the film was bonded to the Teflon AF surface. By rinsing with chloroform, the copolymer could be removed completely from the covered part leaving behind a microstructure.

2.4. Spectrosopic ellipsometry

Ellipsometric measurements were performed using a variable angle multiwavelength ellipsometer M-2000VI (J. A. Woollam Co., Inc.). It is a Diode Array Rotating Compensator Ellipsometer (DARCE™) in polarizer-compensator-sample-analyzer configuration equipped with an automatic computer-controlled goniometer and a horizontally mounted sample stage. The light source is a 50 W mercury lamp. For a given angle of incidence, the M-2000VI measures 500 wavelengths simultaneously covering the spectral range from 370–1700 nm. Accurate measurements over the full Δ and Ψ range were acquired ($\Delta =$ 0°–360°; $\Psi =$ 0°–90°).

In case of dry samples, values from three angles of incidence, 65°, 70° and 75° were acquired. To investigate swollen hydrogel layers, a solid-liquid cell (angle of incidence 68°) with de-ionized water (pH 6.5) was used. For the variation of temperature with a rate of 1 $K\cdot min^{-1}$, a computer controlled heating device for the solid-liquid cell was used.

To calculate the thickness and the optical properties of the polymer films under investigation, fit procedures based on optical multi-layer models were applied to the the ellipsometric data.

2.5. Cell cultivation

L929 mouse fibroblasts were obtained from DSMZ, Braunschweig, Germany and cultivated at 37°C, 5% CO_2 and 95% relative air moisture using RPMI medium (RPMI 1640; Pan Biotech GmbH, Aidenbach, Germany) containing 10% fetal calf serum (FCS) and antibiotics.

Human endothelial cells from umbilical cord vein were collected according to the procedure suggested by Weis *et al.* [30]. Cells were grown at 37°C, 5% CO_2 and 95% relative air moisture on T25 culture dishes pre-coated with fibronectin (20 $\mu g\cdot ml^{-1}$ in phosphate buffered saline, PBS, 30 min at 37°C) using endothelial cell growth medium (Promocell, Heidelberg, Germany) containing 2% FCS with supplement mix.

L929 mouse fibroblasts and HUVEC were harvested by trypsination and applied to the poly(NiPAAm-co-DEGMA) substrates. The substrates were allowed to swell for 24 hours at room temperature in PBS and subsequently conditioned at 37°C. In case of HUVEC a pre-coating with fibronectin (5 $\mu g\cdot ml^{-1}$ in PBS; 30 min at 37°C) was applied. Subsequently, the solution was exchanged with the tempered cell culture medium. After a period of 30 minutes cells were seeded with a density of $1.5\cdot10^5$ cells per cm^2 while keeping the temperature at 37°C. The cultivation was proceeded until confluence was reached.

2.6. Imaging techniques

Microscopy images were obtained with an Axiovert 200 microscope by Zeiss. The microscope was equipped with a special incubator that allows cell cultivation (37°C, air stream supplemented with 5% CO_2) and temperature variation while images are taken with a digital camera (AxioCam Colour). Axio Vision 3.1 software was used for image processing.

Fluorescence micrcroscopy images were obtained with an inverse fluorescence microscope Leica DMIRE2 equipped with a 40× oil immersion objective. Improvision 4.03 software was used for image processing.

For immunostaining cells were fixed with 4% paraformaldehyde (Fluka) in PBS for 10 min and subsequently permeabilized with 0.5% Triton® X-100 (Fluka) in PBS for 10 min. Samples were stained with the primary and secondary antibodies (dilution 1:100 and 1:50 in PBS, retention time 45 min and 30 min respectively). After every step the samples were rinsed twice in PBS.

3. Results and discussion

3.1. Characterization of the thermo-responsive cell culture carriers

To study the multilayer polymer system, the optical properties of Teflon AF and poly(NiPAAm-co-DEGMA) were determined. For that purpose thin films on silicon wafers were investigated by spectroscopic ellipsometry. Data sets were evaluated using a fit procedure based on an optical model consisting of the bulk silicon, the silicon oxide layer, and the respective polymer layer. Both polymers were found to be transparent, i. e., no absorption occurs in the wavelength range investigated ($k = 0$). The wavelength dependence of the refractive index was fitted using a two-parameter Cauchy equation (1):

$$n(\lambda) = A_n + \frac{B_n}{\lambda^2} \tag{1}$$

where n: refractive index, λ: wavelength, A_n, B_n: Cauchy parameters [31]. The best fit of ellipsometric data provided $A_n = 1.32$ and $B_n \leq 0.002$ for Teflon AF and $A_n = 1.46$ and $B_n \leq 0.005$ for dry poly (NiPAAm-co-DEGMA) [10].

In the next step poly(NiPAAm-co-DEGMA) thin films covalently fixed by plasma immobilization on Teflon AF coated silicon substrates were immersed in distilled water at room temperature overnight and heated above the phase transition temperature. Subsequently, the temperature was decreased and increased repeatedly while the thickness and the effective refractive index of the swelling and collapsing hydrogel layer were monitored by spectroscopic ellipsometry. Above the phase transition temperature, constant values slightly higher than the dry film thickness were observed while an almost linear increase was found towards lower temperature values (Figure 2). The reversible switching has a amplitude of approximately 40 nm corresponding to a swelling ratio of about 3 with respect to the collapsed state of the poly(NiPAAm-co-DEGMA) film. For the heating/cooling rate of 1 K·min^{-1} there is no significant hysteresis effect.

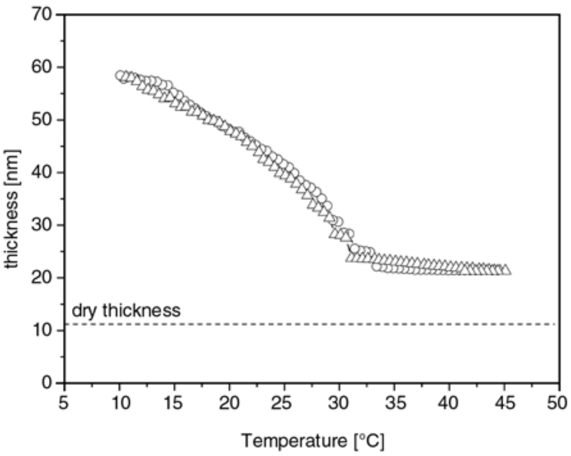

Figure 2. Reversible temperature dependent swelling behavior of poly(NiPAAm-co-DEGMA) thin films in water (circles cooling, triangles heating)

3.2. Cell detachment experiments

Experiments with L929 mouse fibroblasts, a simple and well-known cell line, were carried out on poly(NiPAAm-co-DEGMA) to ensure the comparability with previous studies on different thermo-responsive materials [9, 10]. At 37°C cells adhere, spread, proliferate and reach confluence after 48 h (Figure 3 left) as observed on standard T25 cell culture dishes.

After temperature decrease to 23°C cells detach within a few minutes as a single sheet without enzymatic or mechanical treatment. In Figure 3 (right) the L929 layer retracts from the upper right to the lower left corner with no cells leaving behind on the thermo-responsive surface.

In the next step HUVECs were investigated. After seeding the cells and standard cultivation at 37°C for 48 h only single cells or small aggregates adhered to the copolymer surface. Cells did not show their characteristic morphology and did not form a confluent layer. To ensure initial cell adhesion and spreading, the collapsed thermo-responsive substrates were exposed to a fibronectin solution at 37°C for 30 min. The concentration was varied from 3 µg·ml^{-1} to 20 µg·ml^{-1}. An appropriate balance between initial cell adhesion and subsequent temperature driven cell detachment was found for a fibronectin concentration of 5 µg·ml^{-1}.

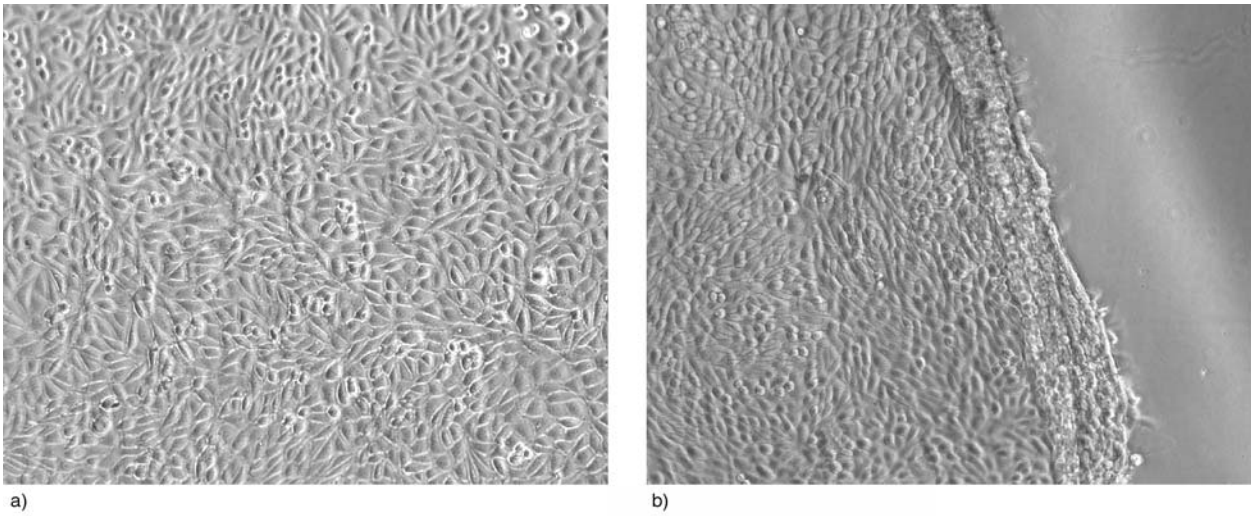

Figure 3. L929 mouse fibroblast detachment from a poly(NiPAAm-co-DEGMA) substrate: Microscopy images ($873\times691\ \mu m^2$) after standard cultivation at 37°C (left) and after temperature decrease (right)

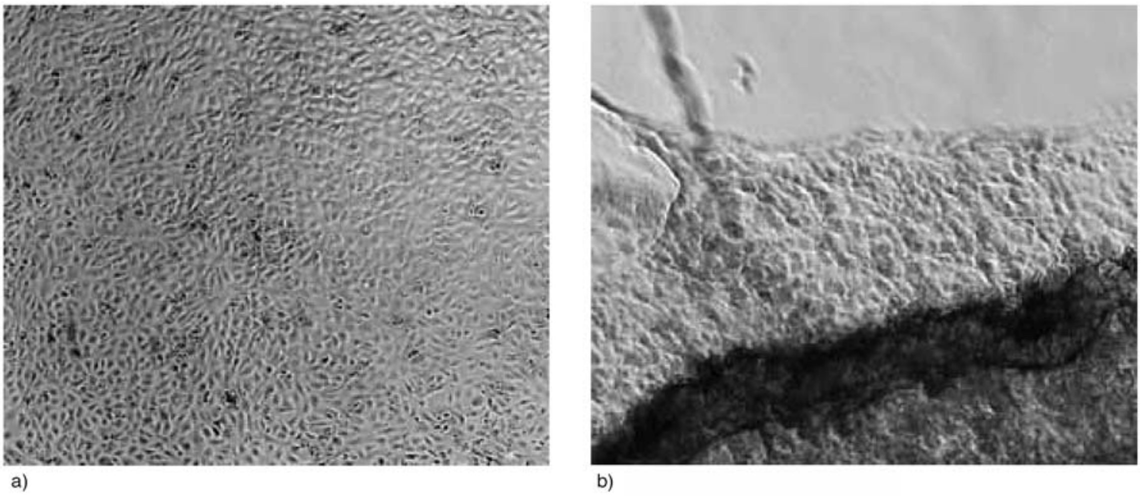

Figure 4. HUVEC detachment from a poly(NiPAAm-co-DEGMA) substrate: Microscopy images ($512\times441\ \mu m^2$) after standard cultivation at 37°C (left) and after temperature decrease (right)

Figure 4 shows a typical HUVEC detachment experiment on a pre-coated poly(NiPAAm-co-DEGMA) substrate. For standard cultivation at 37°C on the FN exposed thermo-responsive carrier cells reach confluence after 20 h and show their characteristic cobblestone-like morphology (left). After temperature decrease to 23°C cells detach within a few hours as a single sheet (right). As in the case of L929 no cells are left behind on the swollen thermo-responsive substrate.

3.3. Protein staining experiments

Unraveling the fate of proteins of the extracellular matrix (ECM) on a thermo-responsive cell culture carrier during cell harvesting is a key to understand the mechanism of cell detachment [32]. Accordingly, the allocation of fibronectin as a major component of the ECM was investigated by immunofluorescence. For that purpose a substrate with lateral structures in the order of several 100 μm (i. e. well above the dimension of a single cell) of poly(NiPAAm-co-DEGMA) was employed [29]. This allows a direct comparison of the cell behaviour on adhesive uncoated areas with thermo-responsive areas in the same image (Figure 5). A HUVEC layer grown at standard cultivation at 37°C (left) was cooled down below the phase transition temperature. Cells adhering on poly (NiPAAm-co-DEGMA) coated areas detached as described above (center). Subsequently, the lateral distribution of fibronectin was visualized by immunostaining (right). While in the adhesive areas cells and ECM are clearly visible, no fibronectin

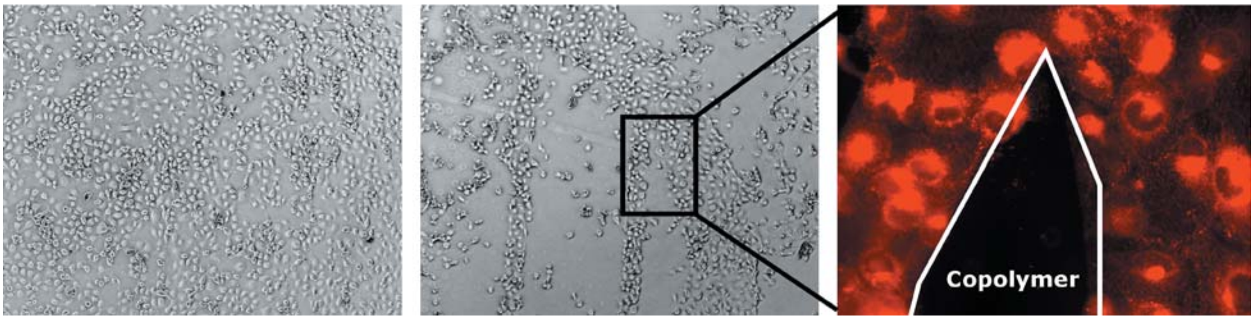

Figure 5. HUVEC detachment from a structured poly(NiPAAm-co-DEGMA) substrate: Microscopy images (1747×1385 μm^2) after standard cultivation at 37°C (left) and after temperature decrease (center). Fluorescence microscopy image (672×512 μm^2, fibronectin, Cy5) of the indicated region.

appears in areas that had been occupied by cells before. This agrees well with results from other studies [20, 21, 33] showing that hardly any ECM remained on the surface of thermo-responsive cell culture carriers after cell detachment. This is an indication, that the ECM is removed together with endothelial cells providing coherence of the harvested cell sheets.

4. Conclusions

The technique of harvesting cells and cell sheets without enzymatic treatments using thermo-responsive cell culture carriers was applied to human endothelial cells. To meet the requirements of this cell type the physico-chemical properties of the thermo-responsive carriers were adjusted. Poly (NiPAAm-co-DEGMA), a polyethylene glycol containing hydrogel, was identified to provide an appropriate switching behaviour. The repeated swelling and collapsing of the material was characterized quantitatively by spectroscopic ellipsometry. A fine-tuned fibronectin pre-coating of the collapsed hydrogel surface ensures the initial adhesion and spreading of HUVEC. After reaching confluence, HUVEC sheets were detached successfully by decreasing the temperature to 23°C. Immunostaining experiments prove the detachment of the extracellular matrix together with the cell sheet.

The reported results demonstrate the applicability of temperature-driven cell sheet harvesting to human endothelial cells grown in culture. As this cell type is of highest interest in the engineering of vascular structures future activities may utilize this approach for the design of advanced multilayered graft substitutes consisting of degradable biomaterials, smooth muscle cells and endothelial cells.

Acknowledgements

The authors thank R. Schulze and K. J. Eichhorn (Leibniz Institute of Polymer Research Dresden) for ellipsometry measurements and discussions.

References

[1] Schild H. G.: Poly (N-isopropylacrylamide)– experiment, theory and application. Progress in Polymer Science, **17**, 163–249 (1992).

[2] Kwon O. H., Kikuchi A., Yamato M., Okano T.: Accelerated cell sheet recovery by co-grafting of PEG with PIPAAm onto porous cell culture membranes. Biomaterials, **24**, 1223–1232 (2003).

[3] Cheng X. H., Canavan H. E., Stein M. J., Hull J. R., Kweskin S. J., Wagner M. S., Somorjai G. A., Castner D. G., Ratner B. D.: Surface chemical and mechanical properties of plasma-polymerized N-isopropylacrylamide. Langmuir, **21**, 7833–7841 (2005).

[4] Curti P. S., de Moura M. R., Veiga W., Radovanovic E., Rubira A. F., Muniz E. C.: Characterization of PNIPAAm photografted on PET and PS surfaces. Applied Surface Science, **245**, 223–233 (2005).

[5] Huang J., Wang X. L., Chen X. Z., Yu X. H.: Temperature-sensitive membranes prepared by the plasma-induced graft polymerization of N-isopropylacrylamide into porous polyethylene membranes. Journal of Applied Polymer Science, **89**, 3180–3187 (2003).

[6] Lin Z., Xu T. W., Zhang L.: Radiation-induced grafting of N-isopropylacrylamide onto the brominated poly(2,6-dimethyl-1,4-phenylene oxide) membranes. Radiation Physics and Chemistry, **75**, 532–540 (2006).

[7] Yamato M., Okano T.: Cell sheet engineering. Materials Today, **7**, 42–47 (2004).

[8] Yang J., Yamato M., Kohno C., Nishimoto A., Sekine H., Fukai F., Okano T.: Cell sheet engineering: Recreating tissues without biodegradable scaffolds. Biomaterials, **26**, 6415–6422 (2005).

[9] Schmaljohann D., Oswald J., Jorgensen B., Nitschke M., Beyerlein D., Werner C.: Thermo-responsive PNiPAAm-g-PEG films for controlled cell detachment. Biomacromolecules, **4**, 1733–1739 (2003).

[10] Nitschke M., Gramm S., Götze T., Valtink M., Drichel J., Voit B., Engelmann K., Werner C.: Thermo-responsive poly(NiPAAm-co-DEGMA) substrates for gentle harvest of human corneal endothelial cell sheets. Journal of Biomedical Materials Research A, **80**, 1003–1010 (2007).

[11] Werner C., Maitz M., Sperling C.: Current strategies towards hemocompatible coatings. Journal of Materials Chemistry, **17**, 3376–3384 (2007).

[12] Nerem R. M.: Tissue engineering of the vascular system. Vox Sanguinis, **87**, 158–160 (2004).

[13] Gong Z. D., Niklason L. E.: Blood vessels engineered from human cells. Trends in Cardiovascular Medicine, **16**, 153–156 (2006).

[14] Berglund J. D., Galis Z. S.: Designer blood vessels and therapeutic revascularization. British Journal of Pharmacology, **140**, 627–636 (2003).

[15] Bhattacharya V., Cleanthis M., Stansby G.: Preventing vascular graft failure: Endothelial cell seeding and tissue engineering. Vascular Disease Prevention, **2**, 21–27 (2005).

[16] Nerem R. M., Seliktar D.: Vascular tissue engineering. Annual Review of Biomedical Engineering, **3**, 225–243 (2001).

[17] Stegemann J. P., Hong H., Nerem R. M.: Mechanical, biochemical, and extracellular matrix effects on vascular smooth muscle cell phenotype. Journal of Applied Physiology, **98**, 2321–2327 (2005).

[18] Kushida A., Yamato M., Konno C., Kikuchi A., Sakurai Y., Okano T.: Decrease in culture temperature releases monolayer endothelial cell sheets together with deposited fibronectin matrix from temperature-responsive culture surfaces. Journal of Biomedical Materials Research, **45**, 355–362 (1999).

[19] Tsuda Y., Kikuchi A., Yamato M., Sakurai Y., Umezu M., Okano T.: Control of cell adhesion and detachment using temperature and thermoresponsive copolymer grafted culture surfaces. Journal of Biomedical Materials Research, Part A, **69**, 70–78 (2004).

[20] Canavan H. E., Cheng X. H., Graham D. J., Ratner B. D., Castner D. G.: Cell sheet detachment affects the extracellular matrix: A surface science study comparing thermal liftoff, enzymatic, and mechanical methods. Journal of Biomedical Materials Research, Part A, **75**, 1–13 (2005).

[21] Canavan H. E., Cheng X. H., Graham D. J., Ratner B. D., Castner D. G.: Surface characterization of the extracellular matrix remaining after cell detachment from a thermoresponsive polymer. Langmuir, **21**, 1949–1955 (2005).

[22] Gramm S., Komber H., Schmaljohann D.: Copolymerization kinetics of N-isopropylacrylamide and diethylene glycol monomethylether monomethacrylate determined by online NMR spectroscopy. Journal of Polymer Science, Part A: Polymer Chemistry, **43**, 142–148 (2005).

[23] Nitschke M., Zschoche S., Baier A., Simon F., Werner C.: Low pressure plasma immobilization of thin hydrogel films on polymer surfaces. Surface and Coatings Technology, **185**, 120–125 (2004).

[24] Nitschke M., König U., Lappan U., Minko S., Simon F., Zschoche S., Werner C.: Low pressure plasma-based approaches to fluorocarbon polymer surface modification. Journal of Applied Polymer Science, **103**, 100–109 (2007).

[25] Sheu M. S., Hoffman A. S., Feijen J.: A glow-discharge treatment to immobilize poly(ethylene oxide) poly(propylene oxide) surfactants for wettable and nonfouling biomaterials. Journal of Adhesion Science and Technology, **6**, 995–1009 (1992).

[26] Terlingen J. G. A., Feijen J., Hoffman A. S.: Immobilization of surface-active compounds on polymer supports using a gas-discharge process. Journal of Biomaterials Science: Polymer Edition, **4**, 31–33 (1992).

[27] Korinek P. M.: Amorphous fluoropolymers- a new-generation of products. Macromolecular Symposia, **82**, 61–65 (1994).

[28] Schmaljohann D., Beyerlein D., Nitschke M., Werner C.: Thermo-reversible swelling of thin hydrogel films immobilized by low-pressure plasma. Langmuir, **20**, 10 107–10 114 (2004).

[29] Schmaljohann D., Nitschke M., Schulze R., Eing A., Werner C., Eichhorn K. J.: In situ study of the thermoresponsive behavior of micropatterned hydrogel films by imaging ellipsometry. Langmuir, **21**, 2317–2322 (2005).

[30] Weis J. R., Sun B., Rodgers G. M.: Improved method of human umbilical arterial endothelial cell culture. Thrombosis Research, **61**, 171–173 (1991).

[31] Fattorini H. O., Kerber A.: The Cauchy problem; Encyclopedia of mathematics and its applications. Cambridge University Press, Cambridge (1984).

[32] Cheng X., Canavan H. E., Graham D. J., Castner D. G., Ratner B. D.: Temperature dependent activity and structure of adsorbed proteins on plasma polymerized N-isopropyl acrylamide. Biointerphases, **1**, 61–72 (2006).

[33] Yamato M., Konno C., Kushida A., Hirose M., Utsumi M., Kikuchi A., Okano T.: Release of adsorbed fibronectin from temperature-responsive culture surfaces requires cellular activity. Biomaterials, **21**, 981–986 (2000).

eXPRESS Polymer Letters Vol.1, No.10 (2007) 667–672
Available online at www.expresspolymlett.com
DOI: 10.3144/expresspolymlett.2007.91

Flexural strength and tribological properties of rare earth treated short carbon fiber/polyimide composites

X. R. Zhang[1,2], *P. Zhao*[1], *X. Q. Pei*[1], *Q. H. Wang*[1*], *Q. Jia*[1]

[1]State Key Laboratory of Solid Lubrication, Lanzhou Institute of Chemical Physics, Chinese Academy of Sciences, Lanzhou 730000, China
[2]Graduate School, Chinese Academy of Sciences, Beijing 100039, China

Received 21 June 2007; accepted in revised form 8 August 2007

Abstract. To investigate the influence of carbon fiber (CF) surface treatment on the flexural strength and tribological properties of the short-cut CF/polyimide (PI) composites, pitch-based short-cut CF were treated by rare earth. The CF before and after treatment was examined by X-ray photoelectron spectroscopy (XPS) and by scanning electron microscopy (SEM). The flexural strength of the specimens was determined in a three-point test machine. The friction and wear behaviors of PI composites sliding against GCr15 steel rings were evaluated on an M-2000 model ring-on-block test rig. The results show that the surface of the treated CF became rougher and there formed lots of active groups after rare earth treatment. The flexural strength of PI composites with rare earth treated CF was improved. The friction coefficient and wear rate of PI composites with rare earth treated CF were lower than that with untreated CF.

Keywords: *polymer composites, carbon fiber, surface treatment, flexural strength, tribological property*

1. Introduction

PI possesses some extraordinary characteristics, such as excellent mechanical and electrical (insulating) properties, good thermal stability and chemical inertness, high wear resistance, and resistance against high energy radiation [1, 2]. Yet, it can not be widely used as self-lubricant material because of its high friction coefficient. Therefore, various fillers have been tried to modify PI composites. CF are widely used as fillers in advanced composite materials due to their high strength and high modulus, excellent electrical and thermal conductivity, good friction and wear qualities and high resistance to fatigue and creep [3, 4]. The CF filled PI composites have especial application in aerospace, robots, sports goods. By reinforcing PI with CF of high strength and modulus, it might be feasible to develop high performance PI-based composites.

The properties of fiber and matrix make a critical contribution to the quality of a fiber-reinforced composite. In addition, the physical-chemical interaction between the fiber-matrix interface plays an important role in improving the mechanical properties of the fiber reinforced composite [4]. CF are chemically inert and they often produce composites with low interfacial bonding between fibers and matrix when used without any surface treatment, which accordingly affects most of the other mechanical properties of the composites [5]. Numerous methods concerning surface treatment, such as chemical method [6–8], electrochemical method [9–12], plasma treatment [13], etc., have been developed to modify the fiber surface and thus enhance the ability to establish strong interactions between fibers and matrix. Rare earth treatment is relatively novel and interesting method, which have attracted more and more researchers' interest.

---

[*]Corresponding author, e-mail: wangqh@lzb.ac.cn

Our previous work found the optimum content of CF in PI composite was 15 wt% [14]. In this work, rare earth treatment was applied to modify the CF surface, and its effect on the flexural strength and tribological properties of PI composites was evaluated.

2. Experimental

2.1. Materials and preparation of PI composites

PI (YS-20) powders (<38 µm) were commercially obtained from Shanghai Synthetic Resin Institute (Shanghai, China). The short-cut carbon fiber was about 1.5 mm in length and 7.8 µm in diameter, and the density was about 1.8 g/cm^3. The commercial short-cut carbon fibers were dipped in acetone for 24 h, then cleaned ultrasonically with acetone for 0.5 h. Finally, they were dried at 100°C for 5 hours before used.

As for the rare earth treatment, carbon fibers were soaked in an alcoholic solution of $LaCl_3$ for 5 h. the $LaCl_3$ content in the alcoholic solution was 0.3 wt%. The content of CF in PI composite was 15 wt%, the untreated and rare earth treated CF were mixed with PI powders to prepare mixtures for the preparation of PI composites. The temperature program of moulding is shown in Figure 1. At the end of each run of compression sintering, the resulting specimens were cooled with the stove in air, cut into pre-set sizes for flexural strength and tribological properties tests.

In order to investigate the possible change of chemical composition of CF treated by rare earth, XPS was used to detect functionalities on activated carbon fibers surfaces. The XPS measurement was performed using VG Scientific ESCA LAB 210 spectrometer, the base pressure in the sample chamber was about 10^{-7} Pa. The morphologies of the treated and untreated CF were compared by SEM observation, before which the tested CF specimens were plated with gold coating to render them electrically conductive.

2.2. Flexual strength test

The flexural strength of the specimens was determined in a three-point test machine (DY35 Universal material tester, France) with a span of 40 mm and crosshead speed of 1 mm/min. The specimens were 65 mm × 7 mm × 3 mm and the test surface was 65 mm × 7 mm. Three specimens of each PI composites were measured and an average value was reported. The specific flexural strength (σ_f) of the specimen was calculated from Equation (1):

$$\sigma_f = \frac{3P\cdot l}{2b\cdot h^2} \qquad \text{[MPa]} \qquad (1)$$

where P is the maximum load [N], l is the span length [mm], b is the width of the specimen [mm], h is the thickness of the specimen [mm].

2.3. Tribological properties test

The friction and wear behaviors of PI composites sliding against stainless steel were evaluated on an M-2000 model ring-on-block test rig (made by Jinan Testing Machine Factory, China).The contact schematic diagram is shown in Figure 2, the blocks in a size of 30 mm × 7 mm × 6 mm were made of the PI composites, the rings of ø40 mm × 16 mm were made of GCr15 stainless steel, the chemical composition of the GCr15 bearing steel (mass fraction, %) is shown in Table 1. The tests were carried

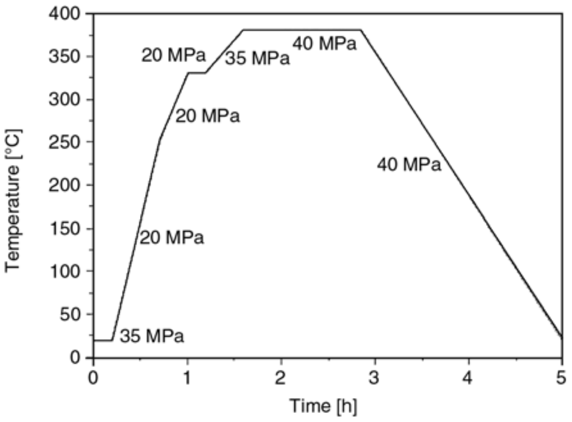

Figure 1. The temperature program of moulding

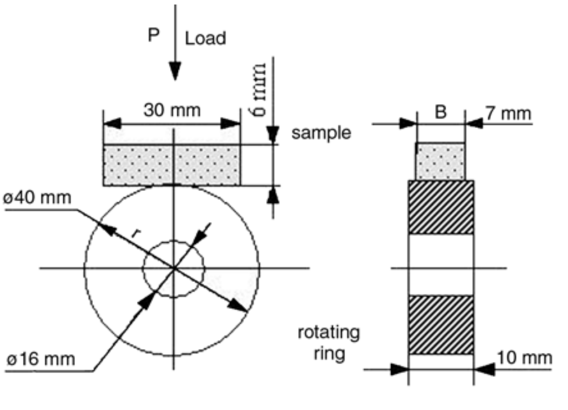

Figure 2. The contact schematic diagram for the friction couple

Table 1. Chemical composition of the GCr15 steel ring

Chemical composition (mass fraction, %)					
C	**Mn**	**Si**	**P**	**S**	**Cr**
0.95–1.05	0.25–0.45	0.15–0.35	≤0.025	≥0.025	1.40–1.65

out at a linear velocity of 0.431 m/s in a period of 120 min with the loads of 200 N. Before each test, the stainless steel ring and the PI composite block were polished to a roughness (R_a) of about 0.2–0.3 μm. The block specimen was static and the GCr15 bearing was sliding against the block unidirectionally. The friction force was measured using a torque shaft equipped with strain gauges mounted on a vertical arm that carried the block, which was used to calculate the friction coefficient by taking into account the normal load applied. The width of the wear tracks was measured with a reading microscope to an accuracy of 0.01 mm. Then the specific wear rate (ω) of the specimen was calculated from Equation (2):

$$\omega = \frac{B}{L\cdot P}\left[\frac{\pi r^2}{180}\arcsin\left(\frac{b}{2r}\right) - \frac{b}{2r}\sqrt{r^2 - \frac{b^2}{2}}\right] \quad [\mathrm{mm^3/N\cdot m}] \qquad (2)$$

where B is the width of the specimen [mm], r is the semi diameter of the stainless steel ring [mm], and b is the width of the wear trace [mm], L is the sliding distance in meter, P is the load in Newton. The tests were repeated for three times, the wear tracks of the composite and stainless steel specimens were examined on a JSM- 5600LV scanning electron microscope (SEM). In order to increase the resolution for the SEM observation, the tested composite specimens were plated with gold coating to render them electrically conductive.

3. Results and discussion

3.1. Morphology analysis

The SEM morphologies of the untreated and rare earth treated CF are shown in Figure 3. The surface of the untreated CF (Figure 3a) seems to be relatively smooth and the grooves were less obvious. The surface of the rare earth treated CF (Figure 3b) became rougher and there appeared more etched ridges with newly grooves and protuberances. The $LaCl_3$ solution can etch the surface of carbon fibers thus increased the surface roughness. The surface became rougher after rare earth treatment, i. e. the fibers possessed a larger surface area, which could contact with PI matrix and thus formed more mechanical interlocking sites. The mechanical interlocking provided a strong interface bonding even though other effects were relatively weak [15]. In addition, the enhancement of the surface roughness reduced the contact angle between fibers and PI and hence increased the wettability [16].

3.2. XPS analysis

The overall XPS spectra of different samples are shown in Figure 4. It can be observed that the fiber surfaces consisted mainly of carbon as indicated by the intense C1s peak at approximately 285 eV. In addition, a considerable amount of oxygen could be found by the O1s peak at approximately 533 eV, which varied to a certain extent with the different of treatment. The element information got from the XPS spectra is shown in Table 2. It can be found that the surface C element concentration of the untreated, rare earth treated CF samples were 84.5%, 81.7% respectively. A lower C concentration was found on the surfaces of the rare earth

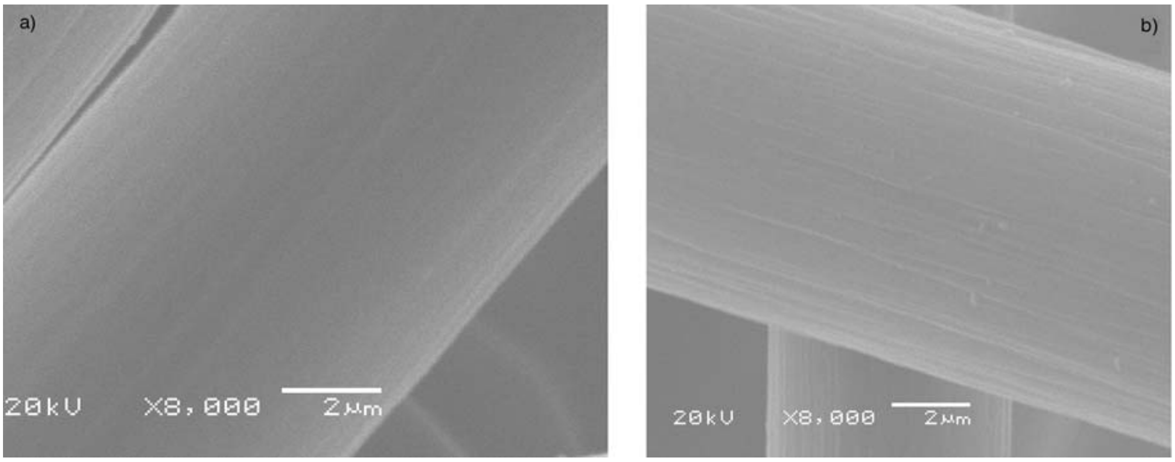

Figure 3. SEM morphologies of the untreated (a) and rare earth treated (b) CF

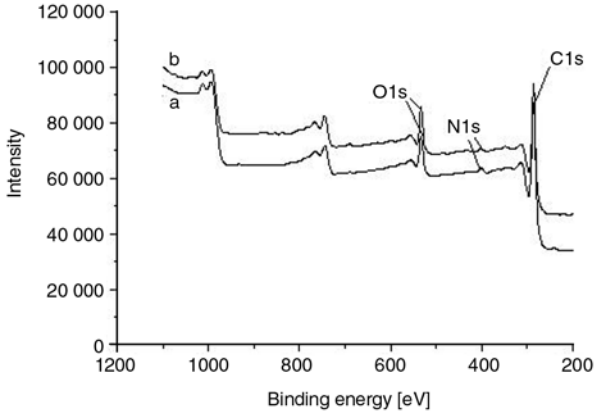

Figure 4. Overall XPS spectra of different samples: Untreated CF (a); Rare earth treated CF(b)

Table 2. XPS surface element analysis data of CF and rare earth treated CF

Samples	C [%]	O [%]	O/C [%]
CF	84.5	15.5	18.3
Rare earth treated CF	81.7	18.3	22.4

treated CF sample compared with that of the untreated one. The surface O concentration of the untreated, rare earth treated CF samples were 15.5%, 18.3 %, respectively. The number of functional groups for untreated CF sample was attributed to the residual groups of the polymeric precursor, polyacrylonitrile and the polymeric sizing on the CF after washing in acetone with ultrasound. La^{3+} has high electronegativity thus has great oxidative ability, more new-formed oxygen-contained groups can form on the surface when CF was soaked in rare earth solution, which resulted in an increase in oxygen content as well as the O/C ratio.

The curve fitting spectra of C1s of the untreated and rare earth treated CF is revealed in Figure 5. The main C1s peak is presented at 285 eV, which correspond to the graphitic linkage of carbon fiber. In addition, there are some peaks appeared at the higher binding energy positions compared with the main C1s peak and they correspond to different oxygen-containing groups. Table 3 gives the different oxygen-contained carbon structural components possibly existed on CF. Each functional group gives rise to a signal in the XPS spectrum with a particular range of binding energies.

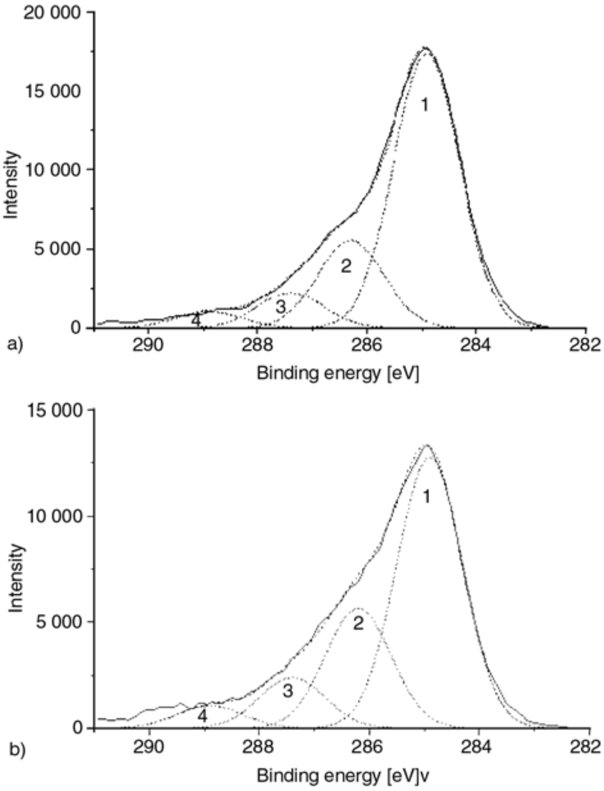

Figure 5. Curve fitting spectra of C1s of the untreated (a) and rare earth treated (b) CF samples

Table 3. Component peak positions used in C1s curve fitting

Peak no.	Functionality	Binding energy [eV]
1	–C–C–	285.0
2	–C–OH, –C–O–C–	286.3
3	Bridged structure	287.4
4	C=O, –COOR	288.9

Table 4. Surface component analysis of C1s curve of different carbon fiber samples

Sample	Peak 1 Area [%]	Peak 2 Area [%]	Peak 3 Area [%]	Peak 4 Area [%]
CF	67.0	21.0	8.3	3.7
Rare earth treated CF	58.5	25.9	10.6	5.0

According to Table 3, the fitting results of C1s of different samples are shown in Table 4. It is noted that the C1s spectra included another three peaks except main ‘graphitic’ peak at 285 eV. After rare earth treatment, the content of –C–C– decreased while the content of –C–OH, –C–O–C–, Bridged structure, C=O and –COOR increased, which increased total surface energy and their polarity thus enhanced the wettability of the CF with the PI matrix. Better wetting can improve the adhesive bond strength by increasing the thermodynamic work of adhesion or by reducing the number of interfacial defects [17]. Adhesion between CF and PI matrix improved, which played an important role on the flexural strength and tribological properties of CF filled polymer composites.

3.3. Flexual strength of PI composites

The flexual strength of CF and rare earth treated CF filled PI samples was 193 MPa, 212 MPa, respectively. It can be seen that the flexural strength of PI composite filled with the rare earth treated CF is improved by 10.4% compared with that with the untreated one. The strength of fiber reinforced composites strongly depends on the interfacial adhesion between fibers and matrix. When there is a strong adhesion between fibers and matrix, the load stress is efficiently transmitted from the matrix to fibers and the fibers can successfully carry the load, so the fiber can bring more reinforcement [18]. The rare earth treated CF filled PI composite had a higher flexual strength, which indicated that the rare earth treatment improved the interfacial adhesion between carbon fibers and PI matrix. Adhesion between CF and PI matrix improved, which played an important role on improving the tribological properties of CF reinforced polymer composites.

3.4. The tribological property

Figure 6 shows the friction coefficient and wear rate of untreated CF/PI and rare earth treated CF/PI composites at a sliding speed of 0.431 m/s under 200 N. It was found that the wear rate of the rare earth treated CF/PI composite decreased drastically than that of the untreated CF/PI composites, though the friction coefficient decreased slightly. It can be concluded that the reinforcement effect of the rare earth treated CF was better than that of the untreated one. The reason may be that the adhesion between CF and PI matrix improved greatly after rare earth treatment. An improved adhesion can transmit the load from the matrix to fibers efficiently and prevent the peeling off of CF, which resulted in better tribological behaviors. However, the untreated CF can not bear the load efficiently and can be easily peeled off and there formed third body, which can result in serious abrasive wear to the surface of the PI composites in the friction process, which resulted in a higher friction coefficient and wear rate.

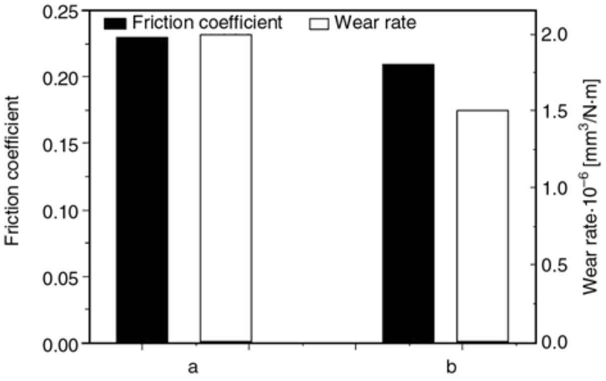

Figure 6. Variation of the friction coefficient and wear rate of the untreated CF/PI (a) and rare earth treated CF/PI (b) composites (0.431 m/s and 200 N)

4. Conclusions

The rare earth treatment could increase the surface roughnesss thus formed more mechanical interlocking sites, which can improve the interfacial bonding. Moreover, the rare earth treatment could increase the O/C ratio of the carbon fiber surface and lots of active functional groups formed there, which can improve the wettability by enhancing the surface energy and thus enhanced the interfacial bonding. In conclusion, the surface treatment favored the improvement of the higher interface strength and so had good effect on improving the tribological behaviors of the composites.

Acknowledgements

The authors would like to acknowledge the financial support of the Innovative Group Foundation from NSFC (Grant No. 50421502) and the National Natural Science Foundation of China (Grant No.50475128) and the important direction project for the knowledge innovative engineering of Chinese Academy of Sciences (Grant No. KGCX3-SYW-205).

References

[1] Bahadur S., Polineni V. K.: Tribological studies of glass fabric-reinforced polyamide composites filled with CuO and PTFE. Wear, **200**, 95–104 (1996).

[2] Price D. M.: Vapor pressure determination by thermogravimetry. Thermochimica Acta, **367–368**, 253–262 (2001).

[3] Okabe T., Takeda N.: Size effect on tensile strength of unidirectional CFRP composites -experiment and simulation. Composites Science and Technology, **62**, 2053–2064 (2002).

[4] Choi M. H., Jeon B. H., Chung I. J.: The effect of coupling agent on electrical and mechanical properties of carbon fiber/phenolic resin composites. Polymer, **41**, 3243–3252 (2000).

[5] Varelidis P. C., McCullough R. L., Papaspyrides C. D.: The effect on the mechanical properties of carbon/epoxy composites of polyamide coatings on the fibers. Composites Science and Technology, **59**, 1813–1823 (1999).

[6] Ogawa H., Satio K.: Oxidation behavior of polyacrylonitrile fibers evaluated by new stabilization index. Carbon, **33**, 783–788 (1995).

[7] Wu Z. H., Pittman C. U., Gardner S. D.: Nitric acid oxidation of carbon fibers and the effects of subsequent treatment in refluxing aqueous NaOH. Carbon, **33**, 597–605 (1995).

[8] Toyoda M., Katoh H., Inagaki M.: Intercalation of nitric acid into carbon fibers. Carbon, **39**, 2231–2237 (2001).

[9] Basova Y. V., Hatori H., Yamada Y., Miyashita K.: Effect of oxidation-reduction surface treatment on the electrochemical behavior of PAN-based carbon fibers. Electrochemistry Communications, **1**, 540–544 (1999).

[10] Theodoridou E., Jannakoudakis A. D., Jannakoudakis P. D., Andonoglou P., Besenhard J. O.: Electrochemical oxidation of PAN- and pitch-based carbon fibers and deposition of palladium on the obtained materials. Synthetic Metals, **87**, 225–229 (1997).

[11] Yue Z. R., Jiang W., Wang L., Gardner S. D., Pittman C. U.: Surface characterization of electrochemically oxidized carbon fibers. Carbon, **37**, 1785–1796 (1999).

[12] Pittman C. U., Jiang W., Yue Z. R., Gardner S. D., Wang L.: Surface properties of electrochemically oxidized carbon fibers. Carbon, **37**, 1797–1807 (1999).

[13] Wu G. M.: Oxygen plasma treatment of high performance fibers for composites. Materials Chemistry and Physics, **85**, 81–87 (2004).

[14] Zhang X. R., Pei X. Q., Wang Q. H.: The effect of fiber oxidation on the friction and wear behaviors of short-cut carbon fiber/polyimide composites. Express Polymer Letters, **1**, 318–325 (2007).

[15] Harris B., Braddell O. G., Almond D. P.: Study of carbon fibers surface treatment by dynamic mechanical analysis. Journal of Materials Science, **28**, 3353–3366 (1993).

[16] Boudou J. P., Paredes J. I., Cuesta A., Martinez-Alonso A., Tascon J. M. D.: Oxygen plasma modification of pitched-based isotropic carbon fibers. Carbon, **41**, 41–56 (2003).

[17] Wu S.: Polymer interface and adhesion. Marcel Dekker, New York (1982).

[18] Choi M. H., Jeon B. H., Chung I. J.: The effect of coupling agent on electrical and mechanical properties of carbon fiber/phenolic resin composites. Polymer, **41**, 3243–3252 (2000).

eXPRESS Polymer Letters Vol.1, No.10 (2007) 673–680
Available online at www.expresspolymlett.com
DOI: 10.3144/expresspolymlett.2007.92

Kinetic study of negative dry-film photoresists

A. K. Diby[1,2], *V. Yu. Voytekunas*[1,3], *M. J. M. Abadie*[1,4*]

[1]Laboratory of Polymer Science & Advanced Organic Materials – LEMP/MAO, CC 021, Université Montpellier II, Place Bataillon, 34095 Montpellier Cedex 05, France
[2]Université Cocody d'Abidjan, Abidjan, Côte d'Ivoire
[3]Singapore Institute of Manufacturing Technology – SIMTech, 71 Nanyamg Drive, 638075, Singapore
[4]School of Materials Science & Engineering, Nanyang Technological University, 50 Nanyang Avenue, 639798, Singapore

Received 1 June 2007; accepted in revised form 9 August 2007

Abstract. Thanks to the differential photocalorimetry technique DPC, characteristics of negative photoresists (Riston® PM 215 and Riston® MM 140, 1 mil or 25.4 μm thickness) to be developed in nonorganic aqueous medium) used in microlithography are highlighted. The photoreactivity (being evaluated by DPC) of the matrix polymer involved in these Riston® is critical for ensuring good lithographic performance. The influence of temperature and irradiation intensity on kinetic parameters such as the enthalpy of reaction ΔH, the time of induction (I_t), the conversion rate to the maximum peak (RPM), the coefficient rate of the reaction (k), the conversion rate α, and the polymerization rate R_p were studied.
All the results highlights not only the strong differences between the two Riston® studied, but also the great reactivity of Riston® PM 215 compared to Riston® MM 140.

Keywords: *thermosetting resins, photoresists, differential photocalorimetry, kinetics, photoreactivity*

1. Introduction

The explosive growth in performance of semiconductors devices has been fueled in part by advances in microlithography, which in turn fueled similar advances in photoresist technology [1]. The ability to continually shrink the feature size and improve the performance has occurred because of advancements in materials. Tremendous advances have been made in the development of negative resist systems. Their sensitivity, ease of chemical modification, and low cost have made them the materials of choice for both Printed Wiring Boards circuitry industry and Printed Circuit Boards industry, and they are being continually improved to provide greater resolution, ease of processing, and improved physical and thermal properties. For semiconductor industry, it has been necessary to provide negative resists to meet the ever-increasing circuit density requirements for every new generation of semiconductors devices.

Epoxy materials are attractive alternatives, since there are a large variety of epoxidized polymers available in both solid and liquid form. These materials generally offer excellent adhesion to semiconductor surfaces, good sensitivity, and low cost. The ever increasing complexity of integrated circuits – multi-layers printed circuits (Ultra Large Scale Integration) and the fact that the epoxy based – photoresists cannot be easily stripped after etching require new photosensitive dry film photopolymers such as DuPont Riston® Dry Film Resists. Dry film resist has numerous advantages such as good conformability, excellent adhesion on any substrate, no liquid handling due to absence of solvent, excellent thickness uniformity over the whole wafer, no formation of edge beads and low exposure energy [2].

---

[*] Corresponding author, e-mail: marc@ntu.edu.sg

The aim of the present study involves the characterization of new Riston® products. The effect of some factors on the rate of crosslinking and degree of conversion were assessed.

A series of Dry Films (1 mil thickness – 0.0254 mm), used as received, were evaluated as negative photoresist and characterized via free radical polymerization technique by DPC. Specimens were prepared by casting polymer films onto alumina plates (of diameter equal to 6 mm).

1.1. Photolithography

Lithographic technology has been based on projecting an optical image of a device onto a resist in order to record the image for subsequent processing steps. Photolithography is the process of transferring geometric shapes onto the substrate (silicon wafer, pyrex, metal, ceramic).

When the image is projected onto the wafer, the photoresist materials undergo some light-sensitive chemical reactions, which cause the regions exposed to light to be either more (positive photoresist) or less (negative photoresist) susceptible to chemical etch. The resist is then 'developed' by immersion in a developer, which removes either the exposed (positive-tone) or the unexposed (negative-tone) photoresist. The resulting wafer then has a pattern coating on its surface. The pattern can then be etched into the underlying wafer by either a wet chemical etch or a plasma etch. When the resist image is transferred into the substrate by etching and related processes, the resist film that remains after development serves as a protective mask. The resist film must withstand the etchant and protect the underlying substrate while the bared areas are being etched. The remaining resist film is finally stripped, leaving an image of the desired circuit in the substrate.

1.2. Photoresist

Photoresist is a complex organic mixture of polymers and low-molecular weight additives that serves as light-sensitive template for manufacturing semiconductor integrated circuits. These polymers with a combination of properties such as high photosensitivity, good solubility, the ability to form films, good thermal stability, resistance towards solvent after crosslinking, resistance towards plasma and etching agents, are very important for practical use as negative photoresist materials. Resist transparency is a dominant factor in the choice of resist materials.

Exposure to the UV light causes the negative resist to become polymerized, and more difficult to dissolve. Indeed, when exposed to UV light in the range from 200 to 300 nm (4 to 6 eV) the polymers form 'radical species' which can result in crosslinking, increased molecular weight, insolubilization, and film embrittlement [3]. The insolubilization can be achieved by using materials which, upon UV exposure, are photochemically rearranged to form new insoluble products. To increase molecular weight, photoinitiators are generally used.

2. Experimental procedures

2.1. Materials

Because of environmental concerns, a set of new resists were investigated to try to enhance the process latitude, reduce the manufacturing cost of resists and to meet safety requirements in a manufacturing environment. As such, DuPont Printed Circuit Materials supplied two types of Riston® which requires further characterization:

- Riston® MultiMaster MM 100 Series: a 'general purpose' dry film for acid and alkaline etch, copper, tin, nickel and gold plating,
- Riston® PlateMaster PM 100 Series: negative working, aqueous processable dry film photoresists. Specially designed for pattern plating applications on scrubbed and unscrubbed electroless copper and direct surfaces, it is functional in acid etching and suitable for some nickel/gold plating applications with fine line capability and wide exposure latitude.

The resist formulation, a thin film 'dry', is sandwiched between a polyolefin sheet and a polyester base, rolled up on a support core.

2.2. Method

The analysis of the photoreactivity has been perfomed by Differential Scanning Photocalorimeter (DPC), method widely described in [4]. Note that the technique is based on heat produced during all polymerization or crosslinking process, when the photoreactive compound is irradiated.

The exotherm of the curve leads to assess some kinetic paramteres such as:

– enthalpy of the photochemical reaction (ΔH),

– induction time (I_t) of the system corresponding to the consumption of 1% of monomer. In practice, it gives a good information of the photo reactivity of the film; the lower the induction time, the higher the reactivity of the photosensitive layer,

– resin reacted at maximum peak (RPM),

– percentage of conversion (degree of conversion α),

– coefficient of rate k given by Sestak and Berggren equation, see Equations (1) and (2) [5]:

$$R_T = -\frac{\mathrm{d}\alpha}{\mathrm{d}t} = k(T)\alpha^m(1-\alpha)^n \tag{1}$$

with

$$k(T) = Z\exp\left(-\frac{E_a}{RT}\right) \tag{2}$$

where m and n the oder of initiation and propagation respectively, E_a the activation energy of the crosslinking reaction.

The specimen of about 1 mg is light-cured with UV light of intensity of 1.2 mW/cm^2, 2.2 mW/cm^2 and 3.3 mW/cm^2 respectively. The measurements are carried out in air atmosphere. The sample analyzed is peeled out from polyethylene sheet, sticked directly to the pan, the upper layer being protected by the polyethyleneterephthalate film. This geometry of the sample allows preventing the sample from air, inhibitor of radical polymerization.

3. Results and discussion

3.1. Kinetic parameters

3.1.1. Effect of intensity I of the irradiation

The results representing evolutions of these parameters, according to intensity I, are consigned in Table 1 for Riston® MM 140 and Riston® PM 215. The Table 1 shows that intensity I of the irradiation in the range of 1 to 3 mW/cm^2 does not have very significant effect on the kinetic parameters such as ΔH, RPM, I_t; however, the coefficient rate k increases with the intensity. In addition one observes a greater reactivity for Riston® PM 215 (larger values of ΔH, k, RPM and smaller value of I_t).

According to the nature of Riston®, it is noted that the variation of the enthalpy of reaction is not very sensitive for the two Ristons and a slight difference appears for the time of induction. Significant differences appear in the case of the percentage of conversion to the maximum peak (RPM) and of the coefficient rate k. These last two parameters of Riston® PM 215 are higher than those of Riston® MM 140. That is probably due to the nature of their initial composition related to the specificity of their use. Although the composition of these samples is confidential (by DuPont Technologies) and therefore unknown, we can emphasise that the different reactivity observed for the two Ristons® is probably due to the chemical structure of the (meth)acrylate used, especially the presence of flexibilizer along the chain bearing the (meth)acrylate function which makes it more reactive. For example the use of triacrylate product such as trimethylolpropane-tri(ethyleneoxyde)acrylate [TMPT(EO)A] compared to trimethylolpropane-triacrylate [TMPTA] or a mixture TMPTA/TMPT(EO)A could explain the differences observed. The presence of oxygen of the ethyleneoxide structure –O–CH_2–CH_2– linked to the acrylate function for TMPT(EO)A gives more flexibility to the chain and therefore permits a better reactivity of the acrylate function. This structure-property relationship could explain why Riston® PM 215 is more photosensitive than Riston® MM 140.

3.1.2. Effect of temperature of polymerization

Tables 2 and 3 demonstrate that the temperature of polymerization constitutes a significant parameter and strongly affects the kinetic behaviour of the crosslinking polymerization of the photoresists.

Table 1. Comparative values of the kinetic parameters of the Ristons® studied (1 mil thickness – 0.0254 mm)

	Riston® MM 140				**Riston® PM 215**			
I [mW/cm²]	**ΔH [J/g]**	**I_t [s]**	**RPM α [%]**	**k [min⁻¹]**	**ΔH [J/g]**	**I_t [s]**	**RPM [%]**	**k [1/min]**
1.2	53±4	2.9±0.1	6.9±0.3	9.2±0.2	60±4	2.1±0.1	9.8±0.3	12.6±0.2
2.2	53±4	2.9±0.1	6.2±0.3	9.7±0.2	59±4	1.9±0.1	9.7±0.3	13.8±0.2
3.3	58±4	2.9±0.1	6.3±0.3	10.3±0.2	62±4	1.8±0.1	9.6±0.3	16.8±0.2

(ΔH enthalpy, I_t induction time, *RPM* resin reacted at peak maximum, k coefficient of rate)

Table 2. Effect of measurement temperature on kinetic parameters, @ I = 3.3 mW/cm^2, for Riston® MM 140

Temperature [°C]	ΔH [J/g]	RPM α [%]	I_t [s]	t_g [s]	k [min^{-1}]	α_f·100 [%]	R_{pmax} [min^{-1}]
25	58±4	6.3±0.3	2.9±0.1	4.8	10.3±0.2	30	1.8±0.1
35	95±6	8.9±0.3	1.8±0.1	3.6	14.8±0.2	40	3.2±0.1
45	160±10	12.1±0.5	1.6±0.1	3.4	18.1±0.3	80	4.2±0.1
55	170±10	14.1±0.7	1.3±0.1	3.0	21.4±0.3	–	–
65	168±10	13.0±0.7	1.2±0.1	2.8	24.8±0.3	99	5.8±0.1

(ΔH enthalpy, *RPM* resin reacted at peak maximum, I_t induction time, t_g gel time, k coefficient of rate, α_f ×100 degree of conversion, R_p rate of polymerization)

Table 3. Effect of measurement temperature on kinetic parameters, @ I = 3.3 mW/cm^2, for Riston® PM 215

Temperature [°C]	ΔH [J/g]	RPM α [%]	I_t [s]	t_g [s]	k [min^{-1}]	α_f·100 [%]	R_{pmax} [min^{-1}]
25	62	9.6±0.3	1.8±0.1	3.6	16.8±0.2	40	3.6±0.1
35	76	10.0±0.3	1.5±0.1	3.0	20.4±0.3	45	4.8±0.1
45	119	12.3±0.5	1.3±0.1	2.8	22.6±0.3	55	6.0±0.1
55	175	13.7±0.5	1.2±0.1	2.6	25.9±0.3	85	7.0±0.1
65	266	15.1±0.7	1.1±0.1	2.6	30.4±0.3	99	7.2±0.1

(ΔH enthalpy, *RPM* resin reacted at peak maximum, I_t induction time, t_g gel time, k coefficient of rate, α_f ×100 degree of conversion, R_p rate of polymerization)

The examination of Tables 2 and 3 shows that generally the increase in the temperature contributes more reactivity in both samples (ΔH, k, α increase with the temperature and I_t and gel time t_g decreasing when the temperature increases). Riston® PM 215 is more reactive across all temperatures except at 65°C, at which similar reactivity were observed (close α and I_t).

It should be highlighted that at higher temperatures the period of induction is less significant. It is thus necessary to determine an optimum temperature for each type of photoresist to obtain a good polymerization. Our study locates this temperature to be 65°C, at which the conversion rate is 99%.

The influence of the temperature also gives access the energy of activation while following the evolution of the coefficient rate k as a function of $10^3/T$ according to the expression $\ln k = \ln Z - E_{has}/RT$. We represented on Figure 1 these variations, in semi-logarithmic scale, T is the temperature of measurement. One reaches easily the value of the energy of E_a activation of the reaction of polymerization of the two types of Riston® thanks to the slope of these lines. The value of E_a is about (17.7±0.5) kJ/mol and (11.7±0.5) kJ/mol respectively for Riston® MM 140 and Riston® PM 215. As the activation energy of Riston® PM 215 is lower than the Riston® MM 140, it appears that the conversion of the Riston® PM 215 is easier than that of the Riston® MM 140, which confirms the superior photosensitivity of the Riston® PM 215.

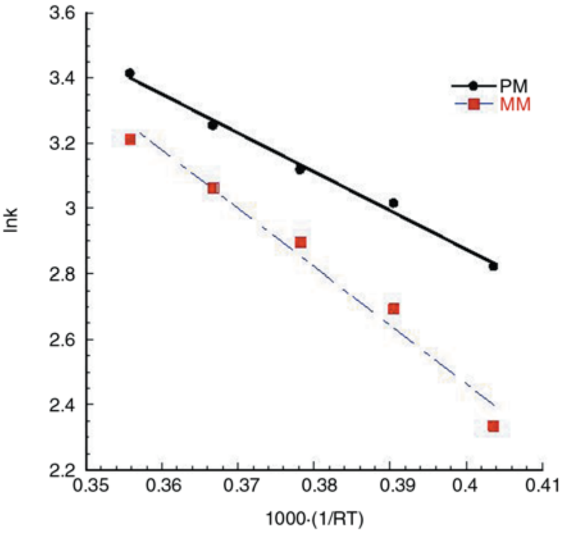

Figure 1. Variation of ln$k$ as function of temperature of measurement (Riston® PM 215, Riston® MM 140)

3.2. Others kinetic parameters

The photoreactivity of Riston® photoresists through the polymerisation speed and the conversion rate under UV will be analyzed.

3.2.1. Degree of conversion

Figures 2 and 3 present the evolution of the conversion rate α according to the time of irradiation of Riston® MM 140 and Riston® PM 215 respectively for I = 3.3 mW/cm^2.

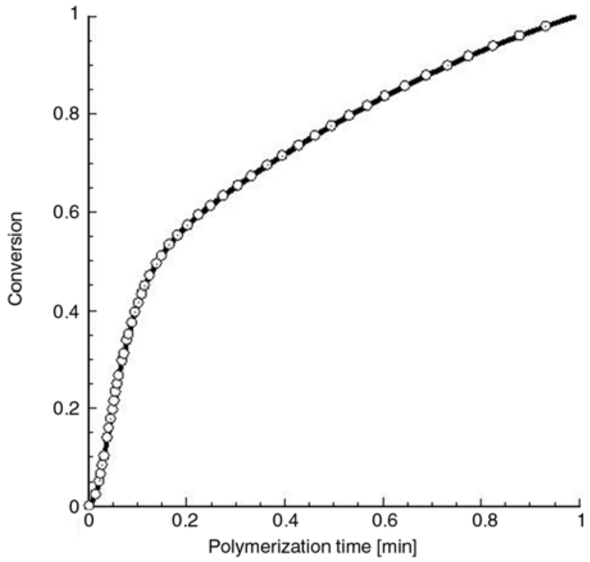

Figure 2. Evolution of conversion rate as function of irradiation time, for Riston® MM 140, at $T = 65°C$ and $I = 3.3$ mW/cm^2

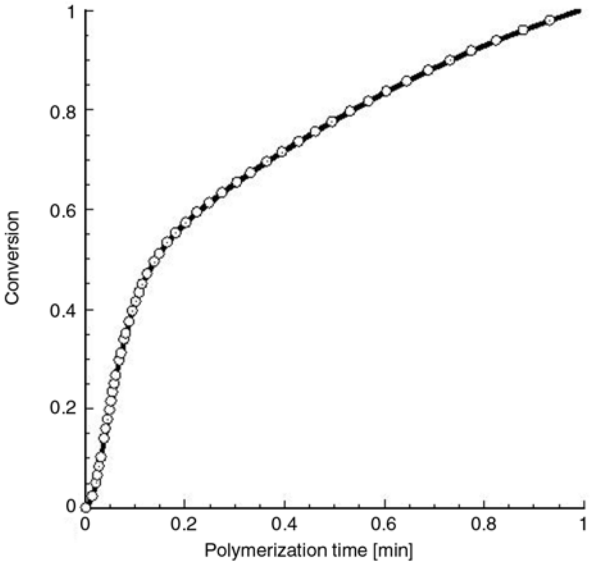

Figure 3. Evolution of conversion rate as function of irradiation time, for Riston® PM 215, at $T = 65°C$ and $I = 3.3$ mW/cm^2

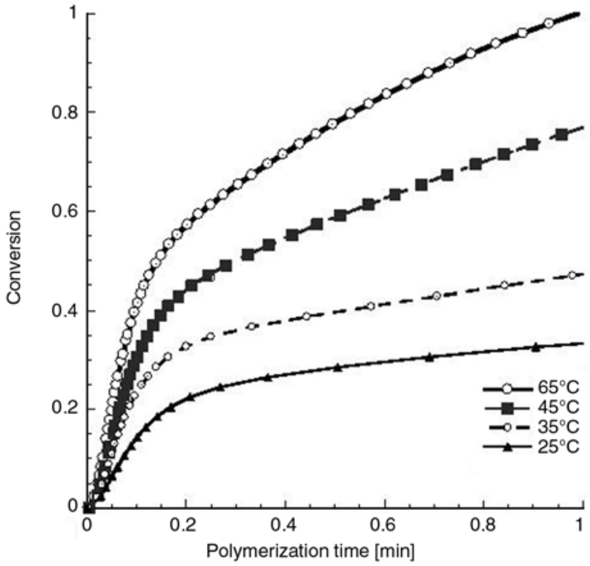

Figure 4. Evolution of conversion rate as a function of polymerization time at different temperatures (Ristons® MM 140, $I = 3.3$ mW/cm^2)

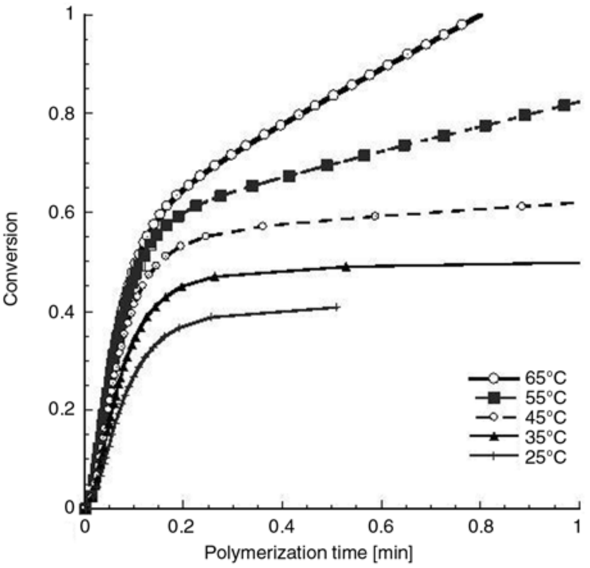

Figure 5. Evolution of conversion rate as a function of polymerization time at different temperatures (Ristons® PM 215, $I = 3.3$ mW/cm^2)

Rate of photoconversion of 58 and 65% of Riston® MM 140 and Riston® MP 215 respectively, are reached after 12 s of irradiation. The rate of 98% of conversion is obtained at the end of 54 s of irradiation for sample Riston® MM 140 and 48 s for sample Riston® PM 215. Although the two samples have a good photoreactivity, that of Riston® PM 215 is superior.

3.2.2. Effect of the temperature

The influence of the temperature of measurement on the photoconversion, under irradiation intensity $I = 3.3$ mW/cm^2 is illustrated in Figures 4 and 5 (the experimental conditions are the same for all temperatures).

For the Riston® MM 140 (Figure 4), at the end of one minute reaction, the rate of photoconversion is 33, 46 and 77% when the temperature increases from 25 to 35 and 45°C respectively. And finally conversion is quasi complete at 65°C.

With regards to the Riston® PM 215, Figure 5 shows that the limiting conversion rate of 40% is reached upon 30 s of irradiation at 25°C. When temperature increases from 35 to 55°C, the conversion rate, at the end of one minute of irradiation, is respectively 50, 62 and 82%. The quasi complete consumption of the double bonds C=C (since the resists contain a significant amount of multifunctional acrylate) is observed at 65°C upon 48 s irradiation.

Moreover, the curves representing the evolutions of the rate of photoconversion indicate that the temperature of polymerization play a significant role in the kinetics of the crosslinking polymerization of Ristons®. Indeed, when the temperature of measurement is high, the reactive species benefit from a larger kinetic energy and an improved mobility. The period of induction is less significant and the values of the limiting rate of photoconversion are sufficiently high to predict a complete reticulating polymerization samples.

3.2.3. Effect of intensity I of irradiation

The effect of irradiation intensity on the conversion rate is analyzed at the temperature $T = 65$°C (temperature inducing the optimum value of the kinetic parameters).

For both samples the curves have the same slope:

– fast increase in the conversion rate from the very start of the exposure:

for Riston® PM 215, during this period, the conversion rate is independent of the intensity during the 9 first second of the exposition (at 9 s, $\alpha = 58\%$ regardless of the intensity I);

– increase much slower at the end of the exposure.

The influence of the irradiation intensity increases with the exposition time. For the most reactive Riston® PM 215, conversion rates of 100% is obtained at the end of 49 s with an intensity of $I = 3.3$ mW/cm^2 while the conversion rate is only 90% at the end of one minute with an intensity of $I = 2.2$ mW/cm^2. The increase in intensity I is accompanied by an increase in the conversion rate throughout the process of crosslinking reaction. This result is justified by the fact that combined effects of the temperature, which increases the mobility of the reactive species and the intensity of the irradiation which breaks the bonds C=C, makes the medium more favourable. Decker (1996) showed that the luminous flow of excitation plays a dominating role in the reactions of polymerization process; it acts by its wavelength, its intensity and its homogeneity. Quantum yield being related to the intensity of the irradiation, Figure 6 shows clearly that any increase in the light intensity of radiation UV involves an increase proportional in limiting conversion and in parallel a reduction in the period of induction is observed (see Table 1).

The curves of photoconversion (Figures 7 and 8) clearly exhibit that Riston® PM 215 has a rate of crosslinking higher than Riston® MM 140 for identical experimental conditions.

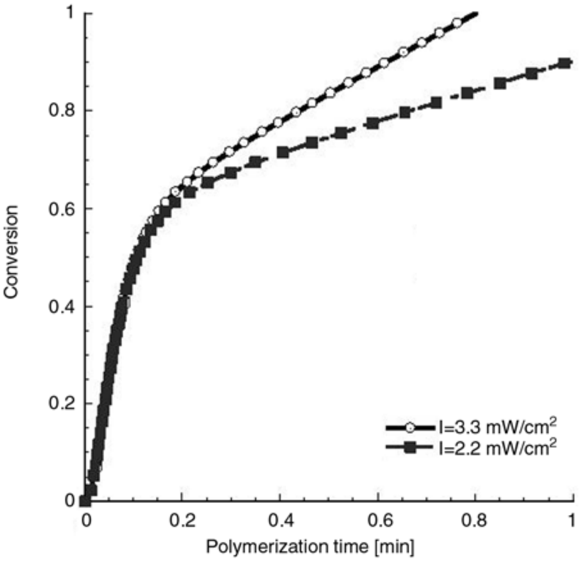

Figure 6. Influence of intensity I on conversion rate at $T = 65$°C, $I = 3.3$ et $I = 2.2$ mW/cm^2 (Riston® PM 215)

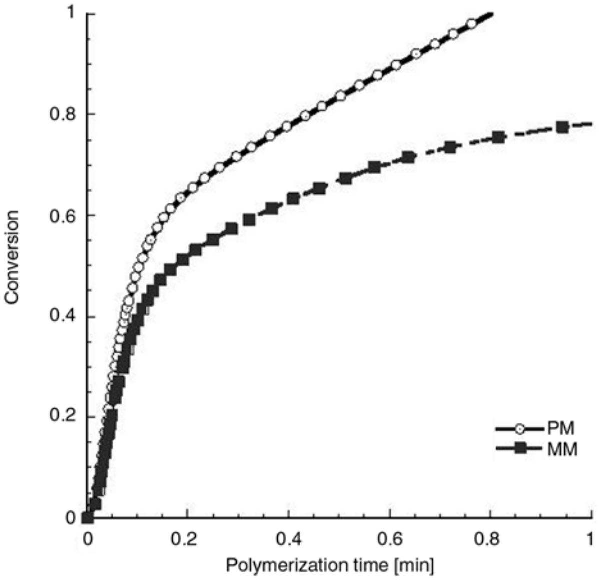

Figure 7. Comparison of conversion rate evolution during polymerization of the two Ristons® ($I = 3.3$ mW/cm^2 and $T = 65$°C)

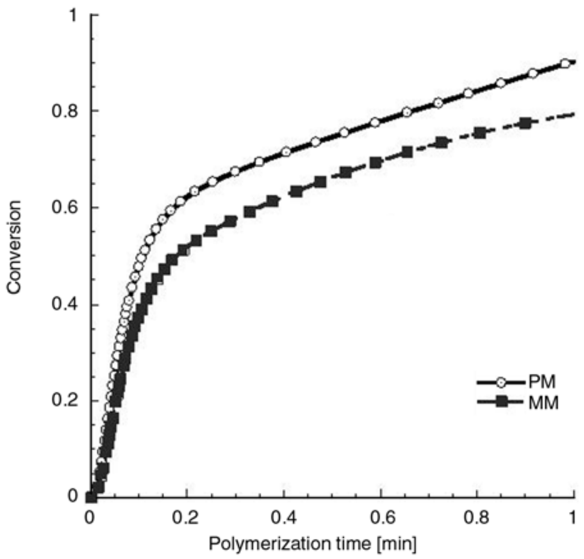

Figure 8. Comparison of conversion rate evolution during polymerization of the two Ristons® (I = 2.2 mW/cm^2 and T = 65°C)

From the two samples, the Riston® PM 215 is most reactive. It is may be an intrinsic property which is due to its composition and its structure.

This observation is also emphasized regardless of the temperature of measurement and the intensity of the irradiation.

The effect of the temperature shows that the conversion rate is maximum at T = 65°C. We also observed that the irradiation time necessary to obtain a maximum conversion rate is one minute (1 min).

The irradiation intensity of I = 3.3 mW/cm^2 is sufficient and induces a larger conversion rate.

These curves highlight the influence of the nature of the resist on the kinetic profile. Indeed it appears clearly that the values of final conversion (estimated approximately at the end of a minute of reaction) depend primarily on the formulation or basic composition of the resist. Thus in the case of the system PlateMaster 100 conversion proves to be almost complete (value of final conversion near to 100%) whereas this value is 80% for the system MultiMaster 100. The remarkable reactivity of PlateMaster 100 is probably due to its composition: the functionality of the monomer, the nature of the initiators and activators. If we examine the kinetic profile of the two systems closely, we notice that it is the same during the first three seconds of the reaction. That highlights the importance of the mobility of the polymeric radicals in growth and the density of the formed polymeric network.

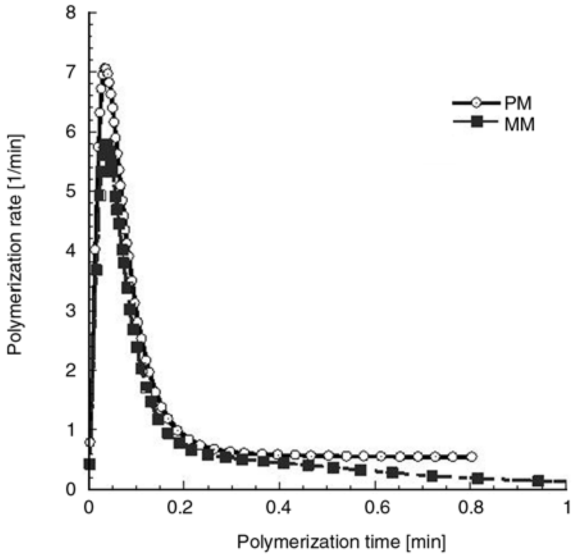

Figure 9. Comparison of conversion rate evolution during polymerization of the two Ristons® (T = 65°C and I = 3.3 mW/cm^2)

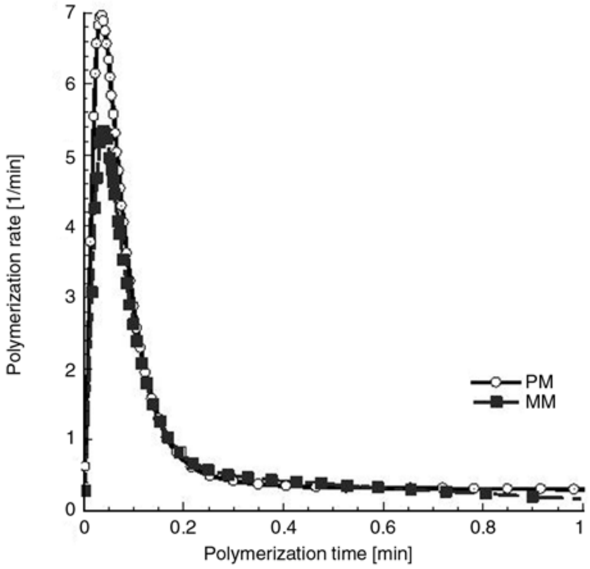

Figure 10. Comparison of conversion rate evolution during polymerization of the two Ristons® (T = 65°C and I = 2.2 mW/cm^2)

3.3. Photopolymerization rate

Figures 9 and 10 represent the evolution of polymerization rate as function of irradiation time for the two samples studied at both intensity I = 3.3 mW/cm^2 and I = 2.2 mW/cm^2.

The photopolymerization, of the two samples, begins with a maximum rate which decreases quickly. The maximum value, reached at the end of 3 s, is 5.80 min^{-1} for Riston® MM 140 and 7 min^{-1} for Riston® PM 215. The larger reactivity of Riston® PM 215 is noticed here.

The strong reactivity of Riston® PM 215 compared to Riston® MM 140 is highlighted by the maximum values of polymerization rate.

The crosslinking photoreaction of the two samples under UV exposure as a function of time indicates that the reaction was fast during the first second and then followed attenuation (Figure 9). It is very short even if the intensity of irradiation is relatively weak ($I = 2.2$ mW/cm^2) and constitutes a major asset in the process of photolithography (Figure 10).

It appears clearly that the value of limiting polymerization rate also depends on the formulation or basic composition on the photoresist.

4. Conclusions

The kinetics of reticulation of negative photoresists allowed, by differential photocalorimetry with compensation of power (DPC), the quantification of a certain number of significant parameters such as enthalpy of polymerization, induction time, coefficient of rate, activation energy and the conversion rate.

We examined the effect of irradiation intensity and temperature on several kinetic parameters (ΔH, k, I_t), conversion to the reacted maximum peak (RPM), the degree of conversion α and the polymerization rate R_p.

The values of these kinetic parameters (ΔH, k, I_t and RPM) indicate that Riston® PM 215 presents a stronger photoreactivity compared to Riston® MM 140, probably due to the difference in the chemical structure of the acrylates used. Increasing the intensity increases the photoconversion throughout the polymerization process for the two samples. While monitoring, by DPC, the evolution of the photoconversion of irradiated film, one finds a kinetic curve representing an almost complete conversion. The high values of the limiting conversion rate and the polymerization rate show that the reactivity of both the radical initiators and monomers in the formulation of these two samples is very significant. The photoconversion is not only quasi-instantaneous but also completes at temperature $T = 65$°C; this value would thus be indicated during the irradiation in the microlithographic process.

Although at $T = 65$°C the two samples have similar reactivities, the low value of the energy of activation is obtained for Riston® PM 215 attesting that the conversion of this Riston® is easier and confirms its strong photosensitivity compared to Riston® MM 140.

All kinetic parameters studied emphasized the strong photoreactivity of Riston® PM 215. The photosensitivity of the Riston® PM 215 is better than Riston® MM 140 and hence makes it more suitable for an efficient microlithography.

We believe that the new generation of Riston® PM 215 is more powerful on the kinetic level for an etching. Our study recommends its formulation to the industrials and to manufacturers of printed circuits with the following conditions for optimum performance: an irradiation of intensity $I = 3.3$ mW/cm^2 at the temperature $T = 65$°C.

References

[1] Brainard R., Baeclay G. G., Anderson E. H., Ocola L. E.: Resists for next generation lithography. Microelectronic Engineering, **61–62**, 707–715 (2002).

[2] Kukharenka E., Farooqui M. M., Grigore L., Kraft M., Hollinshead N.: Electroplating moulds using dry film thick negative photoresist. Journal of Micromechanics and Microengineering, **13**, 67–74 (2003).

[3] Shaw J. M., Gelorme J. G., LaBianca N. C., Conley W. E., Holmes S. J.: Negative photoresists for optical lithography. Journal of Research and Development, Optical Lithography, **41**, 81–94 (1997).

[4] de Almeida Y. B. M., Carrera L. C. M., Abadie M. J. M.: Photopolymerization of multifunctional acrylates MAM using trans-10,11-dibromodibenzosuberone as radical photoinitiator. European Polymer Journal, **32**, 1355–1360 (1996).

[5] Sestak J., Berggren G.: Study of the kinetics of the mechanism of solid-state reactions at increasing temperatures. Thermochimica Acta, **3**, 1–12 (1971).

eXPRESS Polymer Letters Vol.1, No.10 (2007) 681–687
Available online at www.expresspolymlett.com
DOI: 10.3144/expresspolymlett.2007.93

Mechanical properties of sisal fibre reinforced urea-formaldehyde resin composites

*J. B. Zhong, J. Lv, C. Wei**

Key Laboratory of New Processing Technology for Nonferrous Metals and Materials, Ministry of Education, Guilin University of Technology, Guilin541004, China

Received 6 June 2007; accepted in revised form 12 August 2007

Abstract. Alkali-treated sisal fibres were used as novel reinforcement to obtain composites with self-synthesized urea-formaldehyde resin as matrix phase. The composites were prepared by means of compression molding, and then the effects of sisal loading on mechanical properties such as impact strength, flexural strength, and wear resistance were investigated. In addition, water uptake was studied and structural features were revealed by the scanning electron microscopy (SEM). The composite with 30 wt% sisal fibres gives excellent flexural strength, water absorption, and especially the wear resistance showing that it has the most superior bonding and adhesion of all the composites. In particular, the highest value 9.42 kJ/m^2 of charpy impact strength is observed in the composite with 50 wt% sisal fibre. SEM micrographs of impact fractured and worn surfaces clearly demonstrate the interfacial adhesion between fibre and matrix. This work shows the potential of sisal fibre (SF) to improve the composite wear resistance and to be used in fibreboard.

Keywords: *polymer composites, mechanical properties, sisal fibres, urea-formaldehyde resin, micro-structure*

1. Introduction

Fibre reinforced polymer composites are being used in almost every type of applications in our daily life and its usage continues to grow at an impressive rate. The manufacture, use and removal of traditional composite structures usually made of glass, carbon and aramid fibres are considered critically because of the growing environmental consciousness [1]. In recent years, there is a growing interest in the use of biofibres as reinforcing components for thermoplastics and thermosets. Sisal fiber (SF), a member of the Agavaceae family is a biodegradable and environmental friendly crop. Moreover, sisal is a strong, stable and versatile material and it has been recognized as an important source of fibre for composites [2–4].

It is generally accepted that the mechanical properties of fiber reinforced polymer composites are controlled by factors such as nature of matrix, fiber-matrix interface, fiber volume or weight fraction, fiber aspect ratio etc. Many scientists are working in this field and the reinforcement of polymer with SF has been widely reported. Low-density polyethylene-sisal [5], Polyester-sisal [6], epoxy-sisal [7], polypropylene-sisal [8, 9], urea-formaldehyde-sisal [10], phenol-formaldehyde-sisal [11, 12], polyvinyl-acetate-sisal [13], and starch-based-sisal [14] are some of the promising systems. A further attempt to use sisal fibre as reinforcement for heat and pressure applications has been found in the literature [15]. Manikandan Naira *et al.* [16] studied the thermal behaviour of polystyrene composites reinforced with short SF by means of thermogravimetric and dynamic mechanical thermal analysis. It has been found [17] that matrix cracking, fibre bridging, fibre breakage and pull-out are the major fracture modes of sisal textile reinforced

---

*Corresponding author, e-mail: glweichun@glite.edu.cn

composites with pre-cracks under the static loading condition. However, despite the fact that several methods have been used and great strides have been made, there is still some lack of knowledge about wear resistance property of sisal reinforced polymer composites.

Urea-formaldehyde resins (UFR) are the most prominent examples of the class of thermosetting resins usually referred to as amino resins, even though new research efforts are needed to address to offset its major disadvantage. The use of UFR as a major adhesive by the forest products industry is due to a number of advantages, including low cost, ease of use under a wide variety of curing conditions, low cure temperatures, water solubility, resistance to microorganisms and to abrasion, hardness, excellent thermal properties etc.

The present paper describes the changes in the Charpy impact, flexural and wear resistance properties of SF/UFR blend composite as a function of weight fraction of SF. In addition to this, the effect of SF loading on water absorption tendencies of the composites has also been examined. Meanwhile, the surface morphology is studied and described. We conduct this study to determine whether the compatibility between UFR and SF is strong or weak, and to evaluate the abrasive wear resistance of the composites. It is anticipated that this study may open the way for future investigations in the use of SF in fiberboard so that the range of sisal's potential applications can be widened.

2. Experimental

2.1. Materials

Fibres were soaked in 2% NaOH solution in a water bath where the temperature was maintained throughout at 22±2°C for 24 h, then washed with distilled water and left to dry at room temperature before being put in an oven for 15 h at 70°C. Finally, fibers were chopped into 2–3 mm size.

Liquid urea-formaldehyde resin was synthesized by us. The ratio of urea to formaldehyde used was 1:1.4. Melamine was added for improving adhesion strength and its amount was 8 wt% of urea. The reaction temperature was 90±1°C and reaction time was about 2.5 h. It had an average viscosity of $3.5\cdot10^{-2}$–$4.5\cdot10^{-2}$ Pa·s, pH between 7.0 and 7.5, 50±1% solid content and <1% free formaldehyde content.

2.2. Sample preparation

A mixture of SF, UFR, and inorganic filler $CaCO_3$, curing agent (NH_4Cl, 3 wt% of resin) and mold release agent (zinc stearate, 1 wt% of the total mixture mass) was prepared, and then put it in an oven for 2 h at 90°C.The blends were taken for composite fabrication available as such. The specimens were produced through compression molding under a pressure of 8 MPa at 140–145°C for 4 min. After that, the composites were post-cured at 120°C for 2 h. The composites containing 30, 40, 50, 60 and 70 wt% SF, contained UFR 50, 40, 30, 20 and 10 wt%, respectively.

2.3. Characterization

Charpy impact strengths of the specimens (120×10×4 mm length, width and depth, respectively) were determined with an impact tester (Chengteh China, Model JC-25 4J) in the flatwise, unnotched mode. The striking velocity was 2.9 m/s and the reported values reflect an average from five measurements.

Three-point bend tests were performed using Shimadzu electronic universal test machine (Model AG-201).The specimens were 120×10×4 mm length, width and depth, respectively. The span of the supports was 60 mm, and the loading speed was 2 mm/min. The reported values reflect an average from five measurements.

Sliding wear tests were conducted on an abrasive wear tester (Yihua China, Model M-2000) at room temperature according to GB3960-83. The diameter of the steel ring (45#steel) was 40 mm, the hardness was 45–50 HRC, and the rotation speed of the steel was 200 rpm during operation. Before the testing, the specimen and the steel ring were washed with acetone and air dried. The size of the wear specimens were 30×7×6 mm length, width and depth, respectively. The tests were performed at a normal load of 200 N and for 40 min. The wear volume loss and friction coefficient were adopted to evaluate wear resistance property. The reported values reflect an average from five measurements.

Water absorption testing of composites has been carried out by taking circular sheet which the diameter was 50 mm and thickness was 4 mm.Samples were first dried by heating in an oven at 50°C for about 24 h, weighed (W_1) and then soaked in distilled water in beakers at room temperature. After

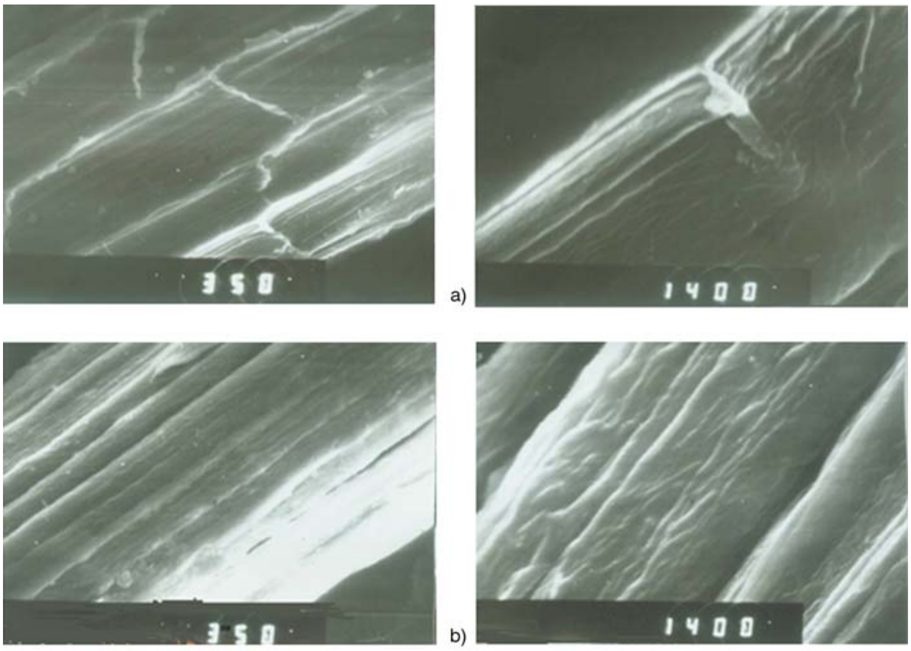

Figure 1. SEM micrographs of (a) untreated SF, (b) alkali-treated SF

24 h, the composite samples were removed from water, dried by a cotton cloth and weighed (W_2). Percentage water absorption of the samples was calculated. The reported values reflect an average from five measurements.

SEM micrographs of SF surfaces and fractured surfaces following impact were taken using a scanning electron microscope (Model JEOL JSM-6380LV). Prior to SEM evaluation, the samples were coated with carbon by sputtering technique. The worn surfaces were observed using the same method.

3. Results and discussion

3.1. SEM examination of treated SF

SEM micrographs of untreated and alkali-treated SF are shown in Figure 1. It can be observed that the untreated SF (a) presents a network structure and includes waxes and other low molar mass impurities. Compared to the (b), it is clear that SF gets thinner after treatment. It is possible that treatment led to micro-fiber fibrillation. The surfaces of the SF (b) become rather smoother as compared to that of untreated SF. In addition, this fibrillation could have increased the effective surface area available for contact with the matrix in the composites, as well as reduced the diameter of sisal fibers, thereby increasing their aspect ratio. This may offer better fiber-matrix interface adhesion and improve stress transfer. These will give rise to improvement in mechanical properties.

3.2. Impact strength

Impact strength is defined as the ability of a material to resist the fracture under stress applied at high speed. The impact properties of composite materials are directly related to its overall toughness. Composite fracture toughness is affected by interlaminar and interfacial strength parameters [18]. Figure 2 shows the variation of Charpy unnotched impact strength of SF/UFR composite with SF loading. The impact strength of composite with 30 wt% SF is 5.78 kJ/m^2.With increase in SF load-

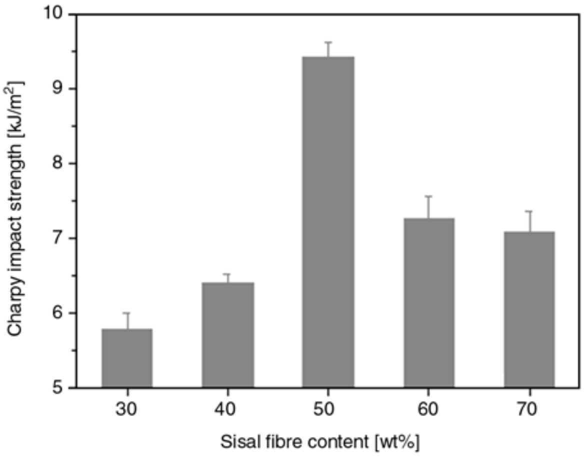

Figure 2. Effects of sisal fibre loading on the impact strength of SF/UFR composites

ing from 30 to 50 wt%, the impact strength increases by 62.98%, namely achieves 9.42 kJ/m^2. With further increase in SF loading (60 wt%), there is a considerable decrease in impact strength. The impact strength of a composite is influenced by many factors including the matrix fracture, fibre-matrix debonding and fibre pull out. It has been reported by van der Oever *et al.* [19] that the Charpy impact strength decreases with enhanced fibre-matrix adhesion. For the composite with 30 wt% SF, the UFR is sufficient and excessive; hence, the interfacial friction stress and chemical bond between matrix and fibre is generally higher when compared to other samples. This is likely to cause a drop in toughness and can explain why the impact strength is much lower. Moreover, the superior strength of composite with 50 wt% may be associated with proper interfacial adhesion between the fibre and matrix; the fibres have reasonable amounts and act as stress transferring medium. In addition, the interspaces and stress concentrations shoot up with the increase of the SF. These fibers could have acted as crack initiation points during impact. Therefore, inferior impact strength is obtained in the composite containing 60 wt% SF.

Figure 3 shows several micrographs of the fractured surface of SF/UFR composite on impact. The images (a) and (b) show the fibres are well anchored in the matrix and a very small amount of fibres are pulled out. The fractured surfaces are smooth and clear. This is observed due to the brittle nature of the matrix. It can be concluded that the fracture mainly happens in the matrix and the performance of fibres is not available. However, in (c) and (d), fiber bundle debonding, deformation in the fiber leading to microcracking and fracture, and fibers splitting are presented. Toughness is significantly enhanced due to the fibres acting as stress transferring medium.

3.3. Flexural property

Results from the bend tests on SF/UFR composite are given in Table 1. It is observed that with decrease of SF content from 70 to 30 wt%, the flexural strength increases sharply i. e. from 15.28 to 58.58 MPa, increasing by about 283.4%. Meanwhile, the flexural modulus increases from 1.59 to 7.63 GPa. As the improved mixing will provide

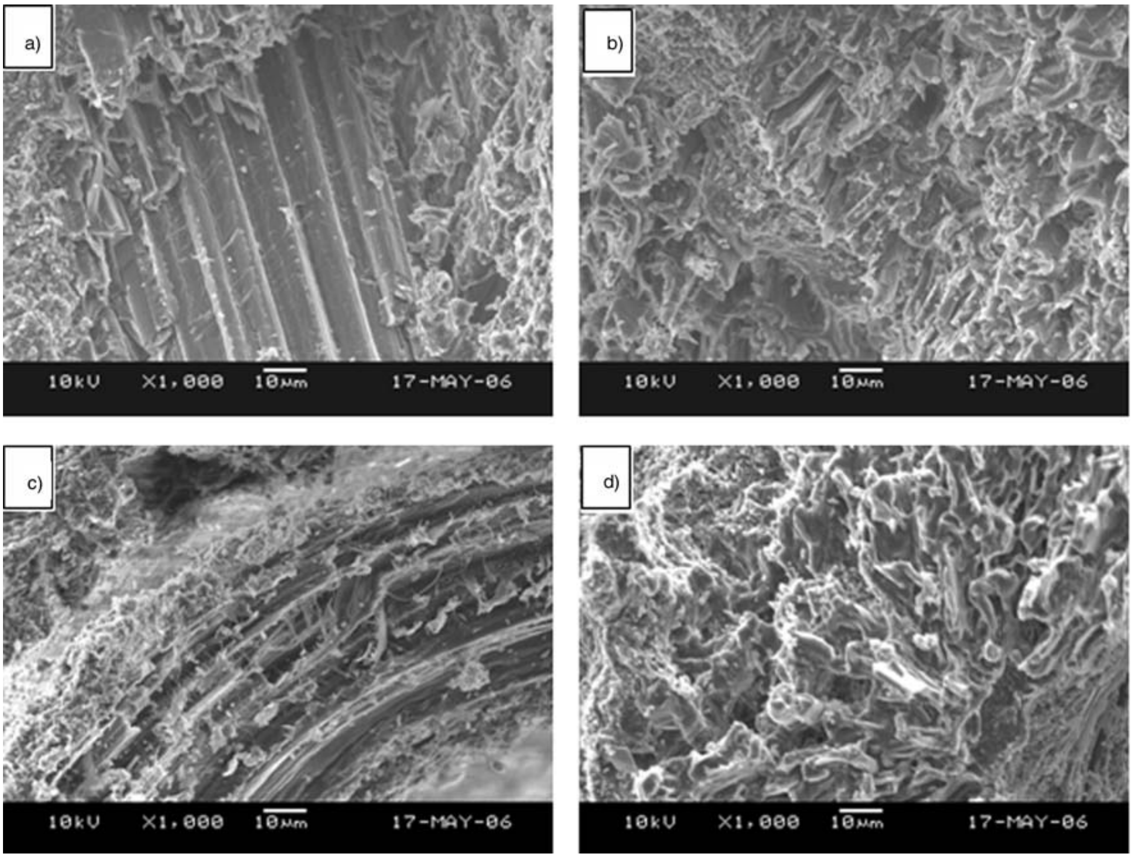

Figure 3. SEM micrograph of Charpy impact fractured surface of SF/UFR composites with (a, b) 30 wt% and (c, d) 50 wt% sisal fibre

Table 1. Effect of sisal fibre loading on the bending property of SF/UF composite

SF content [wt%]	Flexural strength [MPa]	Flexural modulus [GPa]	Density [g/cm³]	Specific strength [MPa·cm³/g]	Specific modulus [GPa·cm³/g]
30	58.58	7.63	1.53	38.29	4.99
40	55.80	5.27	1.52	36.71	3.47
50	53.07	4.93	1.48	35.86	3.33
60	37.73	4.09	1.44	26.20	2.84
70	15.28	1.59	1.22	12.52	1.31

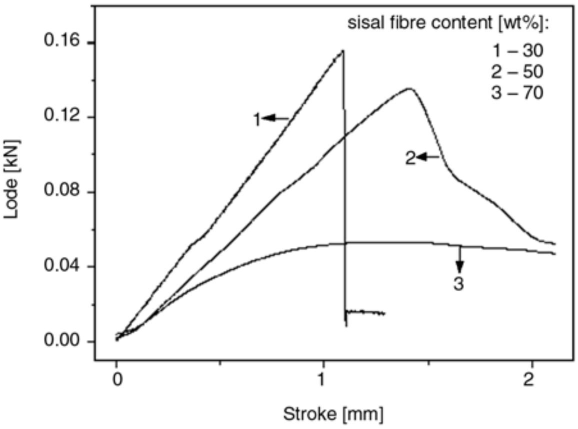

Figure 4. Relationships between lode and stroke as a function of sisal fibre loading

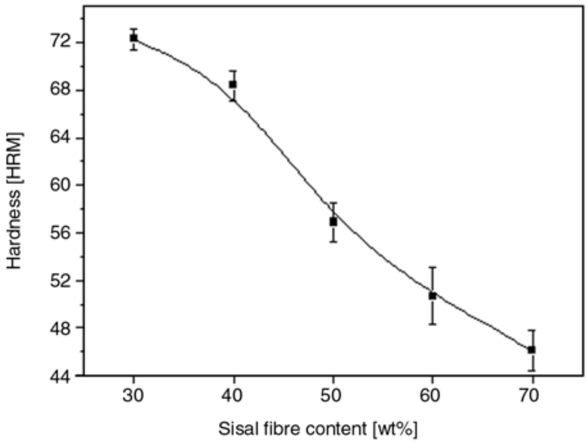

Figure 5. Effects of sisal fibre loading on the hardness of SF/UFR composites

better distribution of sisal, the bridging gaps between the fibres can conduct more effectively.

To obtain qualitative information about the flexural behavior of the composite, the load-stroke traces are taken into consideration. In Figure 4, although the composite with 30 wt% sisal loading yields catastrophically, it bears a higher load than other samples, resulting in a higher flexural strength. In addition, it deforms less until maximum load, which gives a higher flexural modulus. As a consequence, the flexural strength and the flexural modulus of the composites show larger values. Apparently, the stroke of the composite with 50 wt% sisal loading is larger, and this can support the impact results as discussed earlier.

3.4. Wear resistance property

The variation of wear volume loss and friction coefficient with weight fraction of SF for steady-state sliding of SF/UFR composite against the stainless steel ring under dry conditions is shown in Figures 5 and 6. Evidently the wear volume losses and friction coefficients of SF/UFR composite go up with increasing sisal weight fraction. Better performance of the sample with 30 wt% sisal relies heavily on its strong interfaces, and the higher surface hardness nature of the matrix. This indicates that wear of the composite is mostly due to the fibre-matrix adhesion and partly due to the nature of components.

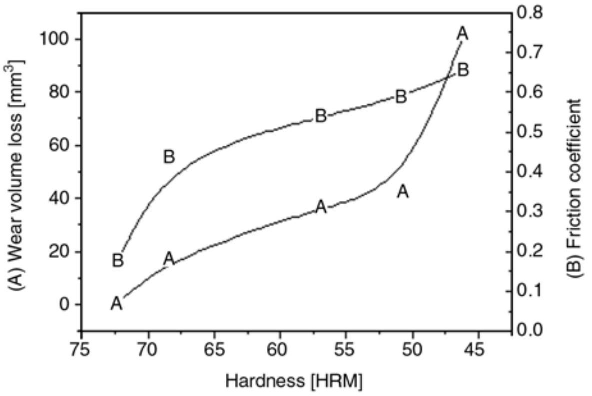

Figure 6. Relationships of the wear volume loss and friction coefficient to the hardness of SF/UFR composites

The surface in Figure 7a is significantly smoother and one can conclude that the inclusion of SF hinders the microcutting, microploughing and deformation of the worn surface. Thus, adhesion and ploughing of the composite are much reduced, leading to a very low wear rate. In addition, the resin may be released from the composite during

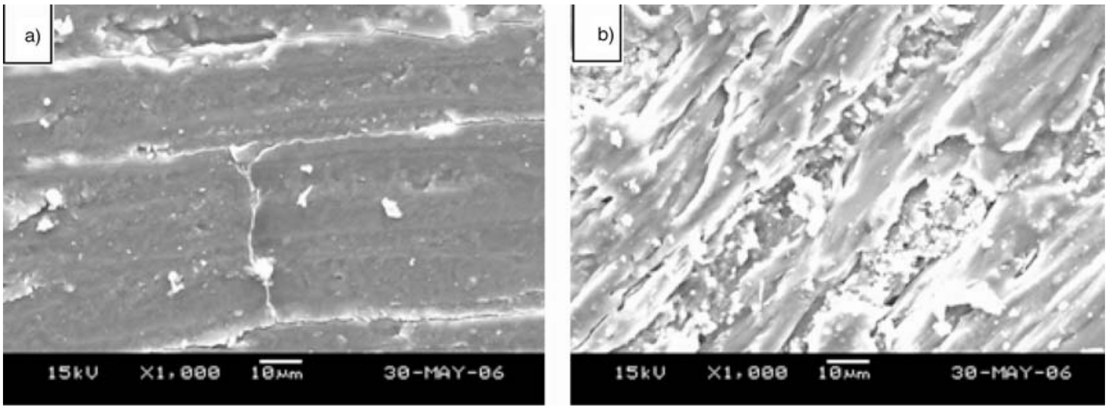

Figure 7. SEM micrograph of worn surface of SF/UFR composites with (a) 30 wt% and (b) 50 wt% sisal fibre

sliding and transfer to the interface between the composite and the steel counter-face. The thin transfer film adhering strongly to the metallic counterpart serves as spacer, preventing the direct contact between the two mating surfaces, thereby slowing the wear rate and reducing the friction coefficient. By contrast, as shown in Figure 7b, the worn surface of composite with 50 wt% SF is quite rough, displaying cracks and microploughing furrows. Fibre and some other components are fractured into fragments and many small filler particles are detached from the composite leaving cavities in the surface. These cavities are themselves stress concentrators and resulted in more cracks and a higher friction coefficient.

3.5. Water absorption property

Figure 8 shows the result of water absorption. We can find out the water absorption of composite with 30 wt% SF is only 0.98 wt% .This can be attributed to the greater adhesion between the fibre and matrix, the low water absorption nature of the matrix. It is observed that with increase of SF content from 30 to 70 wt%, the water absorption rockets. This might be due to the poor distribution of fibres in the composite which result in the formation of fibre lumps. These lumps require more force to deform during hot pressing, and as a result more stresses are built in the composites [20]. When the composites are tested (water absorption test), a greater proportion of these stresses are released, causing a high water absorption. In addition, sisal fibres are lignocellulosics and therefore hydrophilic in nature; sisal absorbs moisture readily.

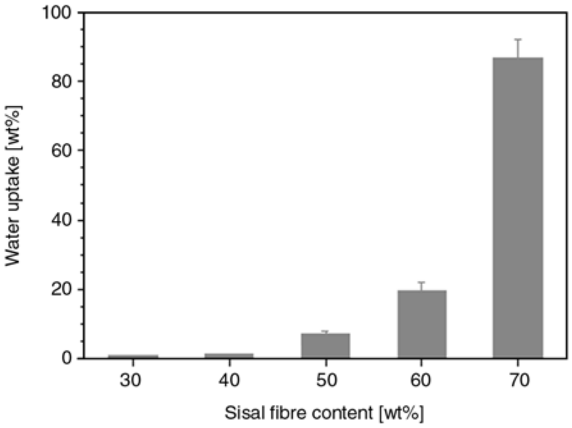

Figure 8. Effects of sisal fibre loading on the water absorption property of SF/UFR composites

4. Conclusions

In this paper, mechanical properties of SF reinforced urea-formaldehyde resin composites have been described. The composite with 50 wt% SF has the optimal Charpy impact strength and it reaches 9.42 kJ/m^2. Whereas the flexural, wear resistance and water absorption properties are proved to be excellent in the composite with 30 wt% SF under the present experimental conditions adopted. The SEM micrographs of impact fractured and worn surfaces reveal that the proper sisal fibre addition can improve the fracture energy, strengthen interfaces and lower wear rate. The composite has significant potential for improving resistance to abrasive wear due to sisal characteristic properties. The fibres themselves possess a higher wear resistance than the matrix and should protrude from the surface after some time. Hence, the applicability of these composites in fibreboard can be expanded.

Acknowledgements

The authors would like to acknowledge the Guangxi Science and Technology Bureau (Grant No.: 05112001-2A3) and Guangxi Natural Science Foundation (No.: 0728223) for financial support.

References

[1] Mohanty A. K., Misra M., Drzal L. T.: Surface modifications of natural fibers and performance of the resulting biocomposites: An overview. Composite Interfaces, **8**, 313–343 (2001).

[2] Joseph K., Thomas S., Paul A.: Effect of surface treatments on the electrical properties of low-density polyethylene composites reinforced with short sisal fibers. Composites Science and Technology, **57**, 67–79 (1997).

[3] Singh B., Gupta M., Verma A.: Polyester moulding compounds of natural fibres and wollastonite. Composites: Part A, **34**, 1035–1043 (2003).

[4] Luyt A. S., Malunka M. E.: Composites of low-density polyethylene and short sisal fibres: the effect of wax addition and peroxide treatment on thermal properties. Thermochimica Acta, **426**, 101–107 (2005).

[5] Kalaprasad G., Joseph K., Thomas S., Pavithran C.: Theoretical modelling of tensile properties of short sisal fibre-reinforced low-density polyethylene composites. Journal of Materials Science, **32**, 4261–4267 (1997).

[6] Pal S., Mukhopadhayay D., Sanyal S., Mukherjea R.: Studies on process variables for natural fibre composites- effect of PEAP as interfacial agent. Journal of Applied Polymer Science, **35**, 973–985 (1988).

[7] Bisanda E. T. N.: The effect of alkali treatment on the adhesion characteristics of sisal fibres. Applied Composite Materials, **7**, 331–339 (2000).

[8] Joseph P. V., Joseph K., Thomas S.: Short sisal fiber reinforced polypropylene composites: the role of interface modification on ultimate properties. Composite Interfaces, **9**, 171–205 (2002).

[9] Fung K. L., Xing X. S., Li R. K. Y., Tjong S. C., Mai Y-W.: An investigation on the processing of sisal fibre reinforced polypropylene composites. Composites Science and Technology, **63**, 1255–1258 (2003).

[10] Wei C., Mu Q-H., Luo W-H.: Influences of treatment methods for sisal stems on properties of sisal fiber/formaldehyde resin composites. China Plastics, **17**, 44–47 (2003).

[11] Niu Y-L., Zhong J-B., Yang X-W., Yu X-B., Wei C.: Effect of sisal fiber contents on wear resistance of sisal fiber/phenol formaldehyde resin in-situ composites. in 'Proceedings of 2005 International Conference on Advanced Fibers and Polymer Materials, Shanghai, China', 411–414 (2005).

[12] Zhong J-B., Niu Y-L., Lü J., Wei C.: Effect of steam explosion treatment on mechanical properties of sisal fiber/phenol-formaldehyde resin composite. China Plastics Industry, **34**, 53–55 (2006).

[13] de Rodriguez N. L. G., Thielemans W., Dufresne A.: Sisal cellulose whiskers reinforced polyvinyl acetate nanocomposites. Cellulose, **13**, 261–270 (2006).

[14] Alvarez V., Vazquez A., Bernal C.: Effect of microstructure on the tensile and fracture properties of sisal fiber/starch-based composites. Journal of Composite Materials, **40**, 21–35 (2006).

[15] Gillah P. R., lrle M. A., Amartey S. A.: Development and production of laboratory scale novel MDF panels from composite and nonwoven mattresses of sisal and wood fibre mixtures. Holz als Roh- und Werkstoff, **58**, 324–330 (2000).

[16] Manikandan Nair K. C., Thomas S., Groeninckx G.: Thermal and dynamic mechanical analysis of polystyrene composites reinforced with short sisal fibres. Composites Science and Technology, **61**, 2519–2529 (2001).

[17] Li Y.: The investigation of fracture properties of sisal textile reinforced polymers. Acta Mechanica Solida Sinica, **17**, 95–103 (2004).

[18] Mishra S., Mohanty A. K., Drzal L. T., Misra M., Parija S., Nayak S. K., Tripathy S. S.: Studies on mechanical performance of biofibre/glass reinforced polyester hybrid composites. Composites Science and Technology, **63**, 1377–1385 (2003).

[19] van den Oever M. J. A., Bos H. L., Molenveld K.: Flax physical fibre structure and its effect on composite properties: impact strength and thermo-mechanical properties. Die Angewandte Makromolekulare Chemie, **272**, 71–76 (1999).

[20] Krzysik A. M., Youngquist J. A., Myers G. E., Chahyadi I. S., Kolosick P. C.: Wood-polymer bonding in extruded and nonwoven web composite panels. in 'Proceedings of Wood Adhesives 1990, Madison, USA', 183–189 (1990).

eXPRESS Polymer Letters Vol.1, No.10 (2007) 688–697
Available online at www.expresspolymlett.com
DOI: 10.3144/expresspolymlett.2007.94

Thermal effects on weld and unweld tensile properties of injection moulded short glass fibre reinforced ABS composites

S. Hashemi[*]

London Metropolitan University, London Metropolitan Polymer Centre, Holloway Road, London N7 8DB, UK

Received 30 May 2007; accepted in revised form 20 August 2007

Abstract. The effect of temperature on weldline properties of injection moulded acrylonitrile butadiene styrene (ABS) reinforced with short glass fibres was investigated in tension between 25 and 100°C. Tensile modulus of both weld and unweld specimens increased linearly with increasing fibre concentration and decreased linearly with increasing temperature. It was found that the presence of weldline had no significant effect upon tensile modulus and this was reflected by weldline integrity factors in the range 0.98 to 0.95. Tensile strength of both weld and unweld tensile specimens increased nonlinearly with increasing fibre concentration and in the case of weldline specimens showed a maximum at fibre concentration of approximately 10% v/v. A linear dependence with respect to volume fraction of fibres was found for specimens without weldline for fibre concentrations in the range 0–10% v/v. The weldline integrity factor for tensile strength decreased significantly with increasing fibre concentration and increased with increasing temperature. The effect of temperature on tensile modulus and strength was satisfactorily modelled using the Kitagawa power law relationship.

Keywords: *polymer composites, weldline, temperature*

1. Introduction

It is well established that the mechanical properties of short fibre polymer composites such as strength and modulus are derived from a combination of the fibre and matrix properties and the ability to transfer stresses across the interface between the two constituents. These properties, however, are affected by a number of parameters, such as the fibre content, fibre length, fibre orientation and the degree of interfacial adhesion between the fibre and the matrix (e.g.: [1–15]). However, as most short fibre composites are fabricated by an injection moulding process, the presence of weldlines is a major design concern as weldlines could lead to a considerable reduction in mechanical properties and because of this designers often need to incorporate liberal safety factors in design analysis to compensate for this weakness.

Weldlines are often observed in injection moulded components due to multigate moulding, existence of pins, inserts, variable wall thickness and jetting and are classified as either being cold or hot. The cold weldlines are formed when two melt fronts meet head on and this type of weld provides the worst-case scenario as far as mechanical properties are concerned. A serious reduction in tensile strength and modulus has been reported for many polymers and their composites in the presence of cold weldlines (e.g.: [1–12]). In general, the presence of a weldline reduces tensile strength by up to 60% and tensile modulus by up to 40% depending on the polymer, the characteristic features of the reinforcing filler and the processing conditions

---

[*] Corresponding author, e-mail: s.hashemi@londonmet.ac.uk

being used. For example, whilst addition of spherical shaped fillers (e.g. glass spheres) has shown to have little effect upon tensile strength of injection moulded thermoplastics with weldlines, addition of cylindrical shaped fillers (e.g. short fibres) has led to a considerable reduction in weldline strength due to the alignment of the fibres parallel to the weldline. The processing conditions such as melt temperature, injection speed and mould temperature could also play an important role in determining the integrity of the welded components and many studies have addressed this issue for both amorphous and semi-crystalline polymers (e.g.:[10, 11, 14])]. However, whilst the majority of weldline studies have been conducted at room temperature, very few have examined the integrity of weldlines at elevated temperatures, particularly in short fibre composite systems [3–5]. To this end, the present work was undertaken to examine the effect of temperature on tensile properties of ABS and its short glass fibre composites in the presence of weldline.

2. Experimental

2.1. Materials

Owens Corning chopped E-glass fibres of initial length and diameter of 4.0 mm and 10 μm, respectively was used as the reinforcing filler for Acrylonitrile Butadiene Styrene (ABS) copolymer received from BAYER. The ABS and the short glass fibres were compounded to produce a series of composites with nominal glass contents of 10, 20 and 30% w/w.

2.2. Compounding

ABS and the short glass fibres were at first dry blended to the desired glass contents of 10, 20 and 30% w/w. After drying in an oven at 80°C for 4 hours the melt compounding of ABS composites was carried out in a counter-rotating twin-screw extruder (Leistritz). The average screw speed was 60 rpm and the die diameter was 4 mm. The extrusion zone temperature ranged from 220–235°C. The extrudates emerging from the die exit were continuously cooled in a water bath and pelletised for injection moulding. Prior to injection moulding, pellets were dried in an oven at 80°C for 4 hours.

2.3. Specimen preparation

The pellets were injection moulded into dumbbell shaped tensile bars using a Negri Bossi NB60 injection-moulding machine using the processing conditions listed in Table 1. The mould used consisted of a single and a double-feed cavity as shown in Figure 1, each 1.7 mm in depth. In the latter a weldline was formed as the two opposing melt fronts met mid-way along the gauge length of the specimen. The dimensions of weldline free specimens (WFS) and weldline specimens (WLS) are depicted in Figure 2.

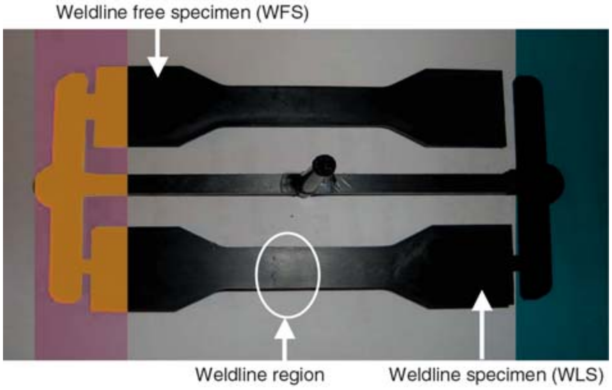

Figure 1. Weldline free (WFS) and unweld tensile specimens

Table 1. Injection moulding conditions for each composite

Processing condition	ABS	Composite with 10% glass fibre	Composite with 20% glass fibre	Composite with 30% glass fibre
Barrel temperature [°C]				
Zone 1	230	230	230	230
Zone 2	230	230	232	232
Zone 3	232	232	235	235
Mould temperature [°C]	70	70	70	70
Injection pressure [MPa]	8.50	8.50	9.00	9.00
Holding pressure [MPa]	3.00	3.00	3.00	3.00
Cooling time [s]	30.00	30.00	30.00	30.00
Cycle time [s]	33.00	33.00	33.00	33.00
Shot weight [g]	27.00	27.00	28.00	29.00

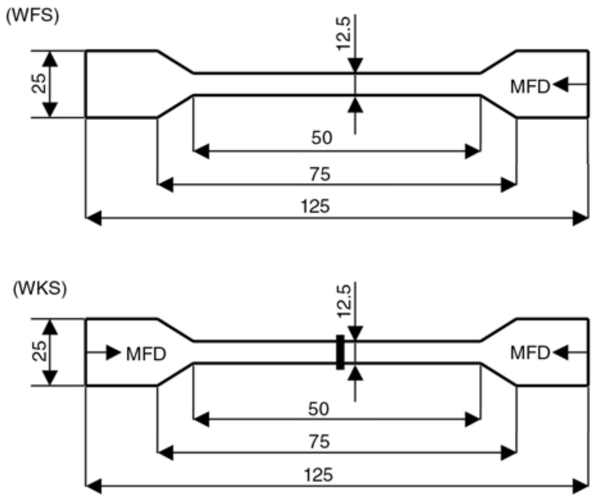

Figure 2. Dimensions of the WFS and WLS in millimetres

2.4. Measurement of fibre length and fibre concentration

Fibre concentration in each composite was determined from the fibre residue remained after ashing weighed samples cut from the gauge length of the moulded bars at 550°C. After cooling, the ash of fibrous material was weighed and the exact weight fraction of fibres (w_f) was determined. The w_f values were subsequently converted into volume fractions (ϕ_f) using the Equation (1):

$$\phi_f = \left[1 + \frac{\rho_f}{\rho_m}\left(\frac{1}{w_f} - 1\right)\right]^{-1} \quad (1)$$

Taking the density of the matrix (ρ_m) as 1.12 kgm^{-3} and density of the fibre (ρ_f) as 2.54 kgm^{-3} gave fibre concentration values of 4.4, 9.5 and 15.5% v/v. It must be pointed out that the void content in moulded specimens was not measured in this study. The residue from the ash tests were subsequently spread on a glass slide and placed on the observation stage of a microscope. Magnified fibre images were transmitted to a large screen, and the fibre images were then automatically digitised by software with a computer. From the fibre length distributions, the average fibre length values ($\overline{L_f}$) of 110, 94 and 83 μm were obtained for 4.4, 9.5 and 15.5% v/v composites, respectively. Results show decrease in $\overline{L_f}$ with increasing ϕ_f thus indicating that the average length of the fibre in the moulded specimens was affected by the concentration level of the fibres. The increased damage to fibre length with increasing ϕ_f was attributed to a greater degree of fibre-fibre interaction and increased in melt viscosity at higher fibre loadings. The latter give rise to higher bending forces on the fibres during compounding and moulding process causing the fibres to break, as noted here.

2.5. Mechanical testing

Dumbbell specimens with weldline (WLS) and without weldline (WFS) were tested in tension in an Instron testing machine using pneumatic clamps. Tensile tests were performed at 25, 60 and 100°C at a constant crosshead displacement rate of 50 mm/min. For each composite at least six specimens with weldline and six without weldline were tested at a given temperature. The load-displacement curve for each specimen was recorded using a computer data logger from which tensile modulus and strength were calculated using the initial slope and the load at maximum, respectively. The modulus values reported in this study are based on the displacement of the crosshead.

3. Results and discussion

3.1. Tensile modulus

3.1.1. Effect of fibre concentration

The load-displacement curves obtained indicated that the tensile behaviour of ABS and its composites during the early stages is linearly elastic. Figure 3 shows that composite modulus (E_c) calculated using the initial slope of the load-displacement curves increases with increasing ϕ_f. As illustrated in Figure 3, variation of E_c with ϕ_f is extremely linear at all three temperatures. The linear dependence

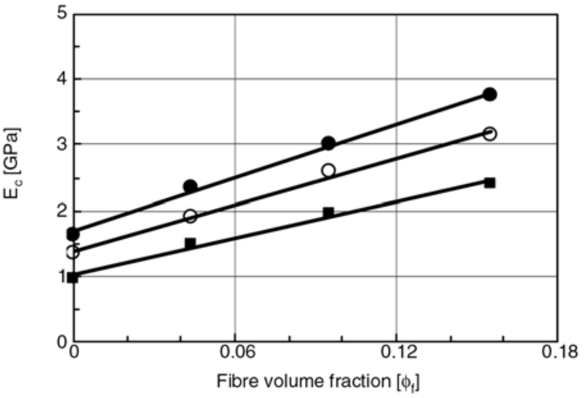

Figure 3. Effect of fibre volume fraction on tensile modulus of weldline free specimens (WFS) at 25 (•), 40 (o) and 100°C (■)

Table 2.. Fibre efficiency parameters for composite modulus as a function of fibre volume fraction at 25, 60 and 100°C

ϕ_f	η_E			η_L			η_0		
	25°C	60°C	100°C	25°C	60°C	100°C	25°C	60°C	100°C
0.044	0.200	0.173	0.133	0.296	0.261	0.199	0.675	0.663	0.667
0.095	0.200	0.173	0.133	0.296	.0260	0.199	0.677	0.664	0.669
0.155	0.200	0.173	0.133	0.294	0.259	0.197	0.681	0.669	0.674

between E_c and ϕ_f follows the modified 'rule-of-mixtures' given by Equation (2):

$$E_c = E_m + (\eta_E E_f - E_m)\,\phi_f \tag{2}$$

where E_m is the modulus of the matrix and E_f is the modulus of the fibre whose value in this study was taken as 76 GPa and temperature independent. The parameter η_E is termed the overall fibre efficiency for composite modulus whose value depends on the length and the orientation of the fibres in the moulded specimens. The value of η_E was determined from the slope of the line E_c versus ϕ_f in Figure 3 using Equation (2). Values obtained are given in Table 2 where it can be seen that η_E decreases with increasing temperature.

The overall efficiency parameter η_E is the product of two efficiency parameters; one associated with the orientation of the fibres (η_0) and the other with the shortness of the fibre (η_L). The parameter η_L was evaluated using the Cox shear lag model [16] which gives η_L by Equation (3):

$$\eta_L = 1 - \frac{\tanh\beta}{\beta} \tag{3}$$

where β is defined by Equation (4):

$$\beta = \frac{\overline{L}_f}{2}\left(\frac{4E_m}{E_f d^2 \ln\lambda}\right)^{\frac{1}{2}} \tag{4}$$

where d is the diameter of the fibres. If packing arrangement of fibres is assumed square, then λ can be obtained from Equation (5):

$$\lambda = \sqrt{\frac{\pi}{4\phi_f}} \tag{5}$$

Values of η_L obtained are given in Table 2 where it can be seen that whilst η_L is not affected by the concentration of the fibres, it decreases with increasing temperature. Also given in the table are values of η_0 obtained from the ratio η_E/η_L. The η_0 values range between 0.663 and 0.681 which are in the same range as 0.67–0.72 reported for some polymer composite systems [2–4, 8, 9]. Using the Krenchel [17] definition of η_0 which is given by Equation (6) and assuming a perfect alignment of fibres (i. e. $a_n = 1$), one obtains fibre orientation angle, θ of approximately 25 to 26° with respect to loading direction.

$$\eta_0 = \sum_{i=1}^{i=n} a_n \cos^4\theta_n \tag{6}$$

3.1.2. Effect of temperature

Temperature dependence of E_c is shown in Figure 4 where it can be seen that in the present temperature range, E_c decreases linearly with increasing temperature at a rate which is dependent upon the concentration of fibres in the composite. Evidently, as ϕ_f increases so does the rate at which E_c decreases with increasing temperature. The linear dependence between modulus and temperature can be expressed by Equation (7):

$$E(T) = E_0 - \kappa T \tag{7}$$

where E_0 and κ are constants whose values at a given temperature increased with increasing ϕ_f.

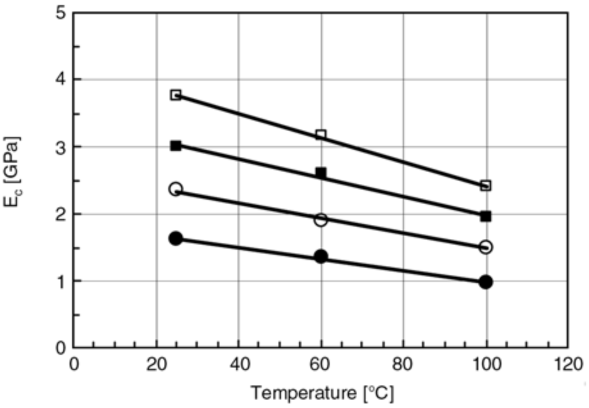

Figure 4. Effect of temperature on tensile modulus of weldline free specimens (WFS) with fibre concentration values (v/v) of 0% (•), 4.4% (o), 9.5% (■) and 15.5% (□)

3.1.3. Effect of weldline

It was noted that the initial slope of the load-displacement curves was marginally affected by the weldline. As shown in Figure 5, modulus of the weldline specimens (E_{cw}) like weld free specimens (E_c) increased linearly with increasing ϕ_f. Using the slopes, η_E values of 0.194, 0.168 and 0.137 were obtained at 25, 60 and 100°C, respectively. Comparing the η_E values for the two specimen types it may be said that η_E is not affected by the presence of the weldline. The modulus retention ratio or the weldline integrity parameter as it is commonly known (the ratio of the modulus of a specimen with a weldline to that of a specimen without a weldline) ranged between 0.98 and 0.95 and showed no systematic variation with respect to either temperature or fibre volume fraction of fibres.

It has been shown [4] that the modulus of a specimen with weldline (E_{cw}) may be represented by the relationship given by Equation (8):

$$E_{cw} = \frac{E_c E_w}{E_w - (E_w - E_c)z} \tag{8}$$

where E_w is modulus of the material inside the weldline, E_c modulus of the material outside the weldline and z is a dimensionless parameter whose value depends on the ratio L_w/L_0 where L_w is width of the weldline and L_0 is the length of the specimen. Previous studies [1–4] using the same mould geometry indicated that whilst fibres inside the weldline region are predominantly aligned with their long axis parallel to the weldline (i. e. perpendicular to the mould-fill direction and the direction of the applied tensile stress), outside the weldline region they are predominantly aligned in the same direction as in the weldline free specimens. The off-axis alignment of fibres outside the weldline region and the transverse alignment of fibres inside the weldline region, implies that $E_c >> E_w$. Also, since the width of the weldline region, L_w was typically less than 1 mm and therefore much smaller than the overall length of the specimen (L_0), the ratio z becomes very small and therefore the second term in denominator of Equation (8) becomes small compared to E_w, thus indicating that $E_{cw} \approx E_c$, i. e., weldline has little effect on tensile modulus as observed in this study.

As for the variation of E_{cw}, with temperature, a linear trend as in Figure 5 was noted with no significant variation in the slopes due to weldline.

3.2. Tensile strength

3.2.1. Effect of fibre concentration

The effect of fibre volume fraction on tensile strength of weldline free specimens (WFS) is shown in Figure 6. Evidently, in the absence of weldline, tensile strength increases with increasing fibre concentration with a tendency to level off or reaching a maximum on approaching fibre concentration value of approximately 16% v/v. The levelling off effect (or reaching a maximum) which is also noted in several other injection moulded glass reinforced polymer systems [3, 4, 8, 9] is mainly attributed to the separation distance between the fibres becoming sufficiently small so that the flow of the matrix material between fibres is severely restricted. This effect and the higher stress concentration in the matrix due to the greater number of

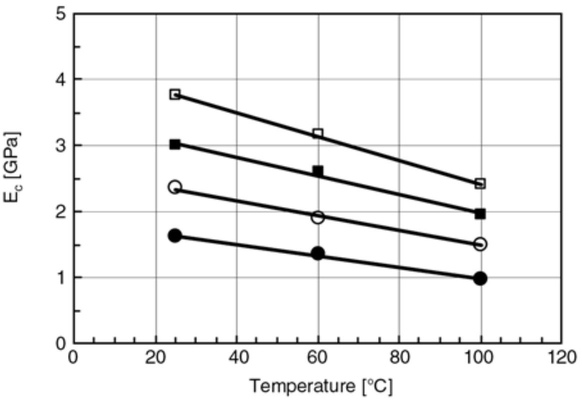

Figure 5. Effect of fibre volume fraction on tensile modulus of weldline specimens (WLS) at 25 (•), 40 (o) and 100°C (■)

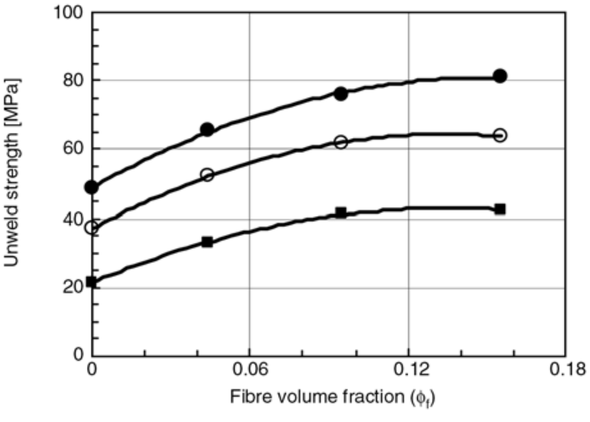

Figure 6. Effect of fibre volume fraction on tensile strength of weldline free specimens (WFS) at 25 (•), 40 (o) and 100°C (■)

Table 3. Curve fitting parameters for composite strength as a function of fibre volume fraction at 25, 60, and 100°C for both WFS and WLS specimens

T [°C]	WFS			WLS		
	a_0	a_1	a_2	a_0	a_1	a_2
25	49.01	422.68	–1401.6	44.48	88.81	–593.39
60	37.03	408.33	–1524.2	34.10	164.92	–946.20
100	21.44	318.46	–1176.1	20.03	171.48	–858.80

fibre ends at high ϕ_f, reduces the gain in strength which one would expect otherwise.

The nonlinear relationship seen in Figure 6 between tensile strength, σ_c and the fibre volume fraction, ϕ_f can be described by a polynomial function given by Equation (9):

$$\sigma_c = a_0 + a_1\phi_f + a_2\phi_f^2 \tag{9}$$

where a_0, a_1 and a_2 are the curve fitting parameters whose values at the three test temperatures are given in Table 3. However, as illustrated in Figure 7, tensile strength for fibre concentration values in the range 0 to 10% v/v, can be reasonably assumed to increases linearly with ϕ_f (regression coefficients are in the range 0.96 to 0.98). The simplest model that may be used to predict a linear dependence between σ_c and ϕ_f in short fibre composites is that of the 'modified rule-of-mixtures' which when rearranged can be expressed by Equation (10):

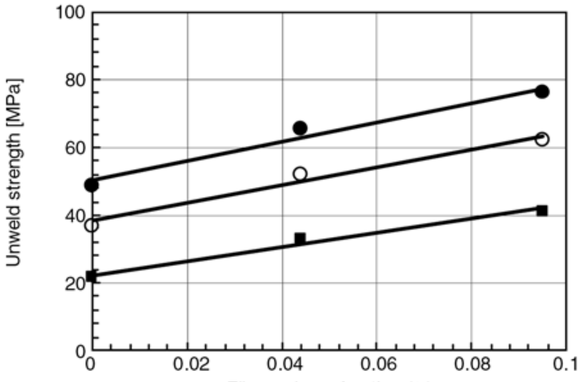

Figure 7. Effect of fibre volume fraction on tensile strength of weldline free specimens (WFS) with fibre concentration values in the range 0–9.5% v/v at 25 (•), 40 (o) and 100°C (■)

$$\sigma_c = \sigma_m + (\eta_\sigma\sigma_f - \sigma_m)\,\phi_f \tag{10}$$

where σ_f is the tensile strength of the fibre taken in this study as 2470 MPa, σ_m is the tensile strength of the matrix and η_σ is the overall fibre efficiency parameter for the composite strength taking into account the effects due to fibre length and orientation in the composite.

Using Equation (10) and the slope of the lines in Figure 7, η_σ values were evaluated. It can be seen from Table 4 that η_σ values are considerably smaller than η_E and likewise decrease with increasing temperature.

The overall efficiency parameter η_σ like η_E is the product of two efficiency parameters as given by Equation (11):

$$\eta_\sigma = \eta_L\eta_0 \tag{11}$$

where η_L is the fibre length and η_0 is the fibre orientation efficiency parameters for the composite strength. Using the η_0 values obtained via the modulus (see Table 2), values of η_L for composite strength was evaluated as a function of temperature using Equation (11). It can be seen from Table 4 that η_L for composite strength like for composite modulus decreases with increasing temperature.

Using the tabulated values of η_L given in Table 4 and the average fibre lengths, the critical fibre lengths, L_c was calculated for each composite as a function of temperature using the Kelly-Tyson relationship given by Equation (12) [18]:

$$L_c = \frac{\overline{L}_f}{2\eta_L} \tag{12}$$

Table 4. Fibre efficiency parameters for composite strength as a function of fibre volume fraction at 25, 60, and 100°C

ϕ_f	η_σ			η_0			η_L		
	25°C	60°C	100°C	25°C	60°C	100°C	25°C	60°C	100°C
0.044	0.136	0.121	0.093	0.675	0.663	0.667	0.201	0.183	0.139
0.095	0.136	0.121	0.093	0.677	0.664	0.669	0.201	0.182	0.139
0.155	0.136	0.121	0.093	0.681	0.669	0.674	0.200	0.181	0.138

Table 5. Fibre critical length as a function of fibre volume fraction at 25, 60 and 100°C

ϕ_f	L_f	η_L			L_c [μm]		
		25°C	**60°C**	**100°C**	**25°C**	**60°C**	**100°C**
0.044	110	0.201	0.183	0.139	274	301	396
0.095	94	0.201	0.182	0.139	234	258	338
0.155	83	0.200	0.181	0.138	208	229	301

Results obtained from this analysis are presented in Table 5 where it can be seen that L_c increases with temperature but decreases with increasing ϕ_f mainly due to the reduction in $\bar{L}_f$ with increasing ϕ_f. It can be said that η_σ is considerably smaller than η_E simply because whilst η_E depends on the average length of the fibres, η_σ depends on both the average length as well as the critical fibre length which is lower.

3.2.2. Effect of temperature

The effect of temperature on the tensile strength of weldline free specimens is shown more explicitly in Figure 8 where it can be seen that it decreases with temperature in a linear manner. The effect of increasing ϕ_f is simply an upward vertical shift in tensile strength-temperature curve. It is also evident that tensile strength decreases with increasing temperature at a faster rate as fibre concentration is increased. The effect of temperature on tensile strength may be expressed by Equation (13):

$$\sigma(T) = \sigma_0 - \lambda T \tag{13}$$

where values of σ_0 and λ are both dependent upon ϕ_f.

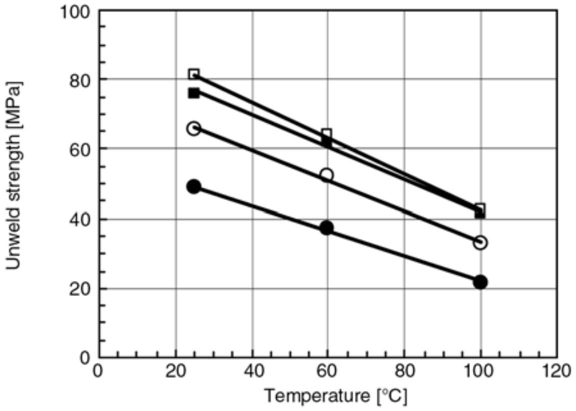

Figure 8. Effect of temperature on tensile strength of weldline free specimens (WFS) with concentration values (v/v) of 0% (•), 4.4% (o), 9.5% (■) and 15.5% (□)

3.2.3. Effect of weldline

Failure of the weldline specimens (WLS) was always at the weldline as shown in Figure 9. Figure 10 shows the effect of weldline strength (σ_{cw}) as a function of fibre volume fraction, ϕ_f at the three temperatures selected in this study. It can be seen that σ_{cw} increases initially and reaches a maximum at fibre concentration value of approximately 10% v/v before decreasing. As illustrated in Fig-

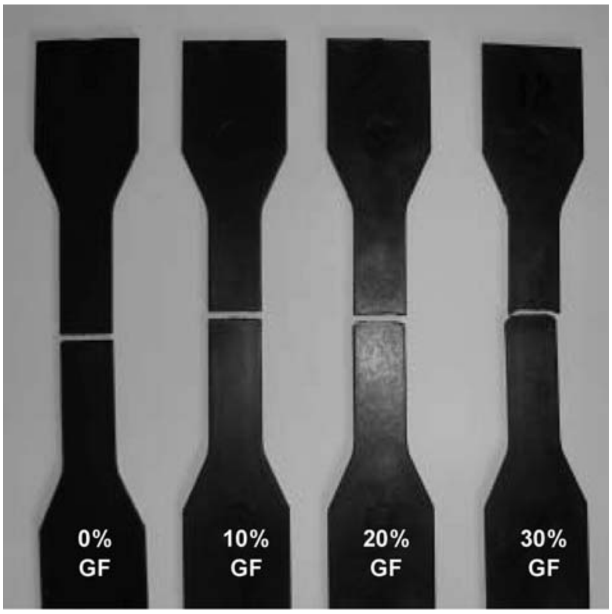

Figure 9. The broken weldline specimens (WLS) at 25°C

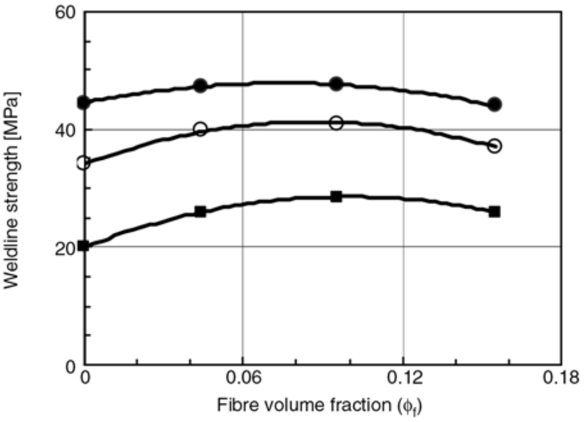

Figure 10. Effect of fibre volume fraction on tensile strength of weldline specimens (WLS) at 25 (•), 40 (o), and 100°C (■)

ure 10, variation of σ_{cw} with ϕ_f like σ_c can also be expressed by Equation (14):

$$\sigma_{cw} = a_0 + a_1\phi_f + a_2\phi_f^2 \tag{14}$$

The values of a_0, a_1 and a_2 can also be found in Table 3. Using Equation (14) one can easily calculate weldline strength of the ABS composites for any fibre concentration value between 0 and 16% v/v.

The effect of weldline on tensile strength was quantitatively expressed in terms of weldline integrity factor, F_σ defined by Equation (15):

$$F_\sigma = \frac{\text{Tensile strength of specimen with weldline}}{\text{Tensile strength of specimen without weldline}} \tag{15}$$

Figures 11 and 12 show the variations of F_σ with ϕ_f and temperature, respectively. It can be seen that F_σ decreases with increasing ϕ_f but increases with increasing temperature. The observed reduction in tensile strength in the presence of weldline is attributed mainly to the reduction in the fraction of fibres crossing the weldline region, particularly at high concentration values of glass fibres. As a result, the material within the weldline region acted as if it was not reinforced. It is also evident from Figure 12 that F_σ increases with temperature in a linear manner. As reflected by slope of the lines, F_σ for composites shows greater temperature dependence than for the matrix. It is interesting to note that slope of F_σ–T lines for the three composites shows no significant variation with respect to ϕ_f, meaning the rate at which F_σ increases with temperature is not sensitive to ϕ_f. It can be said, that the effect of ϕ_f is merely a downward vertical shift in the F_σ–T line.

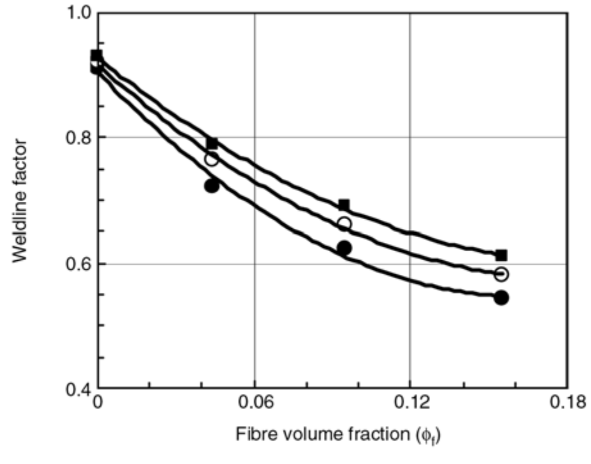

Figure 11. Effect of fibre volume fraction on weldline factor for tensile strength at 25 (•), 40 (o) and 100°C (■)

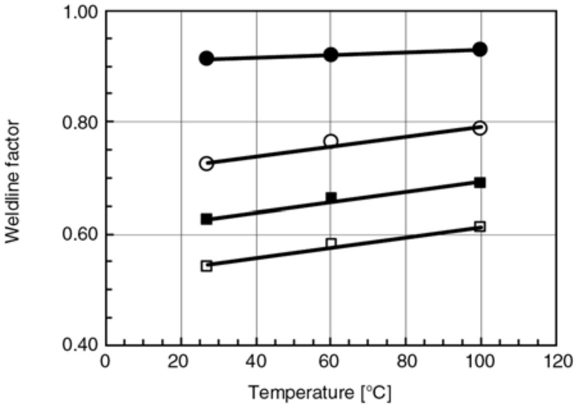

Figure 12. Effect of temperature on weldline factor for tensile strength with fibre concentration values (v/v) of 0% (•), 4.4% (o), 9.5% (■) and 15.5% (□)

3.3. Tensile strength and modulus

The effect of temperature on tensile strength and modulus was analysed further using the general form of the relationship between shear stress, τ and shear modulus, G as proposed by Kitagawa [19]. Kitagawa proposed a power law relation of the form given by Equation (16):

$$\frac{T_0\tau}{T\tau_0} = \left(\frac{T_0 G}{T G_0}\right)^n \tag{16}$$

where τ_0 and G_0 are the values of shear stress and shear modulus at some reference temperature T_0, respectively and n is a temperature independent exponent. The shear properties G and τ in Equation (16) were converted into tensile properties E and σ using Equation (17):

$$\frac{\tau}{\tau_0} = \frac{\sigma}{\sigma_0} = \frac{E}{E_0} = \frac{G}{G_0} \tag{17}$$

Substituting Equation (17) into Equation (16) and rearranging gives Equation (18):

$$\ln\left(\frac{\sigma}{T}\right) = \ln\left[\left(\frac{T_0}{E_0}\right)^n\left(\frac{\sigma_0}{T_0}\right)\right] + n\ln\left(\frac{E}{T}\right) \tag{18}$$

According to Equation (18) log-log plot of (σ/T) versus (E/T) should produce a straight line with the

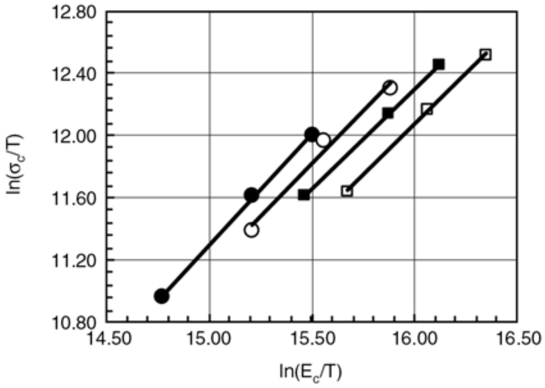

Figure 13. ln(σ_c/T) versus ln(E_c/T) according to Equation (20) for weldline free specimens (WFS) with fibre concentration values (v/v) of 0% (●), 4.4% (o), 9.5% (■) and 15.5% (□)

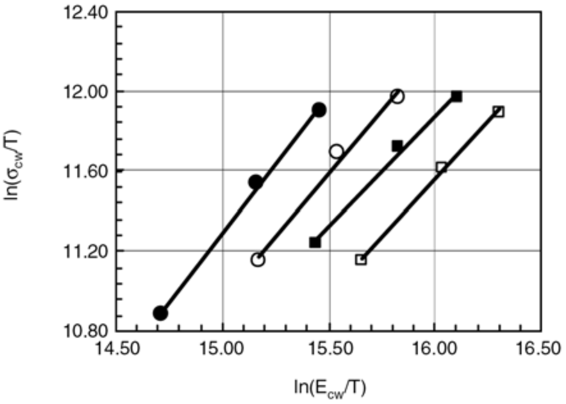

Figure 14. ln(σ_{cw}/T) versus ln(E_{cw}/T) according to Equation (20) for weldline specimens (WLS) with fibre concentration values (v/v) of 0% (●), 4.4% (o), 9.5% (■) and 15.5% (□)

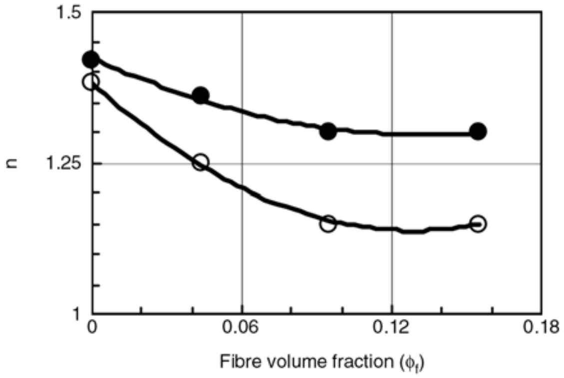

Figure 15. Exponent n versus volume fraction of fibres for WFS (●) and WLS (o)

slope of n. Figures 13 and 14 show log-log plots according to Equation (18) for both unweld and weld data respectively for the range of ϕ_f values studied in this work. It is found that weld and unweld data for the matrix and its composites follow Equation (18) remarkably well with regression coefficients of 0.996 or better. The values of n obtained from the slope of the lines are plotted in Figure 15 as a function of ϕ_f where it can be seen that for the composite system studied here, exponent n deceases with increasing ϕ_f for both weld and unweld specimens with unweld specimens exhibiting higher n particularly for the three composites.

4. Conclusions

The effect of temperature (between 25 and 100°C), fibre concentration (between 0 and 15.5% v/v) and weldline on tensile strength and modulus of ABS reinforced with short glass fibres was investigated. The following observations were made:

- Tensile modulus increased linearly with increasing ϕ_f and decreased linearly with increasing temperature. The linear dependence between tensile modulus and ϕ_f obeyed modified rule of mixtures.
- Presence of weldline had no significant effect on tensile modulus. Weldline integrity factor was in the range 0.98 to 0.95.
- Tensile strength of weldline free specimens increased with increasing ϕ_f in a nonlinear manner but decreased with temperature in a linear manner. For fibre concentration values in the range 0–10% v/v, variation of tensile strength with ϕ_f was reasonably linear and obeyed the modified rule of mixtures for strengths.
- Weldline strength increased with increasing ϕ_f in a nonlinear manner reaching a maximum at fibre concentration of about 10% v/v.
- Weldline factor for strength decreased with increasing ϕ_f but increased linearly with increasing temperature.
- The fibre efficiency parameters for composite strength and modulus decreased with increasing temperature. The efficiency parameter for composite strength was greater than for composite modulus.
- The effect of temperature on tensile modulus and strength for both WFS and WLS was satisfactorily modelled using the *Kitagawa* power law relationship. The power law exponent was affected by the fibre concentration and its value for WFS was higher than for WLS.

References

[1] Chrysostomou A., Hashemi S.: Mechanical properties of injection-moulded styrene maleic anhydride (SMA). Part II: Influence of short glass fibres and weldlines. Journal of Materials Science, **33**, 4491–4501 (1998).

[2] Nabi Z. U., Hashemi S.: Influence of short glass fibres and weldlines on the mechanical properties of injection-moulded acrylonitrile-styrene-acrylate copolymer. Journal of Materials Science, **33**, 2985–3000 (1998).

[3] Hashemi S.: Influence of temperature on weldline strength of injection moulded short glass fibre styrene maleic anhydride polymer composites. Plastics, Rubber and Composites, **31**, 1–7 (2002).

[4] Hashemi S., Lepessova Y.: Temperature and weldline effect on tensile properties of injection moulded short glass fibre PC/ABS polymer composite. Journal of Materials Science, **42**, 2652–2662 (2007).

[5] Necar M., Irfan-ul-Haq M., Khan Z.: Temperature and weld-line effects on mechanical properties of CPVC. Journal of Materials Processing Technology, **142**, 247–255 (2003).

[6] Fu S. Y., Lauke B., Mader E., Yue C. Y., Hu X.: Tensile properties of short-glass-fiber- and short-carbon-fiber-reinforced polypropylene composites. Composites, Part A, **31**, 1117–1125 (2000).

[7] Fisa B.: Mechanical degradation of glass fibres during compounding with polypropylene. Polymer Composites, **6**, 232–341 (1985).

[8] Thomason J. L.: Micromechanical parameters from macromechanical measurements on glass reinforced polypropylene. Composites Science and Technology, **62**, 1455–1468 (2002).

[9] Thomason J. L.: Micromechanical parameters from macromechanical measurements on glass reinforced polyamide 6,6. Composites Science and Technology, **61**, 2007–2016 (2001).

[10] Debondue E., Fournier J-E., Lacrampe M-F., Krawczak P.: Wedlines in injection-molded reinforced thermoplastics: Mechanical performance improvement through intrusion induced fibre reorientation. Polymer and Polymer Composites, **12**, 373–381 (2004).

[11] Sanschagrin B., Gauvin R., Fisa B., Vu-Khanh T.: Weldlines in injection moulded polypropylene: Effect of filler shape. Journal of Reinforced Plastics and Composites, **9**, 194–208 (1990).

[12] Meddad A., Fisa B.: Weldline strength in glass fiber reinforced polyamide 66. Polymer Engineering and Science, **35**, 893–901 (1995).

[13] Akay M., Barkley D.: Flow-aberrations and weld lines in glass-fibre reinforced thermoplastics injection mouldings. Plastics, Rubber and Composites Processing and Applications, **20**, 137–149 (1993).

[14] Nadkarni V. M., Ayodhya S. R.: The influence of knitlines on the tensile properties of fibreglass reinforced thermoplastics. Polymer Engineering and Science, **33**, 358–367 (1993).

[15] Fisa B., Rahmani M.: Weldline strength in injection molded glass fibre-reinforced polypropylene. Polymer Engineering and Science, **31**, 1330–1336 (1991).

[16] Cox H. L.: The elasticity of strength of paper and other fibrous materials. British Journal of Applied Physics, **3**, 72–79 (1952).

[17] Krenchel H.: Fibre reinforcement. Akademisk Forlag, Copenhagen (1964).

[18] Kelly A., Tyson W. R.: Tensile properties of fibre reinforced metals. Journal of the Mechanics and Physics of Solids, **13**, 329–350, (1965).

[19] Kitagawa M.: Power law relationship between yield stress and shear modulus for glassy polymers. Journal of Polymer Science: Polymer Physics Edition, **15**, 1601–1611 (1977).

eXPRESS Polymer Letters Vol.1, No.10 (2007) 698–703
Available online at www.expresspolymlett.com
DOI: 10.3144/expresspolymlett.2007.95

Synthesis, characterization and thermal properties of inorganic-organic hybrid

*Z .L. Da, Q. Q. Zhang, D. M. Wu, D. Y. Yang, F. X. Qiu**

School of Chemistry and Chemical Engineering, Jiangsu University, Zhenjiang 212013, China

Received 7 July 2007; accepted in revised form 20 August 2007

Abstract. Poly (St-MAn-APTES)/silica hybrid materials were successfully prepared from styrene (St), maleic anhydride (MAn) and tetraethoxysilane (TEOS) in the presence of a coupling agent 3-aminopropyltriethoxysilane (APTES), by free-radical solution polymerization and in situ sol-gel process. The TEOS content varied from 0 to 25 wt%. Fourier transform infrared spectroscopy and ^{29}Si nuclear magnetic resonance spectroscopy were used to characterize the structure of the hybrids (condensed siloxane bonds designated as Q^1, Q^2, Q^3, Q^4, with 3-aminopropyltriethoxysilane having mono-, di-, tri, tetra-substituted siloxane bonds designated as T^1, T^2 and T^3). The results revealed that Q^3, Q^4 and T^3 were the major microstructure elements in forming a network structure. The hybrid materials were also characterized by the methods of solvent extraction, Transmission Electron Microscopy (TEM), differential scanning calorimetry (DSC) and thermogravimetric analysis (TGA) for determining the gel contents, particle size and thermal performance. The results showed that gel contents in the hybrid materials were much higher, the SiO_2 phase were well dispersed in the polymer matrix, silicon dioxide existed at nanoscale in the composites, which had excellent thermal stability.

Keywords: *polymer composites, organic-inorganic hybrid material, sol-gel process*

1. Introduction

Over the past decade, the synthesis and characterization of inorganic-organic hybrid materials by the sol-gel process have received considerable attention. This is mainly due to the mild conditions, such as low temperature and pressure[1–3]. In addition, the sol-gel process is a convenient method for preparing oxide films from alkoxysilyl group containing materials via continuous reaction steps of hydrolysis and condensation. This technology has been a great achievement in making ceramic or organic modified hybrid materials in the past two decades, by which homogeneous materials with higher thermal stability, density, and hardness can be produced. These hybrid materials posses organic and inorganic properties [4] which can also be tuned through changing the functionality or segment size of each component, tayloring thermal, mechanical, electronic, optical and optoelectronic properties. Common applications of the hybrid materials as passive or active layer in optoelectronic devices have been reported, including protective coating [5], contact lenses [6], high refractive index films [7], thin film transistors [8], solar cells [9], light-emitting diodes [10], optical waveguides materials [11] and photo chromic materials [12]. These properties are associated with σ conjugation [13]. Many researchers have demonstrated that monolithic, transparent hybrid materials without macroscopic phase separation can be prepared by properly controlling the conditions of hydrolysis and condensation of sol-gel materials such as tetraethoxysilane (TEOS) or tetramethoxysilane (TMOS) [14–16]. Organic and inorganic constituents can be chemically bonded or just physi-

---

*Corresponding author, e-mail: fxqiuchem@163.com

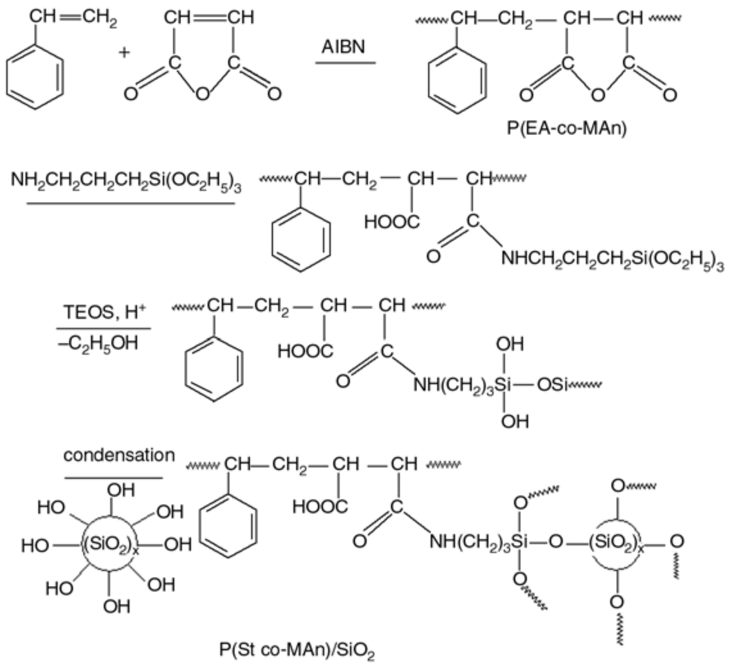

Figure 1. Preparation of organic-inorganic hybrid by sol-gel process

cally mixed in these hybrid materials. A significant feature to enhance the compatibility in the hybrid material, however, is the formation of covalent bonding between organic polymers and inorganic components.

In this study, copolymer was prepared by free radical copolymerization of styrene (St) with maleic anhydride (MAn). Copolymer precursor holding trimethoxysily-functionality was prepared by 3-aminopropyltriethoxysilane (APTES), coupling of the copolymer with miscible TEOS as an inorganic silica matrix for a sol-gel process. Then the copolymer precursor was hydrolyzed and condensed in the presence of an aqueous HCl catalyst to generate poly (St-MAn-APTES)-SiO_2 hybrid material as shown in Figure 1.

2. Experimental

2.1 Materials

Styrene (St), maleic anhydride (MAn), 2,2’-azobisisobutyronitrile(AIBN) and TEOS were purchased from Shanghai Chemical Reagent Company. Initiating agent AIBN was purified by recrystalization from alcohol and then dried in a vacuum oven. APTES was purchased from Nanjing Shuguang Chemical Plant. Tetrahydrofuran (THF) was purified by distillation and other reagents , solvents were obtained commercially and were used as received.

2.2. Preparation of hybrid P (St-MAn-APTES)/SiO_2

Hybrid was prepared according to the scheme, as shown in Table 1. St and MAn were taken in a 500 ml three-neck round-bottomed flask. The THF and initiator AIBN were added under nitrogen purging. The reaction temperature was maintained at 70°C for 3 h and the copolymerization was carried out. Then APTES was added under nitrogen and stirred for 2 h at 70°C. The copolymer precursor for preparing the hybrid films was obtained. Then the TEOS homogeneous hydrolysate, prepared using deionized water, hydrochloric acid and THF, were added into the copolymer precursor solution. Meanwhile the sol-gel process was carried

Table 1. Monomer compositions for preparing\hybrid thin films

Sample	St [g]	MAn [g]	APTES [g]	TEOS [wt%]
Z1	28.61	26.96	40.53	5
Z2	27.11	25.54	38.40	10
Z3	25.39	24.31	36.26	15
Z4	24.09	22.70	34.13	20
Z5	22.59	21.28	32.00	25

All of polymerization mixtures had the following fixed composition: [APTES]/[St] + [MAn] + [APTES] = 25 mol%;
[AIBN]/[St] + [MAn] + [APTES] = 3.25 mol%

out. The synthetic route is shown in Figure 1. The homogeneous transparent sol can be obtained and then transferred to a conical flask. Solvents have been evaporated off the resulting gel slowly for 5 days and then was dried at 110°C under vacuum for 5 h to remove residual solvent and by-products (water and alcohol etc.). The thermally stable sol-gel hybrid material was obtained.

2.3. Measurement

FT-IR spectra of the prepared thin films were obtained on KBr pellets using Nicolet AVATAR 360 spectrometer. ^{29}Si NMR was performed using a Bruker DPX-400WB, Germany. HITACHI H-600 Transmission Electron Microscope (TEM) measured the particle sizes. Transmission electron microscopy (TEM) micrographs were obtained using a Hitachi H-600 operated at 80 kV with a 35 micron objective. Thermogravimetric analysis (TGA) and differential scanning calorimetry (DSC) were performed on NETZSCH STA 449C. The programmed heating range was from room temperature to 800°C, at a heating rate of 10°C/min under nitrogen atmosphere. The measurement was taken using 6–10 mg samples. TGA and DSC curves were recorded. The determination of sol fraction was to put the obtained hybrid materials in the sorbite extraction set and use acetone circulation reflux for 36 h. Then dried to constant weight in the vacuum drying oven. Sol fraction is calculated by Equation (1):

$$A = \frac{m_1 - m_2}{m_1} \cdot 100\% \qquad (1)$$

where A is the sol fraction, m_1 and m_2 are the mass before and after extraction, respectively.

3. Results and discussion

3.1. Fourier transforms infrared spectra

The results of FT-IR spectra (4000–400 cm^{-1}) of hybrid materials Z1–Z5 are shown in Figure 2. It could be easily found that 1788 and 1850 cm^{-1} was attributed to stretching peaks of carbonyl in carboxylic (–COOH) groups. Transmissions at 1732 and 1700 cm^{-1} belonged to stretching peaks of carbonyl in amid (–CONH) groups. Therefore it could be confirmed that amino-group of coupling agent APTES broke maleic anhydride of copolymer to form carboxylic acid and amide. However the TEOS and triethoxy-silicon group of APTES formed inorganic network by hydrolysis and condensation, which could be demonstrated by the absorption, peaks of Si–O–Si asymmetric stretching (1100 to 1050 cm^{-1}) and symmetric stretching (728 cm^{-1}).

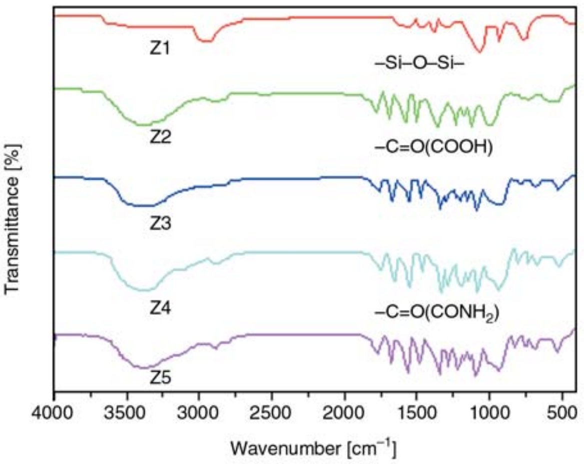

Figure 2. FT-IR spectra of hybrid materials

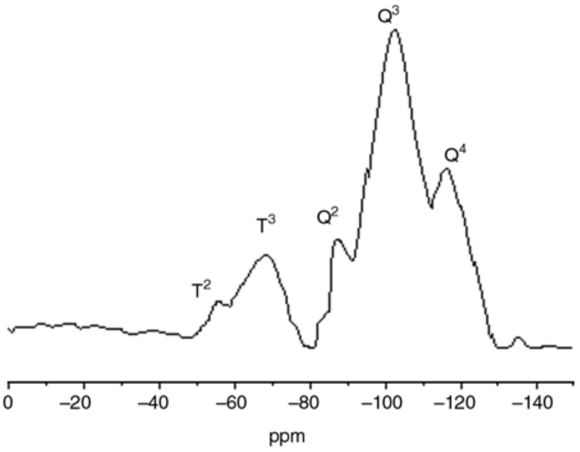

Figure 3. Solid-state ^{29}Si NMR spectrum of hybrid (Z3)

Figure 3 displays the solid-state ^{29}Si NMR spectra of the hybrid nanocomposite (Z3). The condensed siloxane species originating from TEOS, the silicon atoms through mono-, di-, tri-, and tetra-substituted siloxane bonds were designated as Q^1, Q^2, Q^3, and Q^4, respectively. The various Q^S were defined in Figure 4.

The 3-aminopropyltriethoxysilane, APTES, similarly with mono-, di-, tri-, tetra-substituted siloxane bonds were designated as T^1, T^2, T^3, respectively. The various T^S are defined in Figure 5.

The chemical shifts from the ^{29}Si NMR spectra of Q^2, Q^3, and Q^4 were –87, –102, –116 ppm, respectively, and were similar to those reported in the lit-

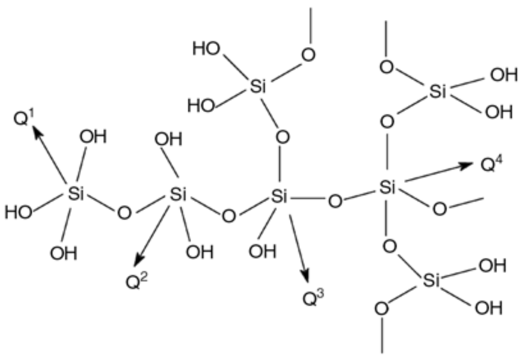

Figure 4. Abbreviations used for Si atoms attached to four oxygen atoms in various structural positions

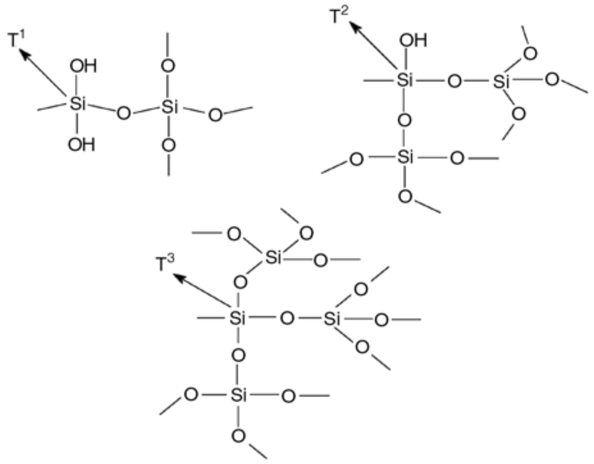

Figure 5. Abbreviations used for Si atoms attached to three oxygen atoms in various structural positions

erature [17]. The chemical shifts of T^2 and T^3 were –54 and –68 ppm, respectively, and also in good agreement with the literature values [18]. Results revealed that Q^3, Q^4 and T^3 were the major microstructures forming a network structure.

3.2. Determination of sol fraction

As is well known, good solvent will extract the part, which doesn't cross link with chemical bond. After the synthetic hybrid materials were extracted with acetone, the extraction sol is the copolymer, which doesn't combine to inorganic network with the covalent bond. The results of extraction experiments were 5.8% (Z1), 5.5% (Z2), 5.1% (Z3) and 4.9% (Z4) and 4.7% (Z5) respectively. This shows combination with chemical bond between organic and inorganic parts. Coupling agent APTES could integrate between the organic unit of the copolymer and inorganic network with covalent bond and restrain the extracted hybrid materials.

3.3. Microstructure analysis

Figure 6 shows the TEM pictures of Z2 and Z5 respectively. The silica particle size was about 50–70 nm.

3.4. Thermal analysis

The results of differential scanning calorimetry (DSC) and thermal gravimetric analysis (TGA) are shown by Figures 7, 8 and Table 2. The glass transition temperatures (T_g) and the thermal degradation temperatures (T_d) of the hybrids increased with the increase of APTES content. This is due to the fact that the plasticizing trimethoxysilyl groups have transformed to silica network during the sol-gel process. The large-scale cooperative movement

Table2. Thermal properties of hybrid materials

Hybrid material	T_g [°C][1]	T_d [°C][2]
Z1	122	292
Z2	134	298
Z3	148	303
Z4	152	309
Z5	160	313

[1] The glass transition temperature (T_g) was obtained from DSC curves

[2] The thermal degradation temperatures (T_d) were defined as weight loss of TGA thermogram at 5 wt%

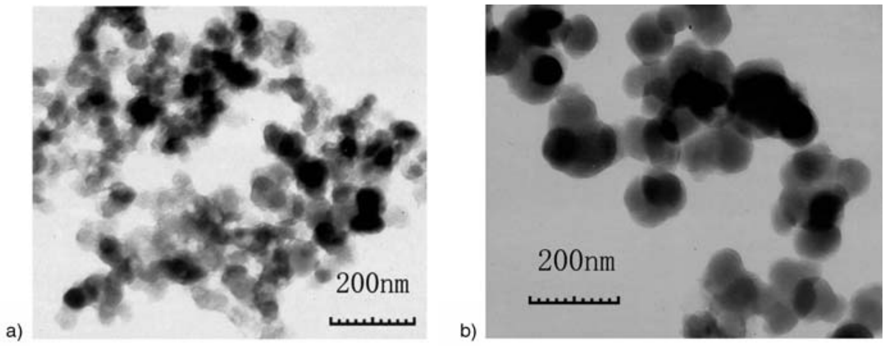

Figure 6. TEM pictures of poly (St-MAn-APTES)/SiO_2 for Z2 (a) and Z5 (b)

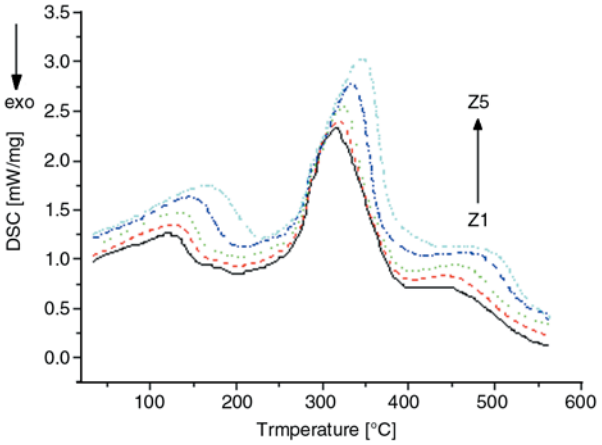

Figure 7. DSC curves of hybrid materials

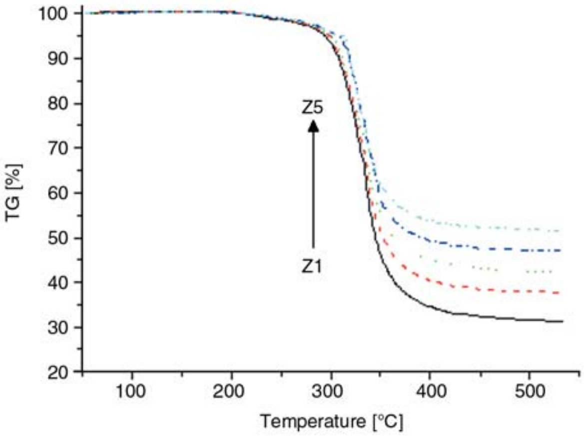

Figure 8. TGA curves of hybrid materials

of the polymer chain segments (i. e., glass transition) was highly restricted by the cross linking points that are generated from the formation of covalent bonds between the polymer chains and the silica network as well as by steric hindrance of the rigid silica (hydrolysis and condensation of TEOS) framework.

4. Conclusions

Different SiO_2 content hybrids were synthesized by the sol-gel process. FT-IR and ^{29}Si NMR were used to characterize the structure of the hybrids. The results show that Q^3, Q^4 and T^3 are the major microstructures forming the network structure. The SiO_2 structures in TEOS based hybrid systems were completely condensed. So these hybrid materials have network structure and inorganic phases have a small size. The hybrids were nanocomposites. Covalent bonding between the organic and inorganic components enhanced miscibility between the silica and the copolymer, which was further confirmed by TEM and the determination of sol content. Because the amino-group of coupling agent APTES breaks maleic anhydride of copolymer to form carboxylic acid and amide, the hybrids have new nanosystems with extremely good heat resistance, resulting from

Acknowledgements

This work was financially supported by the Jiangsu Planned Projects for Postdoctoral Research Funds (0602037B), the Natural Science of Jiangsu Education (05KJB150016) and the fund of Jiangsu University (06JDG015 and 06JDG076).

References

[1] Brennan A. B., Wilkes G. L.: Structure-property behavior of sol-gel derived hybrid materials: effect of a polymeric acid catalyst. Polymer, **32**, 733–739 (1991).

[2] Chiang C-L., Ma C-C. M.: Synthesis, characterization and thermal properties of novel epoxy containing silicon and phosphorus nanocomposites by sol-gel method. European Polymer Journal, **38**, 2219–2224 (2002).

[3] Hsiue G-H., Kuo W-J., Huang Y-P., Jeng R-J.: Microstructural and morphological characteristics of PS-SiO_2 nanocomposites. Polymer, **41**, 2813–2825 (2000).

[4] Hsu Y. G., Lin K. H., Chiang I. L.: Organic-inorganic hybrid materials based on the incorporation of nanoparticles of polysilicic acid with organic polymers. 1. Properties of the hybrids prepared through the combination of hydroxyl-containing linear polyester and polysilicic acid. Materials Science Engineering: B, **87**, 31–39 (2001).

[5] Ershad-Langroudi A., Mai C., Vigier G., Vassoille R.: Hydrophobic hybrid inorganic-organic thin film prepared by sol-gel process for glass protection and strengthening applications. Journal of Applied Polymer Science, **65**, 2387–2393 (1997).

[6] Philipp G., Schmidt H.: New materials for contact lenses prepared from Si- and Ti-alkoxides by the sol-gel process. Journal of Non-Crystalline Solids, **63**, 283–292 (1984).

[7] Chen W-C., Lee S-J., Lee L-H., Lin J-L.: Synthesis and characterization of trialkoxysilane-capped poly (methyl methacrylate)-titania hybrid optical thin films. Journal of Materials Chemistry, **9**, 2999–3003 (1999).

[8] Kagan C. R., Mitzi D. B., Dimitrakopoulos C. D.: Organic-inorganic hybrid materials as semi conducting channels in thin-film field-effect transistors. Science, **286**, 945–947 (1999).

[9] Huynh W. U., Dittmer J. J., Alivisatos A. P.: Hybrid nanorod-polymer solar cells. Science, **295**, 2425–2427 (2002).

[10] Huang W. Y., Ho S. W., Kwei T. K., Okamoto Y.: Photoluminescence behavior of poly (quinoline) s in silica glasses via the sol-gel process. Applied Physics Letter, **80**, 1162–1164 (2002).

[11] Yoshida M., Prasad P. N.: Sol-gel-processed SiO_2/TiO_2/poly (vinyl pyrrolidone) composite materials for optical waveguides. Chemistry of Materials, **8**, 235–241 (1996).

[12] Biteau J., Chaput F., Lahlil K., Boilot J. P., Tsivgoulis G. M., Lehn J-M., Darracq B., Marois C., Lévy Y.: Large and stable refractive index change in photochromic hybrid materials. Chemistry of Materials, **10**, 1945–1950 (1998).

[13] Miller R. D., Michl J.: Polysilane high polymers. Chemical Reviews, **89**, 1359–1410 (1989).

[14] Wei Y., Yang D. C., Tang L. G.: Synthesis, characterization, and properties of new polystyrene-SiO_2 hybrid sol-gel materials. Journal of Materials Research, **8**, 1143– 1152 (1993).

[15] Coltrain B. K., Landry C. J. T., O'Reilly J. M., Chamberlain A. M., Rakes G. A., Sedita J. S., Kelts L. W., Landry M. R., Long V. K.: Role of trialkoxysilane functionalization in the preparation of organic-inorganic composites. Chemistry of Materials, **5**, 1445–1455 (1993).

[16] Qiu F-X., Zhou Y-M., Liu J-Z.: The synthesis and characteristic study of 6FDA-6FHP-NLO polyimide/SiO_2 nanohybrid materials. European Polymer Journal, **40**, 713–720 (2004).

[17] Qiu F. X., Jiang Y., Zhou Y. M., Liu J. Z.: Synthesis, characterization and thermal properties of novel PMDA-PAPD/silica hybrid network polymers. Silicon Chemistry, **3**, 65–73 (2006).

[18] Joseph R., Zhang Z., Ford W. T.: Structure and dynamics of a colloidal silica-poly (methacrylate) composite by ^{13}C and ^{29}Si MAS NMR spectroscopy. Macromolecules, **29**, 1305–1312 (1996).

eXPRESS Polymer Letters Vol.1, No.10 (2007) 704–709
Available online at www.expresspolymlett.com
DOI: 10.3144/expresspolymlett.2007.96

Dynamic dielectric properties and the γ transition of bromine doped polyacrylonitrile

N. Cohen[1], *A. Greenbaum*[2], *Y. Feldman*[2], *G. Marom*[1]*

[1]Casali Institute of Applied Chemistry, The Institute of Chemistry, The Hebrew University of Jerusalem, 91904 Jerusalem, Israel
[2]Department of Applied Physics, School of Computer Science and Engineering, The Hebrew University of Jerusalem, 91904 Jerusalem, Israel

Received 16 July 2007; accepted in revised form 29 August 2007

Abstract. Based on monitoring the γ process (the lowest temperature-relaxation) in polyacrylonitrile (PAN) by dynamic dielectric spectroscopy, new evidence for the formation of a charge transfer complex between bromine dopants and nitrile groups is presented. The experimental work is carried out on PAN and nitrile polymerized PAN with and without bromine doping and the effects of these factors on the γ process are measured. Nitrile polymerization results in diminishing of the γ process and in a 15% increase in its activation energy, whereas bromine doping produces splitting of the original γ process in PAN – coupled with a significant activation energy increase – and its complete disappearance in nitrile polymerized PAN. Both the splitting of the γ process and the higher activation energy reflect bromine-nitrile adduct formation.

Keywords: *smart polymers, polyacrylonitrile (PAN), charge transfer bromine complexes, dynamic dielectric behavior, γ transition*

1. Introduction

Polyacrylonitrile is an attractive polymer because of its ability to form long conjugated imine chains (conjugated PAN) via polymerization of its pending nitrile groups, by heating above 180°C. Also formed by the nitrile polymerization is a condensed cyclic structure, referred to by the term ‘ladder polymer’, which increases the thermal stability of the system [1]. The conjugated π system renders PAN an outstanding candidate for various applications that involve semi-conductive properties. The ability of PAN to form a conjugated imine system of potential electrical conductivity had intrigued our research for quite some time prior to the present study. We demonstrated earlier that, considering the analogy to polyacetylene and other conductive polymers, it was reasonable to expect that doping of PAN with acceptor-type compounds would be significantly beneficial for its electrical properties [2]. Conceivably, as in polyacetylene, doping (oxidation) with iodine or bromine causes electrons of the conjugated systems to be ejected from the polymer, leaving positive charge ‘holes’ that can move along the chain.

Unlike polyacetylene, however, both PAN and conjugated imine systems exhibit a more complex state due to the presence of nitrile/imine nitrogen that can donate its lone electron pair to the acceptor. Thus, acceptor type compounds and ions such as halogens, Ag^+, $FeCl_3$, and $CuCl_2$ can form coordination bonds with the cyano/imine nitrogen of PAN, wherein a lone electron pair from occupied $2p$ orbitals is donated to the empty s orbitals of the acceptor to form a δ-bond. The coordination of cyano nitrogen and Ag^+ was shown to be highly

---

*Corresponding author, e-mail: gadm@vms.huji.ac.il

stable and to endure the reduction of silver ions in a process to form metallic silver nanoparticles free of aggregation [3]. The participation of nitrile/imine groups in coordination bonds with carbon nanotubes was also studied recently by our group, showing that the π interactions were stronger than the original dipole–dipole interactions of the nitriles [4]. It was claimed that in view of the strong metallic character of carbon nanotubes, the role of the nitrile groups is reversed and they act as an electron acceptor, unlike their role as electron donor in the formation of stable electron donor-acceptor (EDA) complexes with Lewis acids [5].

This present work studies the behavior of doped PAN and the ability of halogens, such as Br_2, to create charge transfer complexes/adducts with the conjugated system and the nitrile groups. In this communication we present corroborating evidence for a coordination bond that forms between the nitrile/imine nitrogen of PAN and Br_2. This evidence resulted from a study of molecular processes and electronic properties of PAN doped with bromine, which was based on frequency and temperature-dependent complex dielectric permitivity [6]. Accordingly, the new evidence is based on mobility changes due to doping by bromine reflected in a second order phase transition (the γ transition) of both PAN and conjugated PAN.

Generally, amorphous or semicrystalline pending side-group polymers exhibit two or three second order phase transitions, respectively. In the semicrystalline polymers, such as polypropylene and PAN, the three transitions are designated in descending order from the melting temperature as α, β, and γ [7]. A recent paper on dynamic mechanical relaxation in PAN with different stereoregularities presents a summary of the relaxation temperatures for PAN, as reported previously in several references, and concludes by pointing out the characteristics of each transition and assigning it to corresponding molecular processes [8]. In agreement with the conventional claim that the lowest temperature transition (e.g., the γ transition) in side-group polymers (PP, PVC, PS, etc.) is associated with local motion of groups such as $–CH_3$ and –Cl, the paper assigns the γ transition in PAN to local mode motions of syndiotactic and short isotactic sequences. It is also pointed out that the lower tail of this relaxation extends down to –150°C.

Accordingly, the molecular processes in bromine doped PAN were characterized by dielectric measurements to test the hypothesis that if a coordination bond should form between the nitrile/imine nitrogen of PAN and Br_2, the γ relaxation process would be affected, perhaps by shifting to a higher temperature and exhibiting a higher activation energy.

2. Experimental procedure

2.1. Materials and sample preparation

Polyacrylonitrile powder was obtained from Scientific Polymer Products, Inc.; the polymer was characterized by a melting point of 317°C, a glass transition temperature of 125°C, and $M_w \sim$ 150 000 g/mol.

Films were prepared in a solution casting method, by mixing 2 g of PAN powder and 25 ml of dimethyl formamide solvent at 60°C for a few minutes, producing a transparent mixture. The mixture was dried in a hood for a few days and then compressed (Carver 2518 press) at 100°C (pressure 2 MPa) and then returned to the hood for final drying.

2.2. Preparation of doped PAN

The samples were doped with bromine, which was placed in a desiccator with the samples for various durations up to 10 h. The samples were weighed before and after doping until the weight was stabilized and the weight change was calculated.

2.3. Preparation of heat-treated PAN

The samples were heat-treated in air either at 220°C for 30 min or at 250°C for 1.5 h.

2.4. Dielectric spectroscopy measurements

Dielectric measurements were performed by using a broad band Alpha high resolution dielectric analyzer (Novocontrol) with automatic temperature control in a range of –100 to 160°C and at a frequency range of $0.1–10^6$ Hz. A 3°C step was applied throughout the measurement routine. Each sample, with a thickness in the range of 0.01–0.3 mm, was inserted between parallel plate electrodes of the measurement cell at room temperature, and measurement was preceded by cooling down to –100°C. The measurement produced the complex dielectric permittivity ε* from which the real and imaginary components, namely the permittivity ε', and the dielectric loss ε" were resolved.

3. Results and discussion

To validate the research hypothesis, four systems were tested, namely, pristine PAN, heat-treated PAN (at 250°C), Br_2 doped PAN, and Br_2 doped heat-treated PAN. All four systems were examined by dielectric spectroscopy and the 3-D plots of the dielectric loss ε" as a function of frequency and temperature for qualitative impression are presented in Figure 1. As an example, the dielectric spectroscopy response of the pristine PAN sample is presented over the whole tested temperature range in Figure 1a. A total of three relaxation processes can be observed, designated in descending order (from high to low temperature) as α, β, and γ according to the common convention [7]. The α relaxation is assigned to the interaction between the amorphous and crystalline phases (but in fact, might be masked by the dynamic percolation process [9] – not discussed here). The β process is situated in the temperature range 50–100°C and in almost the whole frequency range; it is assigned to the glass-rubber transition of the amorphous phase. The γ process is situated in the high frequency range and in the temperature range –100 to –30°C and is assigned to the motion of nitrile-side-groups. Obviously, in this study we are interested in the γ process and how it reflects formation of a nitrile-Br_2 complex. Accordingly, Figures 1b–1d present the dielectric spectroscopy results of the other three samples over a lower temperature range that is limited to the γ process regime. It is seen (in Figure 1b) that the thermal treatment that produces the conju-

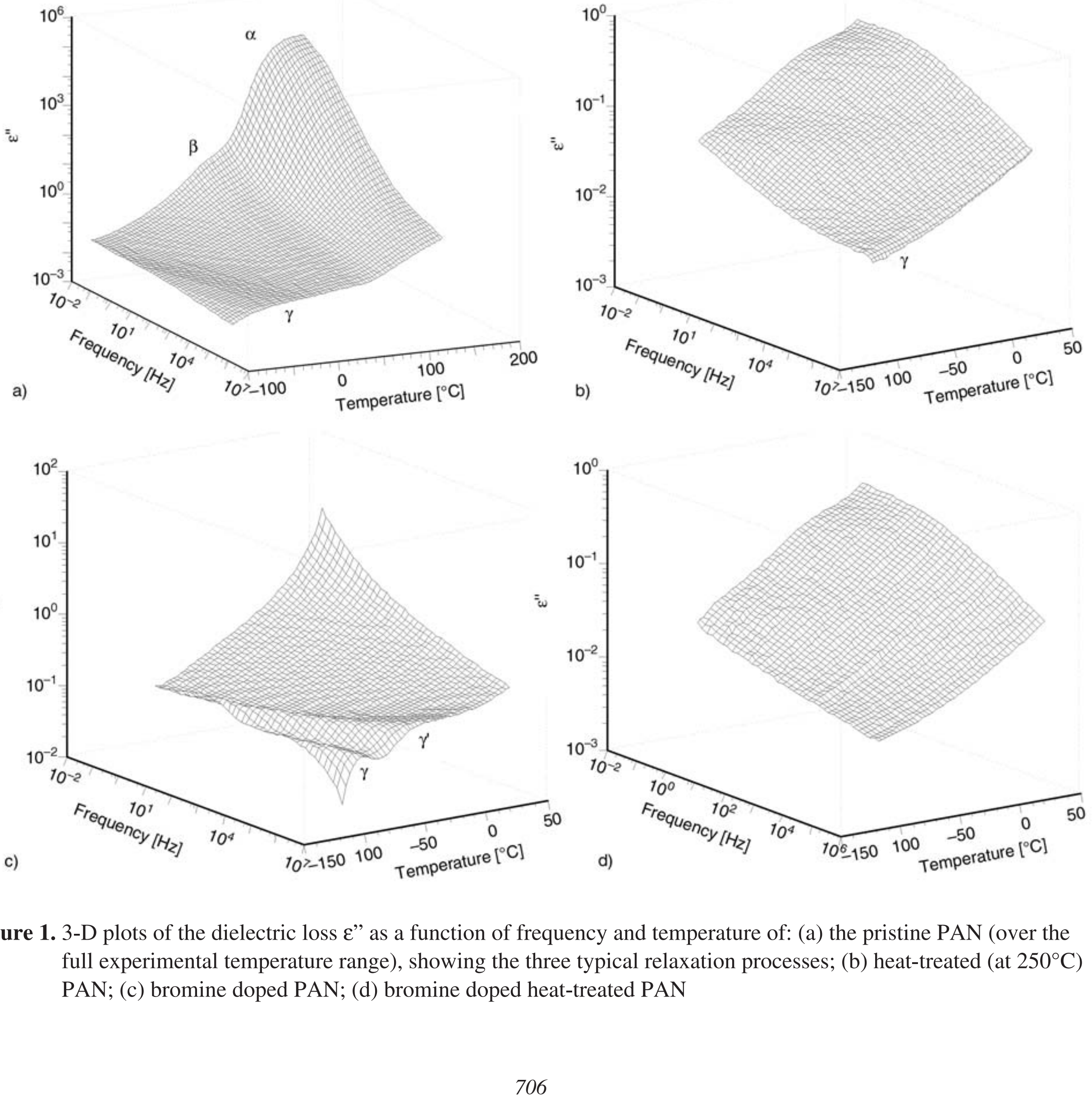

Figure 1. 3-D plots of the dielectric loss ε" as a function of frequency and temperature of: (a) the pristine PAN (over the full experimental temperature range), showing the three typical relaxation processes; (b) heat-treated (at 250°C) PAN; (c) bromine doped PAN; (d) bromine doped heat-treated PAN

gated imine system as part of a ladder structure results in restriction of movement of the remaining nitrile groups and consequently in diminishing of the γ process. (Additional evidence for the decrease in nitrile group concentration and their partial polymerization to form a conjugated imine system was received by FTIR analysis [6].)

Doping of PAN with Br was monitored by recording the weight increase and by X-ray photoelectron spectroscopy (XPS) analysis of the proportion of ionic/covalent Br as a function of exposure time, as done in our previous study of Br treated graphite nanoplatelets [10]. However, because at this stage we were unable to identify consistent trends, only the results of 8 and 10% Br weight increase, respectively, are reported. It is seen that doping of PAN with Br results in splitting of the γ process peak into two peaks denoted by γ and γ' (Figure 1c). As an example, the split γ peak is shown again in Figure 2, where 2-D plots of the dielectric loss as a function of temperature are shown for the 10^4 Hz frequency. Apparently, a certain proportion of the nitrile groups have formed complexes with the bromine, producing bulkier and more hindered side group adducts. Their movement requires higher free volume, thus the γ' process, thought to substitute the original γ process, is shifted to a higher temperature. The new γ process in the bromine doped PAN is situated at a lower temperature relative to the original one. This new γ process is assigned to –Br side groups formed by bromination of the polymer backbone (see Figure 3 – the proportion of C–Br covalent bonds as a function of bromination time was established by XPS (not shown here) [6]). Finally, the combined effect of heat treatment at 250°C and bromine doping is presented in Figure 1d; in this case the γ process disappears altogether, indicating that even the –Br side groups, if formed by bromination, are locked in place by the ladder structure.

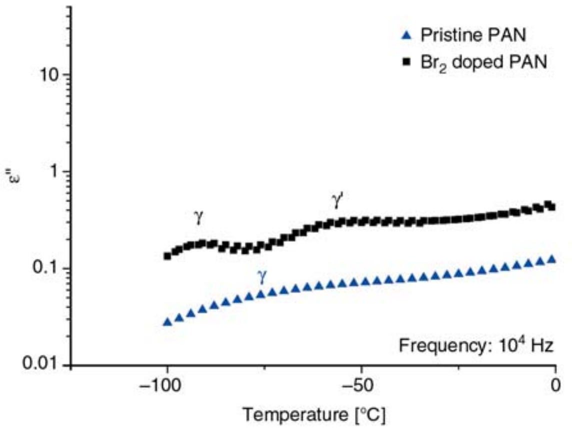

Figure 2. 2-D plots of the dielectric loss ε'' as a function of temperature for a constant 10^4 Hz frequency, showing the γ transition and the γ and γ' transitions for the pristine and bromine doped PAN, respectively

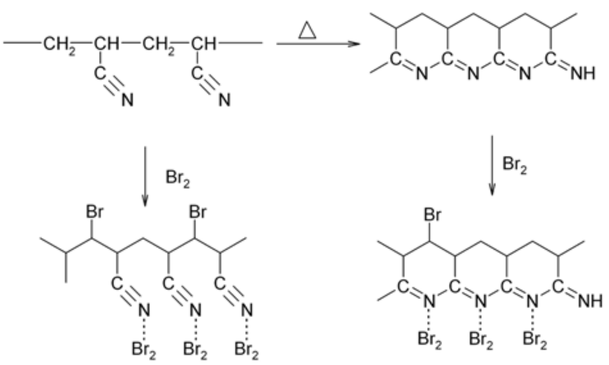

Figure 3. Chemical reactions that pertain to the material systems of Figure 1, showing polymerization of a sequence of pending nitrile groups in a PAN chain segment to form a conjugated ladder structure and doping with bromine to produce electron transfer adducts

The chemical reactions that pertain to the results in Figure 1 and to the corresponding arguments can be presented schematically as follows (Figure 3). A sequence of pending nitrile groups in a PAN chain segment can polymerize to form a conjugated ladder structure of restricted mobility. Doping with bromine produces bulkier electron transfer adducts with either the nitrile/imine groups. Bromination of the main backbone can produce C–Br covalent bonds in the two systems. (It is apparent that the weight increase by doping is accounted for by either or both Br forms.)

An additional expression of the effects of bromine doping and nitrile polymerization is the activation energy of the γ process. It is anticipated that both effects produce increased activation energy as both generate excessive restrictions on chain segment movement. Figures 4a and 5a present plots of the dielectric loss as a function of frequency for a number of selected example temperatures for PAN and heat-treated PAN, respectively. In both, the peak of the γ process is shifted to higher frequencies as the temperature is increased. This shift sets the basis for an Arrhenius type functionality, wherein the logarithm of the relaxation time is a linear function of the reciprocal peak temperature. Accordingly, Figures 4b and 5b present the Arrhenius plots of the

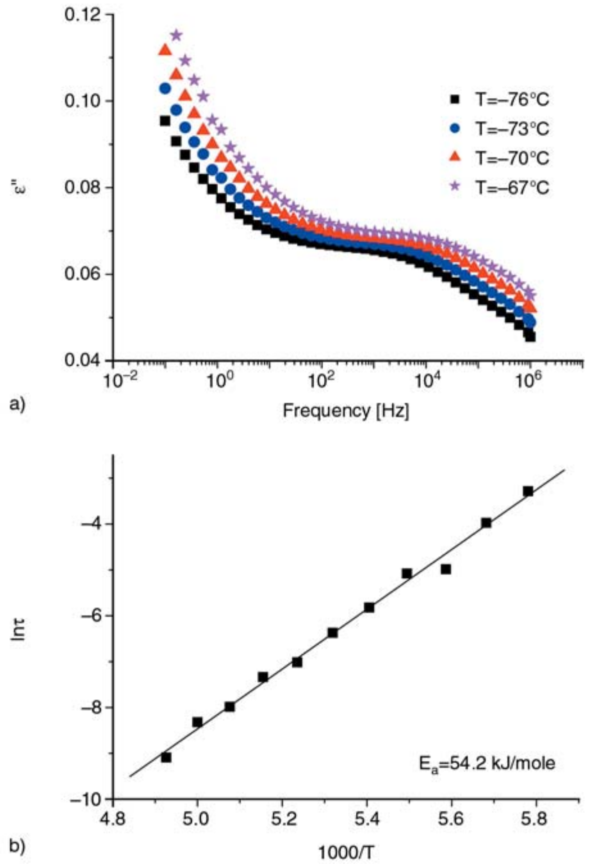

Figure 4. Plots for PAN of: (a) the dielectric loss as a function of frequency in a number of selected temperatures; (b) the logarithm of relaxation time as a function of the reciprocal peak temperature

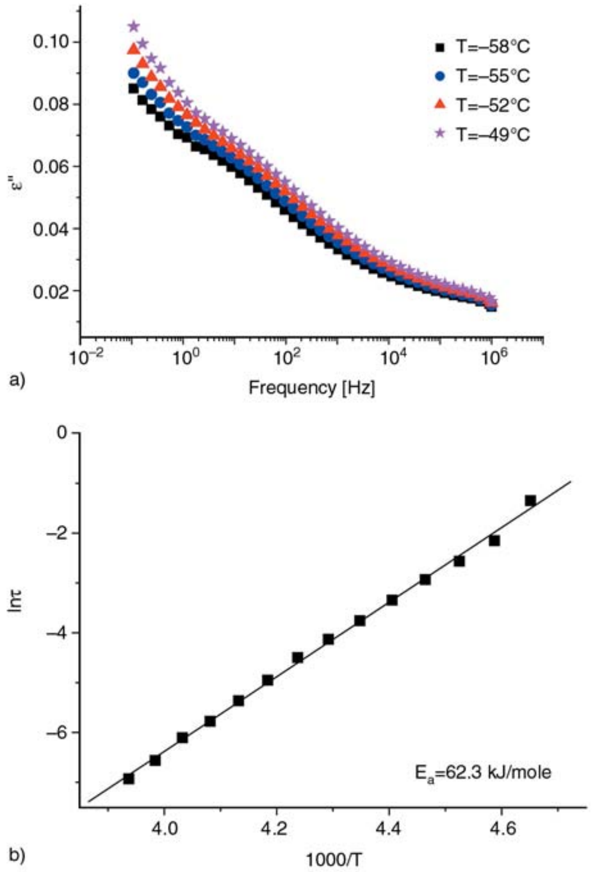

Figure 5. Plots for heat-treated PAN of: (a) the dielectric loss as a function of frequency in a number of selected temperatures; (b) the logarithm of relaxation time as a function of the reciprocal peak temperature

same samples. The data comply with the model, exhibiting linear behavior of high statistically significant correlation coefficients and yielding (from the slopes of the lines) activation energies of 54.2 and 62.3 kJ/mole in the temperature range from –100 to –30°C, for PAN and heat-treated PAN, respectively. Obviously, the activation energy of the γ process in the partially polymerized nitrile system is 15% higher, indicative of the restricted movement.

Plots of the dielectric loss as a function of frequency of the bromine-doped PAN for a few selected temperatures, chosen from the temperature range where both γ and γ' appear, are shown in Figure 6. The Arrhenius based activation energies of these processes were calculated (over the full temperature range) to be 64.4 and 59.5 kJ/mole, respectively. It is seen that the formation of bromine-nitrile adducts, expressed by splitting of the original γ process, results in higher activation energies in the two processes and not only in the γ' process that is assigned to the adduct.

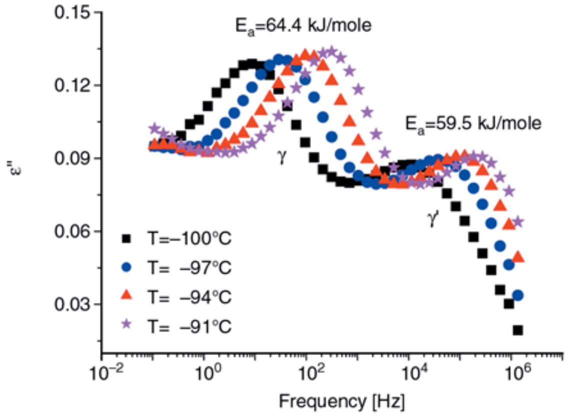

Figure 6. Plots of the dielectric loss ε'' as a function of frequency in a number of selected temperatures from the temperature range where both γ and γ' appear, indicating the activation energies of the two processes

4. Conclusions

The γ process in PAN appears in the lower temperature range and the tail of this relaxation extends down to –100°C. It denotes a relaxation that is associated with movement of pending nitrile groups at activation energy of 54.2 kJ/mole. The restriction of movement associated with the thermal treatment that produces the conjugated imine system as part of a ladder structure results in diminishing of the γ process and in raising its activation energy by 15%. Doping with bromine produces two consequences that relate to the γ process, namely, the process is spilt into two and the activation energies increase by 10–15%. The appearance of the γ' process is taken as significant evidence for the formation of nitrile-bromine charge transfer complexes.

References

[1] Cohen D., Marom G., Zilkha A.: Physical properties of polyacrylonitrile fibres treated with organotin compounds. European Polymer Journal, **12**, 795–800 (1976).

[2] Brokman A., Weger M., Marom G.: Electrical conductivity of halogen doped stabilized polyacrylonitrile. Polymer, **21**, 1114–1115 (1980).

[3] Wang Y., Yang Q., Shan G., Wang C., Du J., Wang S., Li Y., Chen X., Jing X., Wei Y.: Preparation of silver nanoparticles dispersed in polyacrylonitrile nanofiber film spun by electrospinning. Materials Letters, **59**, 3046–3049 (2005).

[4] Vaisman L., Larin B., Davidi I., Wachtel E., Marom G., Wagner H. D.: Processing and characterization of extruded drawn MWNT-PAN composite filaments. Composites, Part A, **38**, 1354–1362 (2007).

[5] Vaisman L.: The reinforcement effect in carbon nanotube based polymer composites. Ph.D. Thesis, The Hebrew University of Jerusalem (2007).

[6] Cohen N.: Molecular processes and electronic properties of PAN doped with bromine. M.Sc. Thesis, The Hebrew University of Jerusalem (2007).

[7] Ward I. M., Hadely D. W.: An introduction to the mechanical properties of solid polymers. John Wiley and Sons, Chichister (1993).

[8] Sawai D., Kanamoto T., Yamazaki H., Hisatani K.: Dynamic mechanical relaxations in PAN with different stereoregularities. Macromolecules, **37**, 2839–2846 (2004).

[9] Feldman Y., Kozlovich N., Nir I., Garti N.: Dielectric relaxation in sodium bis(2-ethylhexyl)sulfosuccinate-water-decane microemulsions near the percolation temperature threshold. Physical Review E, **51**, 478–491 (1995).

[10] Li J., Vaisman L., Marom G., Kim J. K.: Br treated graphite nanoplatelets for improved electrical conductivity of polymer composites. Carbon, **45**, 744–750 (2007).